Sensitivity to quantum decoherence in neutrino oscillations with KM3NeT

Master's Thesis in Physics

Presented by

Nadja Lessing

03.03.2022

Erlangen Center for Astroparticle Physics

Physikalisches Institut

Friedrich-Alexander-Universität Erlangen-Nürnberg

Betreuer: PD Dr. Thomas Eberl

Contents

1 Introduction

Although neutrinos were postulated as early as in 1930, it was not until 1956 that the first detection of a neutrino was confirmed. Since then, neutrino physics has become a major field in particle physics. Neutrinos are leptonic particles with no electric charge and a small rest mass. In the Standard Model of particle physics, there are three different neutrino flavor states, ν_e, ν_μ, and ν_τ, each corresponding to one of the charged leptons, e, μ and τ. Neutrinos only interact via the weak interaction and have very small cross sections. Therefore, to study their properties, huge detectors are necessary in order to collect sufficient event statistics.

Currently, IceCube is the biggest neutrino detector with an instrumented volume of $1\,\mathrm{km}^3$ of ice at the South Pole [1]. As many other neutrino detectors, IceCube makes use of the Cherenkov effect: the neutrinos interact inside the detector and produce a charged lepton that travels faster than the speed of light in the medium. Therefore, the passage of the lepton causes a flash of light that can be detected with PMTs.

In the last decades, a lot of progress in neutrino physics was made using Cherenkov detectors. A major milestone was the detection of neutrino oscillations in 1998 by Super-Kamiokande [2] and in 2002 by the Sudbury Neutrino Observatory [3] (shared Nobel Prize 2015). Neutrino oscillations describe the phenomenon that a neutrino of a certain flavor oscillates into another flavor as it propagates. The precise measurement of the oscillation parameters is a crucial goal of many neutrino experiments. Further open questions in neutrino physics are for example the neutrino mass ordering and whether neutrinos violate CP-symmetry. Also, there could be still unknown effects that modify neutrino oscillations.

One of these effects, called *quantum decoherence*, is proposed in different theories of quantum gravity. Decoherence emerges when the neutrino system is treated as an open quantum system that couples to the environment [4]. Since decoherence modifies the oscillation patterns, it could potentially be verified by detectors like KM3NeT/ARCA and KM3NeT/ORCA (*Astroparticle & Oscillations Research with Cosmics in the Abyss*), which are two Cherenkov detectors that are currently being built in the Mediterranean sea. While ARCA is primarily designed to detect high energy cosmic neutrinos, ORCA is aimed at the precise measurement of atmospheric neutrino oscillations [5]. In this work, the sensitivity of both detectors to decoherence effects in neutrino oscillations is studied.

This work uses a phenomenological model to describe decoherence effects. The model will be introduced in the first chapter after discussing standard neutrino oscillations. The second chapter covers the details of the sensitivity calculations and the software used for the analysis. In the third chapter, calculated oscillation probabilities with decoherence effects are presented. Finally, the fourth chapter contains the detector sensitivities as well as a discussion of systematic parameters.

2 Scientific background

In this chapter, an overview of the theory of standard neutrino oscillations in vacuum and matter is given. Taking matter effects into account is highly relevant for the KM3NeT detectors since, in order to suppress the atmospheric muon background, only neutrinos that have passed through the Earth before they reach the detector are identified as neutrino events. In Sec. 2.2 decoherence effects are included in the oscillation model. Also, as the Earth's density is not constant, the case of non-uniform matter is discussed. Furthermore, the properties of atmospheric neutrinos as well as the detection technique of the KM3NeT detectors ARCA and ORCA is explained.

2.1 Standard neutrino oscillations

The theory of neutrino oscillations describes the transition of one flavor to another one during the propagation of the neutrino. This mechanism was first proposed in 1957 to explain the discrepancy between the flux of electron neutrinos arriving at the Earth, and the flux predicted from the Sun. the predicted flux was too high, since it did not account for flavor transitions into muon neutrinos.

Neutrino oscillations arise from the fact that the flavor eigenstates $|\nu_\alpha\rangle$ (with $\alpha = e, \mu, \tau$) are not identical to the mass eigenstates $|\nu_i\rangle$ (with $i = 1, 2, 3$). While neutrinos are produced and observed with a certain flavor, the propagation occurs in the mass basis. In standard neutrino oscillations the eigenstates are related by

$$|\nu_\alpha(t)\rangle = \sum_i U_{\alpha i} \, |\nu_i(t)\rangle \ , \tag{2.1}$$

where U is a unitary matrix, called the Pontecorvo-Maki-Nakagawa-Sakata (PMNS) matrix. Using this relation, we can calculate the probability $P(\nu_\alpha \to \nu_\beta)$ that a neutrino ν_α is detected as ν_β after propagation:

Starting from Schrödinger's equation

$$i\frac{d}{dt} \, |\nu_i(t)\rangle = H_{\text{vac}} \, |\nu_i(t)\rangle \ , \tag{2.2}$$

the time evolution of the mass states in vacuum is given by

$$|\nu_i(t)\rangle = e^{-iE_i t} \, |\nu_i\rangle \ , \tag{2.3}$$

where $E_i = {}^{m_i^2}/_{2E}$ are the diagonal elements of $H_{\text{vac}} = \text{diag}(E_1, E_2, E_3)$ in the vacuum mass basis, with the neutrino masses m_i and the average neutrino energy $E = \frac{1}{3}(E_1 + E_2 + E_3)$. Using Equation 2.1 and the relation $\langle \nu_i | \nu_j \rangle = \delta_{ij}$, the amplitude for a flavor transition can be written as

$$\langle \nu_\beta | \nu_\alpha(t) \rangle = \sum_i U^*_{\beta i} U_{\alpha i}\, e^{-iE_i t}\,. \tag{2.4}$$

The probability for a flavor transition is therefore given by

$$P(\nu_\alpha \to \nu_\beta) = |\, \langle \nu_\beta | \nu_\alpha(t) \rangle\, |^2 = \sum_{i,j} U_{\alpha i} U^*_{\beta i} U^*_{\alpha j} U_{\beta j}\, e^{-i\Delta E_{ij} t}\,, \tag{2.5}$$

where $\Delta E_{ij} = (E_i - E_j)$ is the energy difference of two mass states.

2.1.1 Neutrino mass hierarchy

From Equation 2.5 it becomes apparent that the squared mass difference

$$\Delta E_{ij} = \frac{m_i^2 - m_j^2}{2E} \tag{2.6}$$

of the neutrino states determines the frequency of the oscillations. This also means that only the squared mass differences, and no absolute neutrino masses can be determined in oscillation experiments.

The value of Δm^2_{21} was measured very precisely [6] using solar neutrinos and it is often referred to as Δm^2_{sol}. The sign of Δm^2_{sol} was determined taking advantage of matter effects, so it is known that $m_2^2 > m_1^2$. For the larger squared mass difference $|\Delta m^2_{31}| \approx |\Delta m^2_{32}|$, only the absolute value has been measured until now. This parameter is often referred to as Δm^2_{atm}, since it is measured most precisely by experiments that detect atmospheric neutrinos.

Depending on the sign of Δm^2_{atm}, two scenarios are possible for the mass hierarchy of the neutrino states. For normal hierarchy (NH), the state ν_3 has the largest mass whereas for inverted hierachy (IH), the state ν_3 has the smallest mass. The two scenarios can be seen in Figure 2.1. Since the neutrino mass hierarchy is not known at the time, both scenarios are taken into account in the sensitivity studies presented in this work.

2.1.2 Mixing angles and CP-violating phase

While the squared mass differences determine the frequency of the oscillations, the elements of the PMNS matrix determine the amplitude, as can also be seen from Equation 2.5. The PMNS matrix can be written more conveniently in terms of three mixing angles Θ_{12}, Θ_{13}, and Θ_{23} and a complex phase δ_{CP} as [7]

$$\begin{pmatrix} U_{e1} & U_{e2} & U_{e3} \\ U_{\mu 1} & U_{\mu 2} & U_{\mu 3} \\ U_{\tau 1} & U_{\tau 2} & U_{\tau 3} \end{pmatrix} = \begin{pmatrix} c_{12}c_{13} & s_{12}c_{13} & s_{13}e^{-i\delta_{\text{CP}}} \\ -s_{12}c_{23} - c_{12}s_{23}s_{13}e^{i\delta_{\text{CP}}} & c_{12}c_{23} - s_{12}s_{23}s_{13}e^{i\delta_{\text{CP}}} & s_{23}c_{13} \\ s_{12}s_{23} - c_{12}c_{23}s_{13e^{i\delta_{\text{CP}}}} & c_{12}s_{23} - s_{12}c_{23}s_{13}e^{i\delta_{\text{CP}}} & c_{23}c_{13} \end{pmatrix}, \tag{2.7}$$

where $s_{ij} = \sin(\Theta_{ij})$ and $c_{ij} = \cos(\Theta_{ij})$.

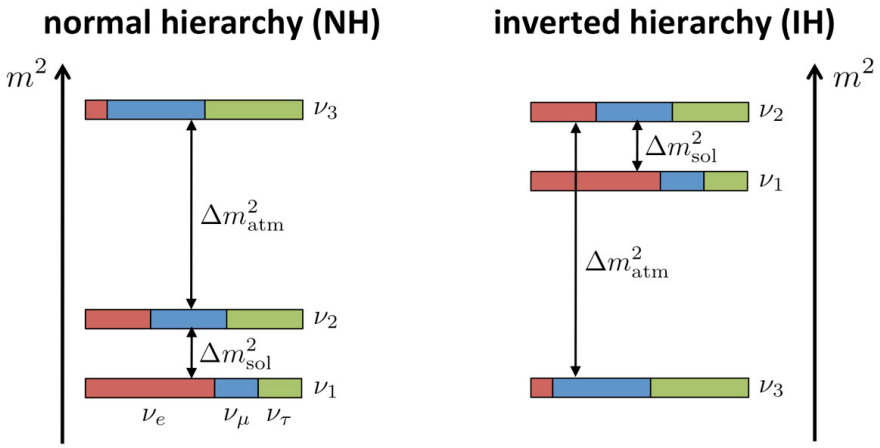

Figure 2.1: Two scenarios for the neutrino mass hierarchy depending on the sign of the larger squared mass difference Δm^2_{atm}. Additionally, the ratio of the flavor eigenstates is shown for each mass state where red corresponds to electron neutrinos, blue to muon neutrinos, and green to tau neutrinos.

Since the PMNS matrix is not necessarily real, CP violation could be possible, which means that in general $P(\nu_\alpha \to \nu_\beta) \neq P(\bar{\nu}_\alpha \to \bar{\nu}_\beta)$. This is described with the CP-violating phase δ_{CP}. At the time, this parameter is not known very precisely. While the mixing angle Θ_{13} was measured very accurately using reactor neutrinos [8], the uncertainties for Θ_{12} and Θ_{23} are still relatively large. Θ_{12} corresponds to the amplitude of the wavelength associated with the smaller squared mass difference Δm^2_{sol}. At the energy range of atmospheric neutrinos, this wavelength is longer than the diameter of the Earth. Since the longest baseline of atmospheric neutrinos is given by the Earth's diameter, ORCA is not sensitive to this parameter. ARCA is not sensitive to any oscillation parameter, since the oscillations vanish completely for the high energy neutrinos that ARCA can detect.

From the data taken with solar, atmospheric, reactor and accelerator neutrinos, the current global best fit values for the oscillation parameters (for NH) are [9]:

$$\Theta_{12} = (33.44^{+0.77}_{-0.74})^\circ\,,$$
$$\Theta_{23} = (49.2^{+1.0}_{-1.3})^\circ\,,$$
$$\Theta_{13} = (8.47^{+0.13}_{-0.12})^\circ\,,$$
$$\delta_{\text{CP}} = (194^{+52}_{-25})^\circ\,,$$
$$\Delta m^2_{\text{sol}} = (7.42^{+0.21}_{-0.20}) \cdot 10^{-5}\,\text{eV}^2\,,$$
$$\Delta m^2_{\text{atm}} = (2.515^{+0.028}_{-0.028}) \cdot 10^{-3}\,\text{eV}^2\,.$$

Together with the neutrino energy E and the distance that the neutrino travels, these parameters determine the oscillation probabilities.

2.1.3 Standard neutrino oscillations in matter

So far, no matter effects have been included in the oscillation model. In matter, the neutrinos can interact with the surrounding electrons via elastic forward scattering by exchanging a Z-boson (neutral current interaction) or a W-boson (charged current interaction). While the neutral current interaction is equally likely for all flavors and therefore does not change the oscillation probability, the charged current interaction is only possible for electron (anti-)neutrinos. Hence, the electron (anti-)neutrinos acquire an effective potential of the form

$$V = \begin{cases} +\sqrt{2}G_{\mathrm{f}}N_{\mathrm{e}}, & \text{for } \nu_e \\ -\sqrt{2}G_{\mathrm{f}}N_{\mathrm{e}}, & \text{for } \bar{\nu}_e \end{cases}, \tag{2.8}$$

where G_{f} is the Fermi coupling constant and N_{e} is the electron number density. The interaction Hamiltonian can be written as

$$H_{\mathrm{int}} = \pm\sqrt{2}G_{\mathrm{f}}N_{\mathrm{e}} \begin{pmatrix} 1 & 0 & 0 \\ 0 & 0 & 0 \\ 0 & 0 & 0 \end{pmatrix} \tag{2.9}$$

in the flavor basis. The full Hamiltonian in the mass basis is given by

$$H = H_{\mathrm{vac}} + U^{\dagger}H_{\mathrm{int}}U\,, \tag{2.10}$$

and is no longer diagonal in the vacuum mass basis. This causes the vacuum mass states to mix. However, it is possible to diagonalize H by a unitary matrix $\tilde{U}$, which leads to decoupled effective mass eigenstates in matter. From now on, the diagonalized Hamiltonian in the effective mass basis will be denoted as

$$\tilde{H} = \tilde{U}^{\dagger}H\tilde{U} = \mathrm{diag}(\tilde{E}_1, \tilde{E}_2, \tilde{E}_2)\,, \tag{2.11}$$

with $\tilde{E}_i = \tilde{m}_i^2/2E$ where $\tilde{m}_i$ are the effective neutrino masses in matter.

2.2 Neutrino oscillations with decoherence

When oscillations are modified due to loss of coherence this is generally referred to as decoherence. In this work, we will consider *non-standard* decoherence, induced by the coupling of the quantum system with the environment.

Non-standard decoherence differs from standard decoherence, which is caused by the separation of wave packets (see for example [10] and [11]). In a neutrino system with standard decoherence effects, the time evolution is still unitary and can be described within the Standard Model. Including non-standard decoherence effects, the time evolution of the quantum system alone, excluding the environment, is generally not unitary [12]. Non-unitary time evolution can be studied in the context of open quantum systems.

A description of the open system approach applied to neutrino oscillations for two flavors in vacuum can be found in [13]. An extension of the mathematical formalism to three families can be found in [14]. As pointed out in [15], the effects of decoherence strongly

depend on the neutrino mass ordering and on matter effects. Therefore we will describe decoherence in the full three-flavor framework, including matter effects.

In an open quantum system, a pure quantum state can evolve into a mixed state. For this reason we will use the density matrix formalism to describe the time evolution. The standard time evolution of a density matrix ρ is given by the Liouville-von Neumann equation. The decoherence effects can be parametrized by an additional term $\mathcal{D}[\rho]$. Thus, the equation for the time evolution of the density matrix is given by [15]

$$\frac{d}{dt}\rho = -i[H, \rho] - \mathcal{D}[\rho]\,, \tag{2.12}$$

where H is the full Hamiltonian in matter as defined in Equation 2.10.

Equation 2.12 can be simplified by imposing the following physical restrictions:

- Probabilities should be conserved for any initial state.
  This is equivalent to demanding that the time evolution should be trace-preserving.
- Probabilities should always remain positive.
  This means that the eigenvalues of ρ, which are interpreted as probabilities, should remain positive. This requirement is fulfilled when $\mathcal{D}[\rho]$ is completely positive [13].

  With the conditions of trace conservation and complete positivity, the decoherence term can be written in the so-called *Lindblad* form [15]

  $$\mathcal{D}[\rho] = \sum_m (\{\rho, D_m D_m^\dagger\} - 2D_m \rho D_m^\dagger)\,, \tag{2.13}$$

  where the D_m are general complex matrices.
- The von Neumann entropy $S = -\operatorname{Tr}[\rho \ln(\rho)]$, should increase with time.
  This is ensured by taking the D_m to be Hermitian, so $D_m = D_m^\dagger$ [15].
- The average energy of the neutrino system should be conserved.
  This can be expressed as

  $$\frac{d}{dt}\operatorname{Tr}(H\rho) = 0\,. \tag{2.14}$$

  More specifically, since H is the Hamiltonian in matter, this last condition requires that the energy is conserved in the effective mass basis, including matter effects. As H changes with the matter density, this implies that decoherence is modified by matter interactions and, furthermore, it is modified in a way that it will ensure energy conservation. This is not a well established assumption. However, non-unitary evolution with energy conservation is characteristic for decoherence, while energy loss is characteristic for dissipation [16]. In this work, we will only consider systems without dissipative effects where energy conservation holds.

  Assuming that the energy is conserved simplifies the calculation of the time evolution since in this case [15]

  $$[H, D_m] = 0\,, \tag{2.15}$$

which means that H and the D_m can be diagonalized simultaneously in the same basis. Thus, the D_m can be written in the effective mass basis as

$$\tilde{D}_m = \tilde{U}^\dagger D_m \tilde{U} = \mathrm{diag}(\tilde{d}_m^1, \tilde{d}_m^2, \tilde{d}_m^3)\,, \tag{2.16}$$

analogous to Equation 2.11.

- Finally, the $\tilde{d}_m^i$ should be independent of the matter density and remain constant as the neutrinos propagate through the Earth. Note that this does not mean that decoherence is independent of matter effects. The matrices D_m still depend on matter effects through $\tilde{U}$.

With the conditions discussed above, Equation 2.12 can be written as

$$\frac{d}{dt}\rho = -i[H,\rho] - \sum_m (\{\rho, D_m^2\} - 2D_m\rho D_m). \tag{2.17}$$

In the following, this equation is solved for the case of uniform matter. Knowing the time evolution of ρ, the oscillation probabilities including decoherence effects can be calculated.

2.2.1 Decoherence effects in uniform matter

To solve Equation 2.17 in uniform matter, we need to change to the effective mass basis. Using $\rho = \tilde{U}\tilde{\rho}\tilde{U}^\dagger$, $H = \tilde{U}\tilde{H}\tilde{U}^\dagger$, and $D_m = \tilde{U}\tilde{D}_m\tilde{U}^\dagger$, we obtain

$$\frac{d}{dt}(\tilde{U}\tilde{\rho}\,\tilde{U}^\dagger) = -i\tilde{U}[\tilde{H},\tilde{\rho}]\tilde{U}^\dagger - \sum_m \tilde{U}(\{\tilde{\rho}, \tilde{D}_m^2\} - 2\tilde{D}_m\tilde{\rho}\tilde{D}_m)\tilde{U}^\dagger\,. \tag{2.18}$$

In general, the $\tilde{U}^{(\dagger)}$ are time dependent, since the matter density can change along the propagation path of the system. Thus, the left-hand side is of Equation 2.18 reads

$$\frac{d}{dt}(\tilde{U}\tilde{\rho}\tilde{U}^\dagger) = \left(\frac{d}{dt}\tilde{U}\right)\tilde{\rho}\tilde{U}^\dagger + \tilde{U}\left(\frac{d}{dt}\tilde{\rho}\right)\tilde{U}^\dagger + \tilde{U}\tilde{\rho}\left(\frac{d}{dt}\tilde{U}^\dagger\right)\,. \tag{2.19}$$

Multiplying with $\tilde{U}^\dagger$ from the left and with $\tilde{U}$ from the right, Equation 2.18 can be rewritten as

$$\frac{d}{dt}\tilde{\rho} = -i[\tilde{H},\tilde{\rho}] - \sum_m (\{\tilde{\rho}, \tilde{D}_m^2\} - 2\tilde{D}_m\tilde{\rho}\tilde{D}_m) - \tilde{U}^\dagger\left(\frac{d}{dt}\tilde{U}\right)\tilde{\rho} - \tilde{\rho}\left(\frac{d}{dt}\tilde{U}^\dagger\right)\tilde{U}\,. \tag{2.20}$$

In uniform matter, the last two terms vanish, as the $\tilde{U}^{(\dagger)}$ are not time dependent. In this case, the time evolution is given by

$$\frac{d}{dt}\tilde{\rho} = -i[\tilde{H},\tilde{\rho}] - \sum_m (\{\tilde{\rho}, \tilde{D}_m^2\} - 2\tilde{D}_m\tilde{\rho}\tilde{D}_m)\,. \tag{2.21}$$

Since $\tilde{H}$ and $\tilde{D}_m$ are diagonal in the effective mass basis, Equation 2.21 can be written for the components of $\tilde{\rho}$ as

$$\begin{aligned}\frac{d}{dt}\tilde{\rho}_{ij} &= -i\,\tilde{\rho}_{ij}(\tilde{E}_i - \tilde{E}_j) - \sum_m \tilde{\rho}_{ij}[(\tilde{d}_m^i)^2 + (\tilde{d}_m^j)^2 - 2\tilde{d}_m^i\tilde{d}_m^j] \\ &= \tilde{\rho}_{ij}(-i\,\Delta\tilde{E}_{ij} - \gamma_{ij}),\end{aligned} \tag{2.22}$$

where $\Delta\tilde{E}_{ij} = \tilde{E}_i - \tilde{E}_j$ and we defined the decoherence parameter

$$\gamma_{ij} = \sum_m (d_m^i - d_m^j)^2\,. \tag{2.23}$$

So, the time evolution in uniform matter is given by

$$\tilde{\rho}_{ij} = \tilde{\rho}_{ij}(0)\,e^{-i\Delta\tilde{E}_{ij}t - \gamma_{ij}t}\,, \tag{2.24}$$

where $\tilde{\rho}_{ij}(0)$ is determined by the initial conditions of the system. For example, for a source that produces only neutrinos of flavor α, the initial condition is given by

$$\tilde{\rho}_{ij}^{(\alpha)}(0) = \langle\nu_i|\,\hat{\rho}^{(\alpha)}(0)\,|\nu_j\rangle = \tilde{U}_{\alpha i}\tilde{U}_{\alpha j}^*\,, \tag{2.25}$$

where $\hat{\rho}^{(\alpha)}(t) = |\nu_\alpha(t)\rangle\,\langle\nu_\alpha(t)|$.

The oscillation probabilities in the presence of decoherence effects therefore read [15] [1]

$$\begin{aligned}P(\nu_\alpha \to \nu_\beta) &= \mathrm{Tr}\Big[\hat{\rho}^{(\alpha)}(t)\hat{\rho}^{(\beta)}(0)\Big] \\ &= \langle\nu_\beta|\,\hat{\rho}^{(\alpha)}(t)\,|\nu_\beta\rangle \\ &= \sum_{i,j}\tilde{U}_{\beta i}^*\tilde{U}_{\beta j}\,\langle\nu_i|\,\rho^{(\alpha)}(t)\,|\nu_j\rangle \\ &= \sum_{i,j}\tilde{U}_{\beta i}^*\tilde{U}_{\beta j}\tilde{\rho}_{ij}^{(\alpha)}(t) \\ &= \sum_{i,j}\tilde{U}_{\alpha i}\tilde{U}_{\beta i}^*\tilde{U}_{\alpha j}^*\tilde{U}_{\beta j}e^{-i\Delta\tilde{E}_{ij}t - \gamma_{ij}t}\,.\end{aligned} \tag{2.26}$$

Comparing this to the case without decoherence effects (see Equation 2.5), it becomes apparent that the only difference is the presence of a damping term $e^{-\gamma_{ij}t}$ in the oscillation probabilities. This means that decoherence suppresses neutrino oscillations. The strength of the damping depends only on the decoherence parameter.

The decoherence parameter itself may depend on the neutrino energy as

$$\gamma_{ij} = \gamma_{ij}^0\left(\frac{E}{\mathrm{GeV}}\right)^n\,. \tag{2.27}$$

[1] Note that a different convention of the relation between mass and flavor states is used here, so the probabilities have to be complex conjugated to equal the results in this work.

In this work, the cases $n = 0, \pm 1, \pm 2$ are considered. Also, from Equation 2.23 it can be seen that the γ_{ij} are not independent of each other. To simplify the analysis, a typical approach for decoherence studies is to distinguish three representative cases where one of the γ_{ij} is set to zero and the other two are equal. The representative cases are:

- Atmospheric limit: $\gamma_{21} = 0$ ($\gamma_{32} = \gamma_{31}$),
- Solar limit 1: $\gamma_{32} = 0$ ($\gamma_{21} = \gamma_{31}$),
- Solar limit 2: $\gamma_{31} = 0$ ($\gamma_{21} = \gamma_{32}$).

In [15] it was shown that these limits correspond to the most conservative bounds of the more general case that all γ_{ij} are different from zero. In each of the limits, decoherence effects are dominated by only one parameter that will be denoted as γ.

2.2.2 Decoherence effects in non-uniform matter

As already mentioned, the neutrinos that are used for oscillation studies have passed through the Earth in order to avoid the large background of atmospheric muons coming from above. The matter density inside the Earth's mantle and core is not uniform. For non-uniform matter, the last two terms in Equation 2.20 do not vanish, since $\tilde{U}^{(\dagger)}$ is now time dependent. This makes solving the equation for the time evolution of ρ more complicated.

To avoid this complication, the matter profile is divided into layers of constant density, as indicated in Figure 2.2. This is a well established approximation for neutrinos that travel through the Earth. In each layer M, the time evolution is simply given by [15]

$$\tilde{\rho}_{ij}^{M} = \tilde{\rho}_{ij}^{M}(t_{M,0})\, e^{-i\Delta\tilde{E}_{ij}^{M} t - \gamma_{ij}\Delta t_M}\,, \tag{2.28}$$

where $\Delta t_M = t_M - t_{M,0}$ is the time for the propagation through layer M. To match the evolution at the boundaries of two layers A and B correctly, it is necessary that [15]

$$\rho_{\alpha\beta}^{A}(t_A) = \rho_{\alpha\beta}^{B}(t_{B,0})\,, \tag{2.29}$$

where the transformation to the flavor basis can be done using

$$\rho_{\alpha\beta}^{M}(t_M) = [\tilde{U}^{M}\tilde{\rho}^{M}(t_M)(\tilde{U}^{M})^{\dagger}]_{\alpha\beta}\,. \tag{2.30}$$

With this procedure the oscillation probability can be calculated for an arbitrary number of layers. The more layers are added, the more accurate non-uniform matter can be described.

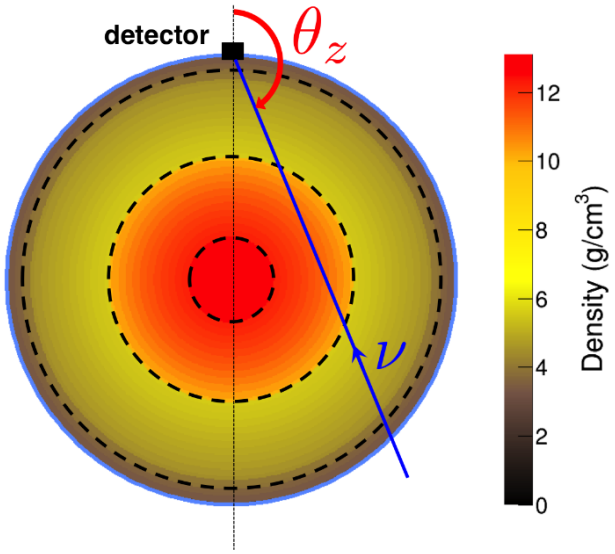

Figure 2.2: Earth model with 42 layers of different densities. The zenith angle Θ_Z describes the path of the neutrino from production to detection site. The dashed lines indicate the boundaries of the three major compositional layers: inner core, outer core, and silicate Earth [17].

2.3 Oscillation research with atmospheric neutrinos

In order to understand the results obtained with neutrino detectors correctly, it is important to describe the expected neutrino flux as precisely as possible. Therefore, the most important properties of the atmospheric neutrino flux are briefly discussed in this chapter. Afterwards, the detection principle of Cherenkov detectors and the setup of ARCA and ORCA is explained.

2.3.1 Properties of atmospheric neutrinos

When a cosmic ray particle interacts with the particles in the Earth's atmosphere, secondary particles emerge from the interaction. In the subsequent decay of the secondary particles, neutrinos are produced. At low energies, this occurs mainly via the decay of pions and the subsequent decay of muons:

$$\begin{aligned} \pi^+ &\to \mu^+ + \nu_\mu \,, \\ \pi^- &\to \mu^- + \bar{\nu}_\mu \,, \\ \mu^+ &\to e^+ + \nu_e + \bar{\nu}_\mu \,, \\ \mu^- &\to e^- + \bar{\nu}_e + \nu_\mu \,. \end{aligned} \tag{2.31}$$

Also the decay of kaons contributes to the conventional flux at low energies. At higher energies, neutrinos emerge from the decay of heavier mesons containing a charm quark. This is called the prompt component of the flux. Assuming that the decays in Equation 2.31

happen at equal rates, there should be approximately twice as many muon neutrinos as electron neutrinos. However, this is only true for low energies of a few GeV. As the energy increases, more and more muons reach the ground without decaying. Therefore, the ratio of muon to electron neutrinos rises with increasing energy. The ratio is shown as a function of energy and arrival direction in Figure 2.3. Also, as cosmic rays consist mainly of protons, in the first interaction with the atmosphere more π^+ than π^- are produced. As a result, there should be more ν_μ than $\bar{\nu}_\mu$, and more ν_e than $\bar{\nu}_e$, as can be seen in Figure 2.4.

Not only the composition of the atmospheric neutrino flux is important, but also the energy dependence and the absolute value of the flux. As the cosmic ray spectrum follows a power law, also the neutrino flux follows a power law:

$$n(E) \propto E^{-\alpha}\,, \tag{2.32}$$

where $\alpha \approx 3$. The measured spectrum is shown in Figure 2.5. It can be seen that specially at high energies the uncertainties of the flux are still large. The uncertainties of the flavor ratios, the ratio of neutrinos and anti-neutrinos, and the uncertainty of the power-law index α should be taken into account to make predictions about detector sensitivities more realistic.

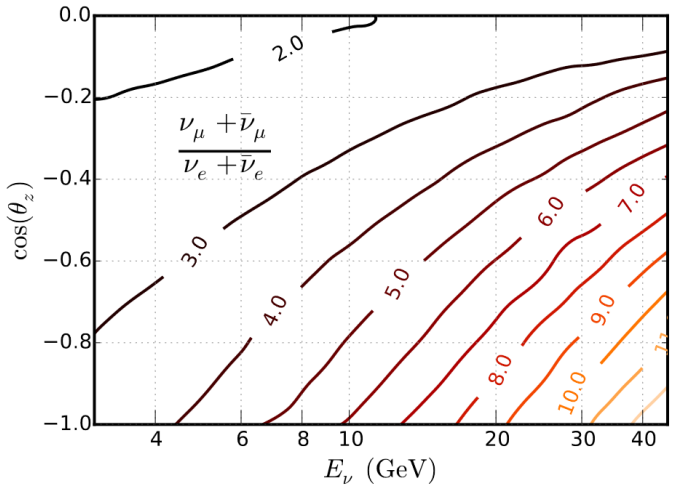

Figure 2.3: Ratio of muon to electron neutrinos as a function of energy and neutrino arrival direction for neutrinos that cross the Earth [18].

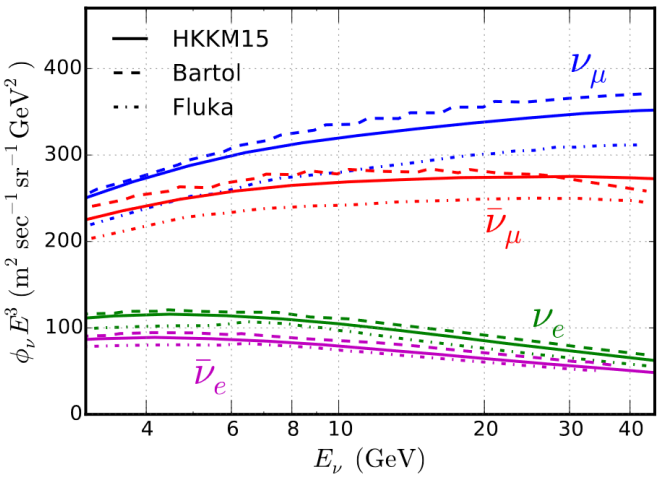

Figure 2.4: Predicted atmospheric neutrino fluxes per flavor [18].

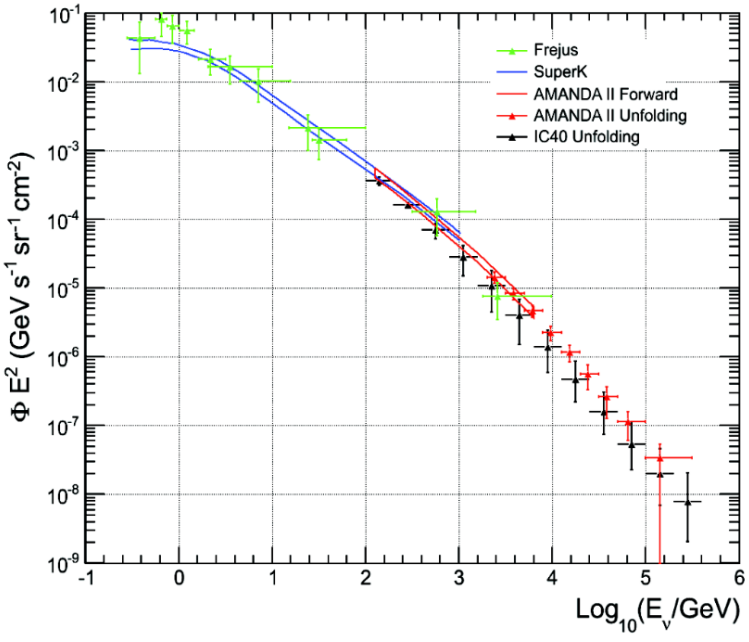

Figure 2.5: Measured spectrum of atmospheric neutrinos [19].

2.3.2 Neutrino detection with Cherenkov detectors

Since neutrinos only interact via the weak interaction, they can not be detected directly. Instead, the particles emerging from a neutrino interaction are detected. For atmospheric neutrinos, the dominant interaction process is scattering on a nucleon X:

$$\begin{aligned} \nu_e + X &\rightarrow e + Y\,, \\ \nu_\mu + X &\rightarrow \mu + Y\,, \end{aligned} \tag{2.33}$$

where Y is the hadronic final state. For energies above 5 GeV the nucleus breaks up in the process and many hadronic particles are produced. The final state particles are relativistic, which means that they induce Cherenkov light when they travel through a medium. As the signatures of of electrons, muons, and hadrons differ from each other, the initial flavor of the neutrino can be determined from the intensity and angular distribution of the observed Cherenkov light. The leftmost diagram in Figure 2.6 shows the CC interaction of ν_e with a nucleon as well as the subsequent electromagnetic and hadronic shower. In a ν_μ interaction, the emerging muon produces a track-like event. The signature of a ν_τ are two shower-like events: one from the neutrino interaction and one from the decay of the τ particle which has a very short lifetime. The rightmost diagram in Figure 2.6 shows a NC interaction of any flavor, which results into a hadronic jet and no other traces.

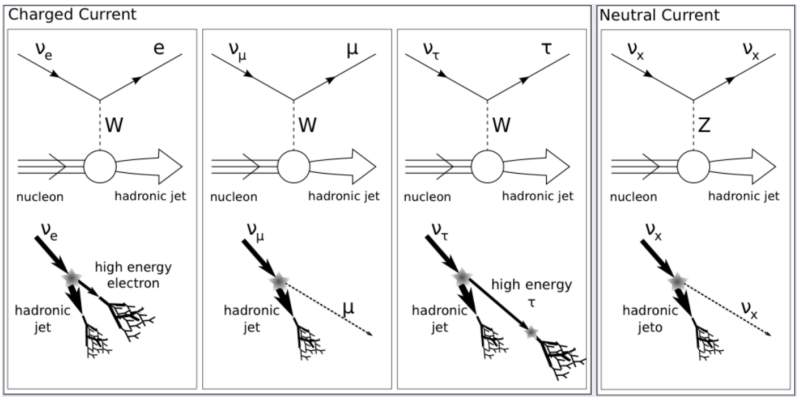

Figure 2.6: Feynman diagrams for neutrino interactions on a nucleon and signatures for each flavor [20].

2.3.3 Oscillation research with KM3NeT

KM3NeT/ARCA and KM3NeT/ORCA are water Cherenkov detectors which are under construction in the Mediterranean sea (see [5]). Water is used as the medium for the neutrino interactions, as well as for the production of Cherenkov light. The light is then detected with PMTs that are fixed inside digital optical modules (DOMs), as shown in Figure 2.7 on the right-hand side. The left-hand side of Figure 2.7 shows a detection string. Each of the detection strings hosts 18 DOMs.

Figure 2.7: Detection string (left) and digital optical module (DOM) for KM3NeT [5].

ORCA will consist of a collection of 115 strings with a relatively small spacing of 20 m between the stings and a spacing of 9 m between the DOMs. With the small spacing, low energy neutrinos of just a few GeV can be detected, even though they produce only a small amount of Cherenkov light. ORCA will have an instrumented volume of 1 Mt.
ARCA will consist of two building blocks of 115 detection strings each. For ARCA, the spacing between single DOMs and detection strings is much larger with 36 m between the DOMs and 90 m between the stings. ARCA is designed to target high energy astrophysical neutrinos. These high energy neutrinos produce more Cherenkov light in a single interaction, but their flux is lower, so that a bigger instrumented volume is needed for the detection. Naturally, ARCA can detect atmospheric neutrinos as well. In total, ARCA will have an instrumented volume of 1 Gt.

The correct identification of the neutrino flavors is crucial for oscillation experiments, as the number of detected neutrinos per flavor is compared to the expectation. In this way, either the survival probability $P(\nu_\alpha \to \nu_\alpha)$, or the disappearance probability $P(\nu_\alpha \to \nu_x)$ for a neutrino of initial flavor α can be measured.

For atmospheric neutrinos, both, ν_e and ν_μ contribute to the flux and both flavors can be detected and distinguished from each other by the event signatures. The KM3NeT detectors can identify track-like and shower-like events based on the event topology. Since the reconstruction strategy depends on the event topology, dedicated algorithms are used for the reconstruction of track- and shower-like events. However, some concepts are applicable for all events (see [17]):

First, the hit selection discards hits that are very likely caused by optical background using space-time coincidences of different PMTs and DOMs.

For the remaining hits, the time residuals are determined. The time residual is the difference between the observed hit time and the hit time predicted from a hypothesized source. A function of the time residuals of all selected hits is minimized via a likelihood fit to determine either the interaction vertex position or the track direction.
To find a suitable starting point for the likelihood fit, a prefit scan selects the best performing points by scanning over a grid.

The track reconstruction algorithm maximizes the likelihood that the pattern observed with PMTs is consistent with Cherenkov light emission from the fitted muon trajectory [5]. For the track-like events, the direction of the neutrino can be reconstructed with good precision. The direction is given by the zenith angle Θ_Z, where $\cos(\Theta_Z) = -1$ corresponds to a path directly though the center of the Earth as can be seen in Figure 2.2. The energy estimate is determined from the length of the track, which is calculated based on the first and last DOMs hits along the track [17]. For the track-like event, not all the Cherenkov light is radiated inside the detector, which makes the energy reconstruction less precise than for the shower-like events. For all detectors, the track reconstruction is done with the algorithm JGandalf.

For the shower-like events, the direction reconstruction is less precise, but the energy reconstruction is better than for a track. The shower reconstruction algorithm uses the spacial position of the PMTs and the arrival time of the hits to determine the position of the interaction vertex. The energy of the neutrino can be estimated from the amount of Cherenkov light. For this, the number of PMT hits within a certain time window of the expected Cherenkov light-front is used [5], where a spherical light emission is assumed. Hadronic showers can be distinguished from electromagnetic showers because they are less bright, as more energy goes into the production of particles. The direction of a shower-like event can be estimated from the average direction of the hits with respect to the vertex position [5]. The shower reconstruction algorithms that were used for the Monte Carlo samples considered in this work are Dusj and JShower for different configurations of ORCA and Aashower for ARCA.

The calculation of the expected rates of shower- and track-like events inside the detector is explained in the next chapter.

3 Analysis methods and Software

To calculate the expected number of events inside the detector, many computational steps are necessary: starting from input models of the neutrino flux and cross section, the oscillation probabilities inside the Earth are calculated and the detector response is modeled. In this work, the software package SWIM (see [17]) is used for the rate calculations as well as the calculation of the detector sensitivities. SWIM relies on the ROOT data analysis framework [21] and models the detector response based on Monte Carlo simulations. This chapter gives a short overview of the computation chain. Furthermore, the calculation of the detector sensitivities is explained.

3.1 Neutrino event rates

SWIM calculates the expected event rates at the detector site as a function of the reconstructed neutrino energy and zenith angle. The strategy for the calculation is illustrated in Figure 3.1, where the indicated steps are very general and not specific for SWIM. The input models for SWIM are the atmospheric neutrino flux, the interaction cross section, an Earth model and the density of the target nuclei at the detector site. For ORCA, the initial flux follows the simulations of M.Honda *et al.* [22]. For ARCA, a component of prompt neutrinos is added to the Honda flux.

To obtain the expected number of neutrinos for each flavor at the detector site, the oscillation probabilities need to be calculated for different trajectories through the Earth. The calculation is done with the software OscProb (see [23]) and follows the approach of layers of constant matter density discussed in subsection 2.2.2. The Earth model is given by the Preliminary Reference Earth Model (PREM) [24]. The more layers are added, the more accurate the matter density inside the Earth can be described, as can be seen in Figure 3.2. The Earth model used for this study consists of 425 layers.

As already seen in section 2.1, the oscillation probabilities depend on the energy E of a neutrino and the time of the propagation. The propagation time is given by the length of the path that a neutrino travels which depends solely on the zenith angle Θ_Z. Therefore, the probabilities are typically shown in dependence of E and $\cos(\Theta_Z)$. These two-dimensional histograms are called oscillograms. The binning of the oscillograms in OscProb follows the same scheme as in the interaction event histograms: the zenith angle is binned linearly in $\cos(\Theta_Z)$ while the energy bins have an equal logarithmic width. For ORCA, 40 bins are used for the the true energy ranging from 1 GeV to 100 GeV The zenith angle is binned linearly in $\cos(\Theta_Z)$ with 40 bins in the range $-1 < \cos(\Theta_Z) < 0$. The same binning is applied for ARCA, although for the zenith angle a finer binning may prove useful in future studies, since the directional reconstruction with ARCA is very accurate. The energy for ARCA ranges from 100 GeV to 10^6 GeV.

From the flux at the detector site and the interaction cross section the interaction rate is determined. To obtain the number of detected events the effective mass of the detector has to be taken into account. The effective mass is defined as [5]

$$M_{\text{eff}} = V_{\text{gen.}} \cdot \rho_{\text{water}} \cdot \frac{N_{\text{sel.}}}{N_{\text{gen.}}}\,, \tag{3.1}$$

where $V_{\text{gen.}}$ is the event generation volume, ρ_{water} is the density of sea water, $N_{\text{gen.}}$ is the number of generated events and $N_{\text{sel.}}$ is the number of events that are successfully reconstructed. A successful reconstruction requires that the event is processed by one of the reconstruction algorithms and passes the pre-PID cuts. The pre-PID cuts include a cut on the zenith angle $\cos(\Theta_Z) < 0$ in order to reduce the atmospheric muon background as well as quality cuts that are specific for each algorithm.

The next step is the particle identification (PID). This is done with a random decision forest [17] that returns a score $0 \leq p \leq 1$ for each event based on the event feature. The scores for the PID are [17]

- $p_{\text{bkg,noise}}$ for the rejection of pure noise events,
- $p_{\text{bkg},\mu}$ for the rejection of atmospheric muons that passed the pre-PID cuts,
- p_{track} for the distinction between track-like and shower-like events.

Using these scores, PID classes can be defined by first cutting on $p_{\text{bkg,noise}}$ and $p_{\text{bkg},\mu}$ and then classifying the remaining events with a cut on the track score p_{track}. In this work, different cuts on the track score were investigated where either two classes (tracks and showers) or three classes (tracks, showers and middles) were used. This is explained in more detail in chapter 5.

The last step in the computation chain is the application of the detector response. In SWIM, this is done with a response matrix that is calculated from the number $N_{\text{gen}}^{\text{MC}}$ of generated Monte Carlo events and the number $N_{\text{sel}}^{\text{MC}}$ of selected Monte Carlo events (see [17]). The generated events represent all simulated neutrino interactions and are characterized by the interaction channel ν_x, the true energy E, true zenith angle Θ_Z, and true inelasticity y. The selected events refer to all events that are successfully reconstructed by one of the reconstruction algorithms. These events are characterized by the measured energy E', the measured zenith angle Θ'_Z, and the measured inelasticity y', as well as a discrete event category i. The response matrix is then given by the ratio [17]

$$R^{[\nu_x \to i]}(E, \Theta_Z, y, E', \Theta'_Z, y') = \frac{N_{\text{sel}}^{\text{MC}}[\nu_x \to i](E, \Theta_Z, y, E', \Theta'_Z, y')}{N_{\text{gen}}^{\text{MC}}[\nu_x](E, \Theta_Z, y)}\,. \tag{3.2}$$

The detector response is applied to obtain the number of reconstructed events n_{reco}^i in a PID class i from the number of interacting events $n_{\text{int}}^{\nu_x}$ via [17]

$$n_{\text{reco}}^i(E', \Theta'_Z, y') = \sum_{\nu_x} \sum_{E, \Theta_Z, y} R^{[\nu_x \to i]}(E, \Theta_Z, y, E', \Theta'_Z, y') \cdot M_{\text{ref}} \cdot \frac{dn_{\text{int}}^{\nu_x}}{dM_{\text{eff}}}(E, \Theta_Z, y)\,. \tag{3.3}$$

Here, $dn_{\text{int}}^{\nu_x}/dM_{\text{eff}}$ is the number of interactions in channel ν_x per unit of target mass. The reference target mass $M_{\text{ref}} = \rho_{\text{water}} \cdot V_{\text{ref}}$ is calculated from the reference generation volume V_{ref}, which takes into account events which are generated outside the instrumented volume but can still be successfully reconstructed [17]. As this is especially important for high-energy track-like events, V_{ref} is an energy-dependent volume.

The reconstructed events n_{reco}^{i} are stored in histograms for each PID class, where in principle any number of PID classes i can be implemented. For the reconstructed events, 20 logarithmic bins in E' and 20 bins in $\cos(\Theta'_Z)$ were used for ORCA and ARCA. The inelasticity was reconstructed in four bins for ORCA, and one bin for ARCA. The histograms can then be used to calculate the detector sensitivity, as explained in the next section.

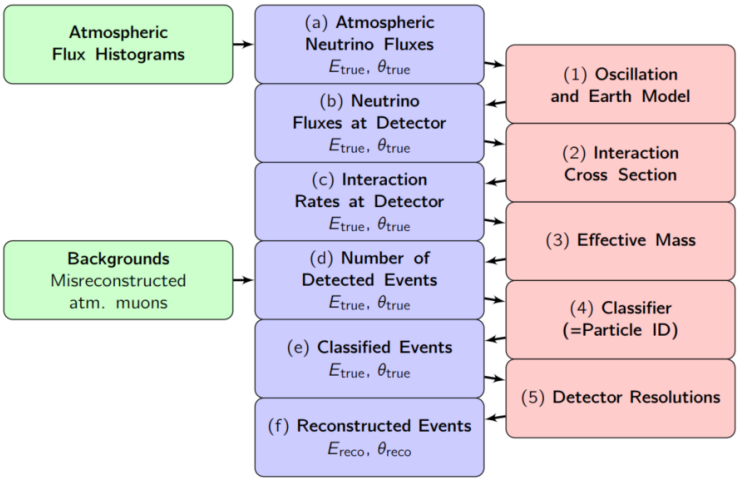

Figure 3.1: Flowchart showing the steps in the computation chain to obtain the expected neutrino events at the detector site [5]. The blue blocks show intermediate results while the red blocks indicate the steps between the intermediate results. The green blocks describe additional input.

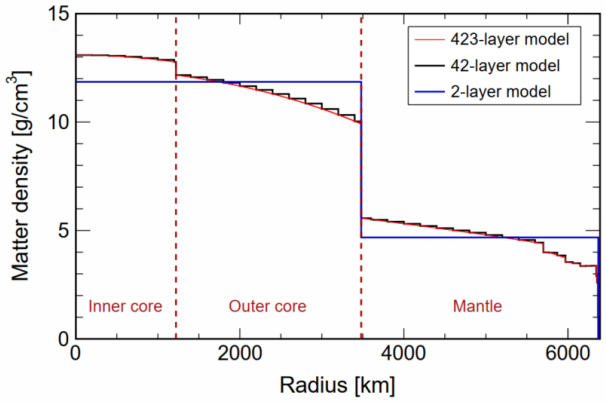

Figure 3.2: The Earth's matter density profile described by models with different numbers of layers [17].

3.2 Calculation of detector sensitivities

The calculation of sensitivities from reconstructed event histograms is based on the Asimov dataset approach [17]. This means that the average experiment is evaluated by setting all event rates to their expectation values $\mu_{\mathrm{H_k}}$. Here, the hypothesis H_0 corresponds to the case of no decoherence. This hypothesis is tested against a set of alternative hypotheses H_i $(i = 1, 2, 3, ...)$ that correspond to different strengths of decoherence effects.

When no prior knowledge about systematic parameters is taken into account, the $\Delta\chi^2$ function [17]

$$\Delta\chi^2 = \min_{\eta} \left[-2 \ln \mathcal{L}_{\mathrm{H}_0}(\mu_{\mathrm{H}_0}|\eta)\right] - \min_{\eta} \left[-2 \ln \mathcal{L}_{\mathrm{H}_i}(\mu_{\mathrm{H_i}}|\eta)\right] \tag{3.4}$$

is used for the hypothesis testing, where

$$\mathcal{L}_{\mathrm{H}_k} = \prod_{j=0}^{N_{\mathrm{classes}}-1} \prod_{b=0}^{N_{\mathrm{bins}}-1} \exp\left[-(\mu_{\mathrm{H}_k})_b^j\right] \frac{[(\mu_{\mathrm{H}_k})_b^j]^{n_b^j}}{n_b^j!} \tag{3.5}$$

is the binned statistical likelihood for all PID classes and all bins in energy, zenith angle and Bjorken-y. The minimization of the $\Delta\chi^2$ function is done over a set of systematic uncertainties denoted as η. This approach assumes that the expected number of events in each bin follows Poisson statistics.

In practice, the term

$$\Delta\chi^2_{\mathrm{stat}} = \sum_{j=0}^{N_{\mathrm{classes}}-1} \sum_{b=0}^{N_{\mathrm{bins}}-1} \left[2\left(\mu_{\mathrm{H}_0} - \mu_{\mathrm{H}_i} + n_b^j \ln\left(\frac{\mu_{\mathrm{H}_i}}{\mu_{\mathrm{H}_0}}\right)\right)\right] \tag{3.6}$$

is minimized in ROOT by Minuit 2. This is a minimization package foreseen for statistical analysis [25]. It provides different minimization methods, where in this work `MnMigrad` was used (see [26]), which can handle interactions between the parameters in η. Put simply, the fit tries to match the number of counts in the model with decoherence and the number of counts in the model without decoherence for each bin.

The $\Delta\chi^2$ function can also be written as

$$\Delta\chi^2 = \min_{\eta} \left[\Delta\chi^2_{\mathrm{stat}}\right] \tag{3.7}$$

which gives a measure for the remaining discrepancy between the two models after the fit has converged. As different strengths of decoherence effects are considered, $\Delta\chi^2$ becomes a function of the decoherence parameter γ.

The considerations above have not taken into account any prior knowledge about the systematic parameters. However, some parameters are better constrained by other experiments than by KM3NeT. To counteract the possibility that the fit finds minima with values that are far from the values determined by other experiments, some parameters are constrained by priors. It is assumed that these parameters follow a Gaussian distribution.

In practice, penalty terms $\Delta\chi^2_{\text{syst}}$ are added to $\Delta\chi^2_{\text{stat}}$. The bigger the discrepancy between the prior and the value determined by the fit is, the bigger the penalty term becomes. The total $\Delta\chi^2$ function reads

$$\Delta\chi^2_{\text{tot}} = \min_{\eta} \left[\Delta\chi^2_{\text{stat}} + \Delta\chi^2_{\text{syst}}\right]. \tag{3.8}$$

The significance to exclude decoherence effects is then given by [17]

$$S = \sqrt{|\Delta\chi^2_{\text{tot}}|}\,. \tag{3.9}$$

4 Calculated oscillation probabilities

In this chapter, the oscillation probabilities calculated with OscProb are presented. OscProb consists of a set of classes aimed at the computation of exact neutrino oscillation probabilities for different models [23]. The available models include for example standard neutrino oscillations for three families or any number of neutrino flavours, oscillations with Lorentz Invariance Violation, neutrino decay or absorption, and oscillations with decoherence effects. The muon and electron neutrino survival probabilities with decoherence effects are discussed and compared to the case of standard oscillations. Furthermore an approximation of the distribution of track-like events with decoherence is shown.

4.1 Survival probabilities

Recall that the three representative cases for oscillations with decoherence effects are

- Atmospheric limit: $\gamma_{21} = 0$ ($\gamma_{32} = \gamma_{31}$),
- Solar limit 1: $\gamma_{32} = 0$ ($\gamma_{21} = \gamma_{31}$),
- Solar limit 2: $\gamma_{31} = 0$ ($\gamma_{21} = \gamma_{32}$),

and the decoherence parameter may depend on the neutrino energy as

$$\gamma_{ij} = \gamma_{ij}^0 \left(\frac{E}{\text{GeV}} \right)^n ,$$

where $n = 0, \pm 1, \pm 2$.

Figure 4.1 shows the muon neutrino survival probability for all three representative cases for $n = 0$, as well as the standard oscillations case for neutrinos that travel directly through the center of the earth[2]. As discussed in section 2.2, decoherence introduces a damping term in the oscillation probabilities. The damping can be seen up to an energy of $E_\nu \approx 100\,\text{GeV}$. At higher energies, standard neutrino oscillations vanish completely. Nevertheless, here it becomes apparent that decoherence can also be probed at $E_\nu > 100\,\text{GeV}$ due to an overall shift in the probabilities.

In [15], the equivalences

$$\begin{aligned} (\text{Atm. limit})^{\text{NH}} &\leftrightarrow (\text{Solar limit2})^{\text{IH}} \\ (\text{Solarlimit2})^{\text{NH}} &\leftrightarrow (\text{Atm. limit})^{\text{IH}} \\ (\text{Solar limit2})^{\text{NH}} &\leftrightarrow (\text{Solar limit1})^{\text{IH}} \end{aligned} \tag{4.1}$$

[2]The strength of the decoherence effects was set to a constant value $\gamma_{ij}^0 = 10^{-23}\,\text{GeV}$ for all plots shown in this chapter.

for $E_\nu \geq 15\,\mathrm{GeV}$ were identified. These equivalences can also be seen in Figure 4.1. We will later see that they are also apparent in the detector sensitivities.

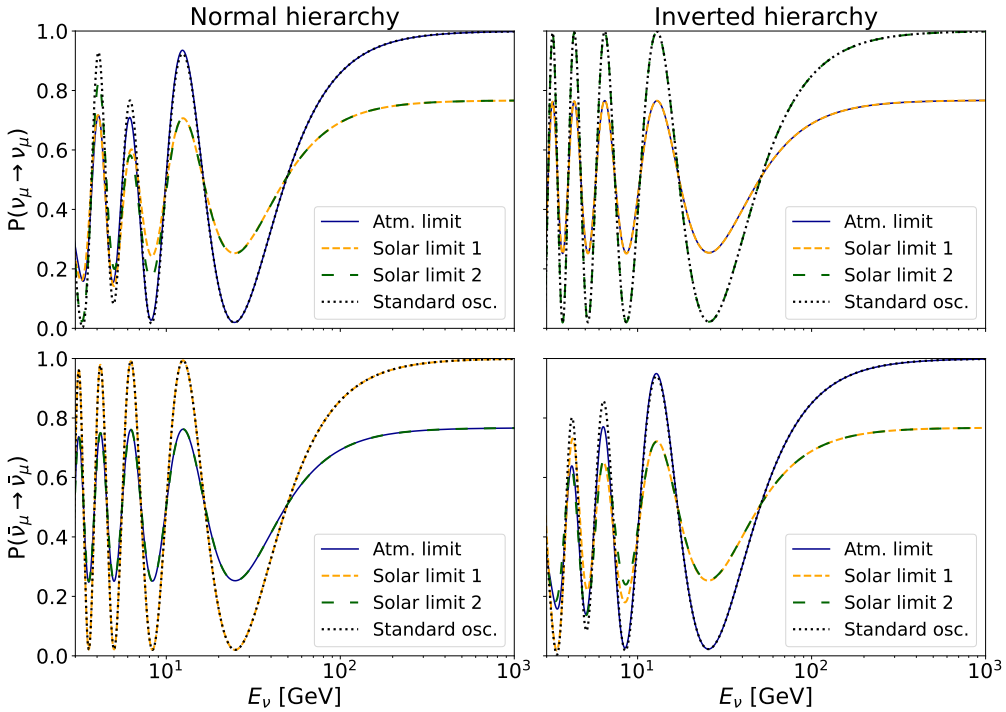

Figure 4.1: Oscillation probabilities for neutrinos (upper panels) and anti-neutrinos (lower panels) that travel through the center of the Earth for normal (left panels) and inverted (right panels) hierarchy for $n = 0$.

The dependence of the muon neutrino survival probability on the zenith angle is shown in Figure 4.2 for standard oscillations and for all limits, assuming normal hierarchy. While the Atmospheric limit does not differ too much from standard oscillations, the contrast of the oscillograms for Solar limit 1 and Solar limit 2 is smaller and the discrepancy between these limits and the standard oscillation case is bigger. This can be seen more distinctly in Figure 4.4, where the difference between standard oscillations and the individual limits is shown for both hierarchies for muon neutrinos ($\mathrm{P}_{\mu\mu}$) and anti-neutrinos ($\mathrm{P}_{\bar{\mu}\bar{\mu}}$). From Figure 4.4 it becomes apparent that the impact of decoherence effects for the representative cases depends strongly on the mass hierarchy and on whether neutrinos or anti-neutrinos are considered.
The same is true for electron neutrinos, for which the survival probability for normal hierarchy is shown in Figure 4.3. At low energies around 7 GeV and for $\cos(\Theta_Z) \leq -0.6$ the MSW effect can be seen for ν_μ ($\bar{\nu}_\mu$) for NH (IH). This is an energy dependent matter effect that induces a resonant behavior in oscillations for neutrinos in the case of normal hierarchy and for anti-neutrinos in the case of inverted hierarchy. When the MSW effect is present, the difference between the standard oscillation case and the three limits is of the same order of magnitude as in the muon survival probability. This can be seen in Figure 4.5 where the survival probabilities for electron neutrinos (P_{ee}) and anti-neutrinos ($\mathrm{P}_{\bar{e}\bar{e}}$) are

shown. When the MSW effect is not present, the difference between standard oscillations and the limits is about an order of magnitude smaller (note the different scaling in the color bars in Figure 4.5).

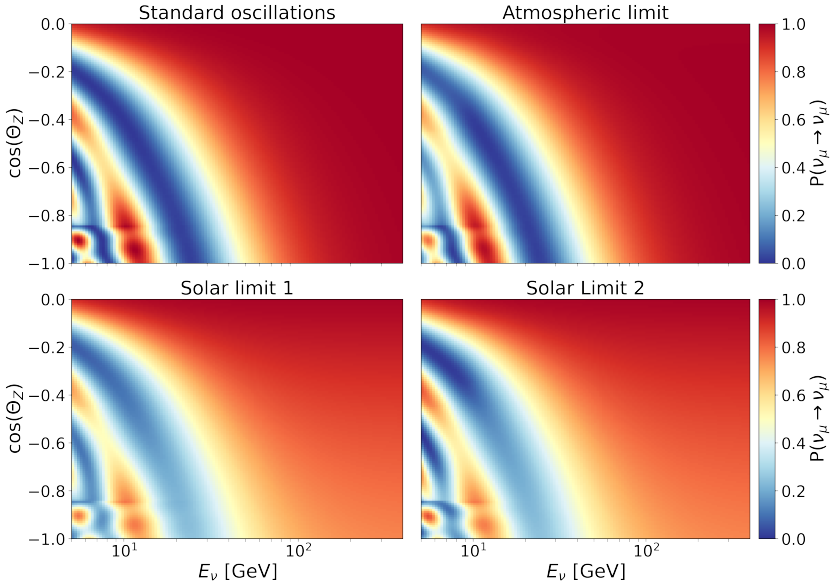

Figure 4.2: Oscillograms for the muon neutrino survival probability for NH and $n = 0$.

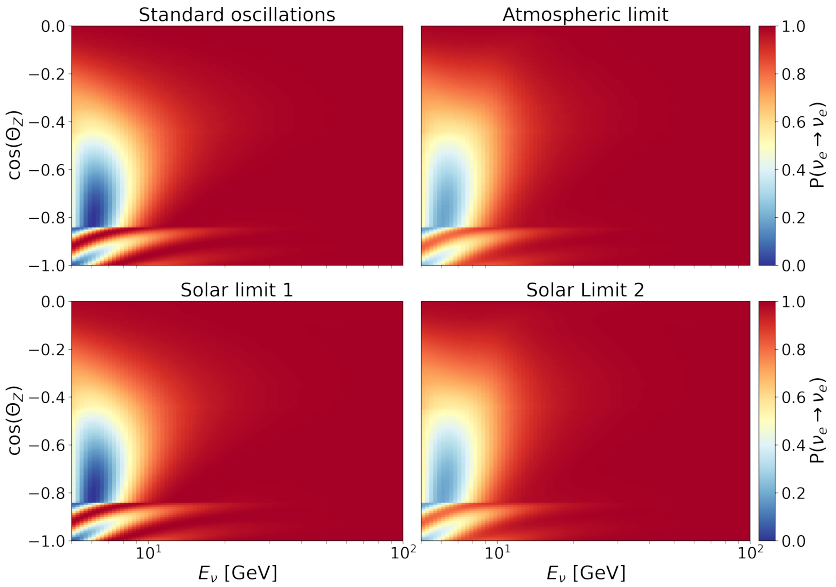

Figure 4.3: Oscillograms for the electron neutrino survival probability for NH and $n = 0$.

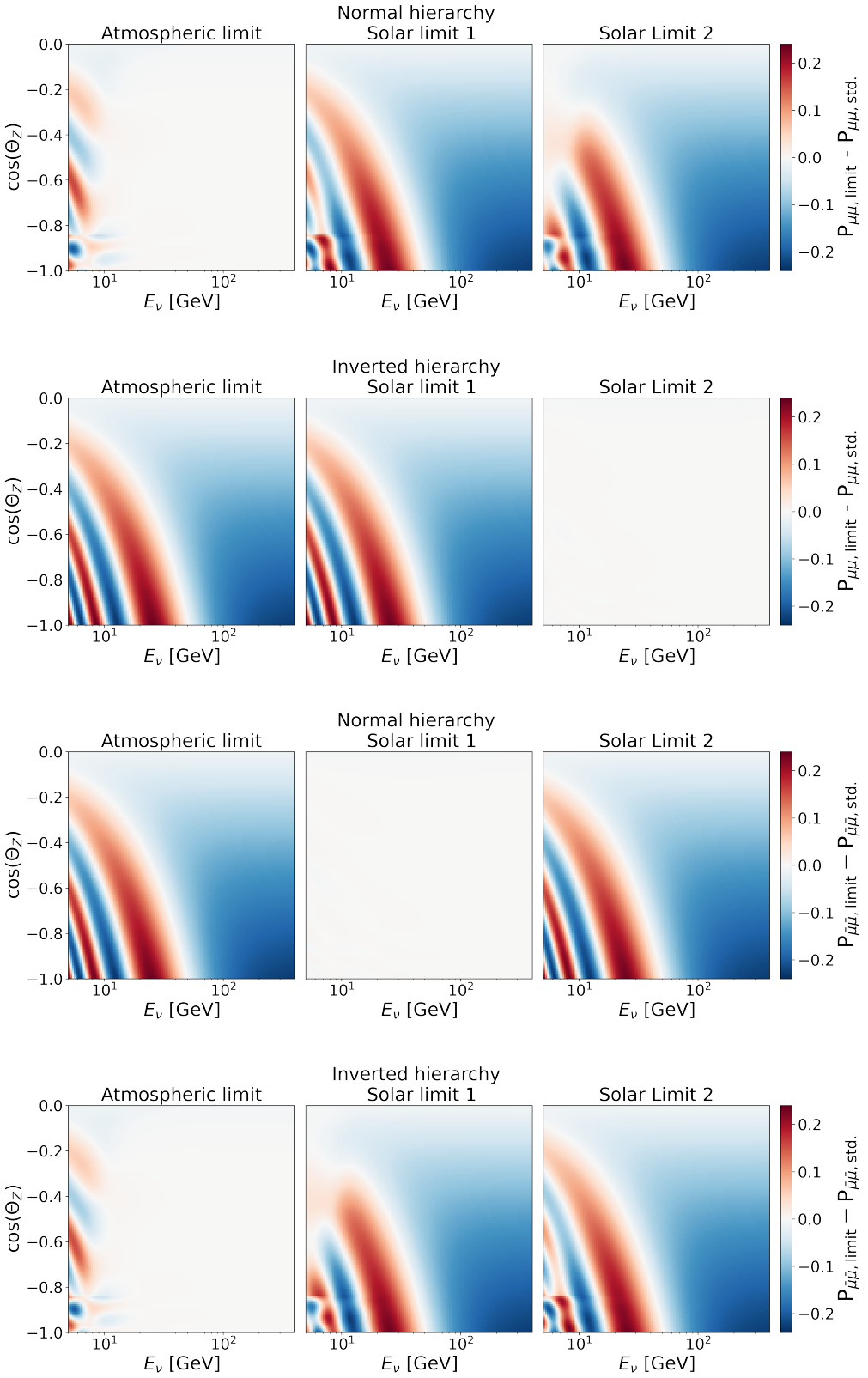

Figure 4.4: Difference between standard oscillations and the three limits in the muon neutrino and anti-neutrino survival probability.

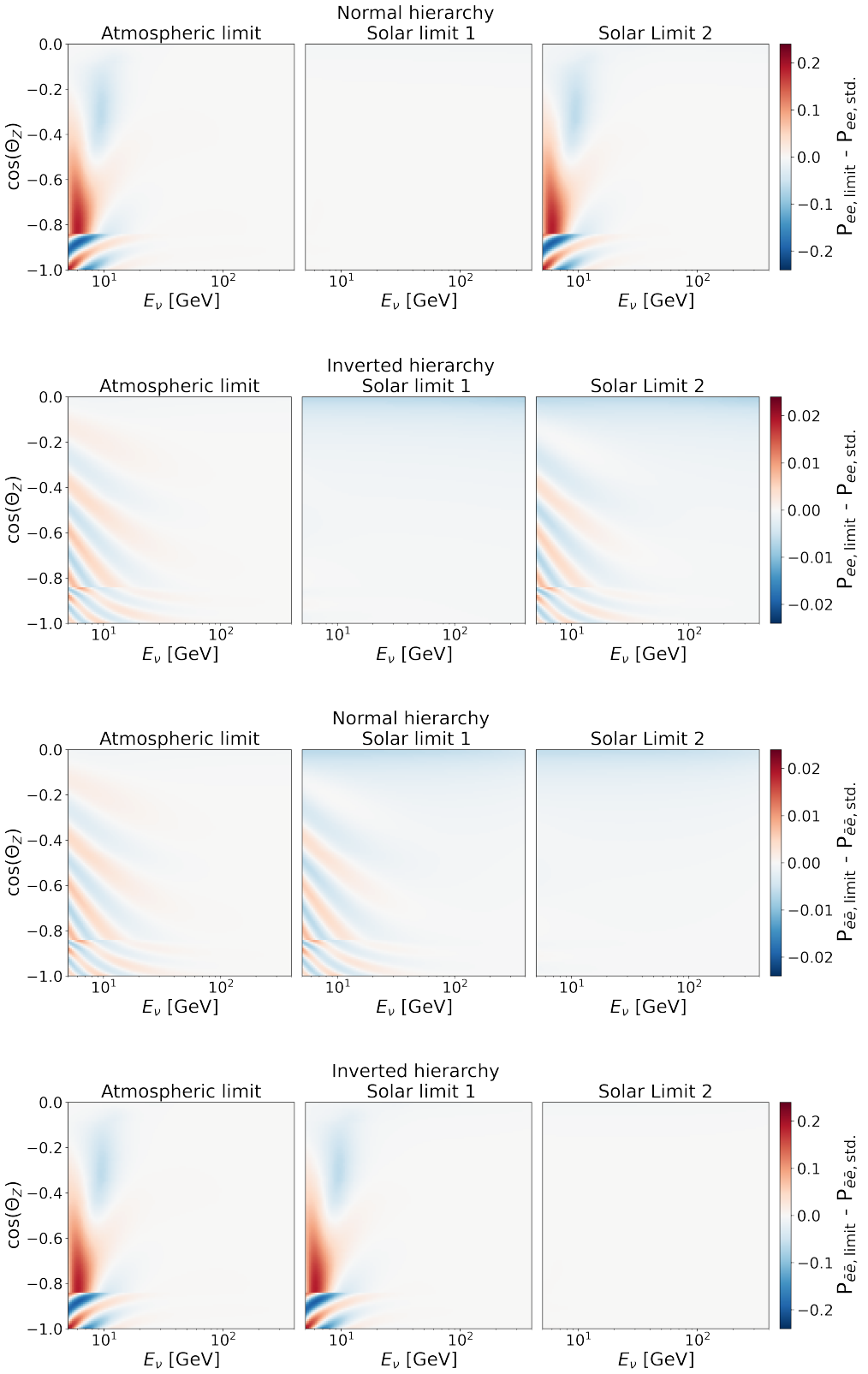

Figure 4.5: Difference between standard oscillations and the three limits in the electron neutrino and anti-neutrino survival probability.

4.2 Decoherence in track-like events

To find out for which limit the highest sensitivity is expected, it is useful to investigate the distribution of track-like events at the detector site. In KM3NeT, both, neutrinos and anti-neutrinos are detected and can not be distinguished from each other in individual interactions. To obtain an estimate of the distribution of track-like events, the overall probability of detecting a muon (anti-)neutrino is calculated as

$$P_{\text{track}} = P(\nu_\mu \to \nu_\mu) + \frac{1}{2}P(\bar{\nu}_\mu \to \bar{\nu}_\mu) + \frac{1}{2}P(\nu_e \to \nu_\mu) + \frac{1}{4}P(\bar{\nu}_e \to \bar{\nu}_\mu)\,. \tag{4.2}$$

This approach is motivated by the fact that the cross-section for neutrinos is about twice as big as the cross-section for anti-neutrinos. Furthermore, there are about twice as many muon neutrinos as electron neutrinos in the initial atmospheric neutrino flux at low energies. At higher energies, where this approximation is no longer adequate, the oscillations from electron to muon neutrinos vanish at any rate [3].
The distribution of track-like events is more suitable than the survival probabilities for the prediction of detector sensitivities, since there is a one-to-one correspondence between the cases shown here, and the cases for which the sensitivities are calculated.

The difference between standard oscillations and the limits in P_{track} for $n = 0$ is shown in Figure 4.6. Solar limit 2 for inverted hierarchy has the lowest contrast, since only muon anti-neutrinos contribute here. The same applies for the distribution of track-like events for $n = -2$ (see Figure 4.7) and $n = 2$ (see Figure 4.8). Thus, this is the case for which the lowest sensitivity is expected.
For $n = -2$, decoherence effects are visible only up to an energy of $E_\nu \approx 12\,\text{GeV}$ and the contrast is generally lower than for $n = 0$. For $n = 2$, it is apparent that decoherence effects are stronger than for $n = 0$, especially for small zenith angles.
Note, that γ_{ij}^0 was always set to the same constant value in order to compare the models with different energy dependencies to each other. For $n = 2$ the current bounds on the decoherence parameter are about nine orders of magnitude smaller, as we will see in the next section.

[3] In the calculation of the detector sensitivities no such approximations are made but instead an energy dependent model for the cross-sections and flavor composition is used.

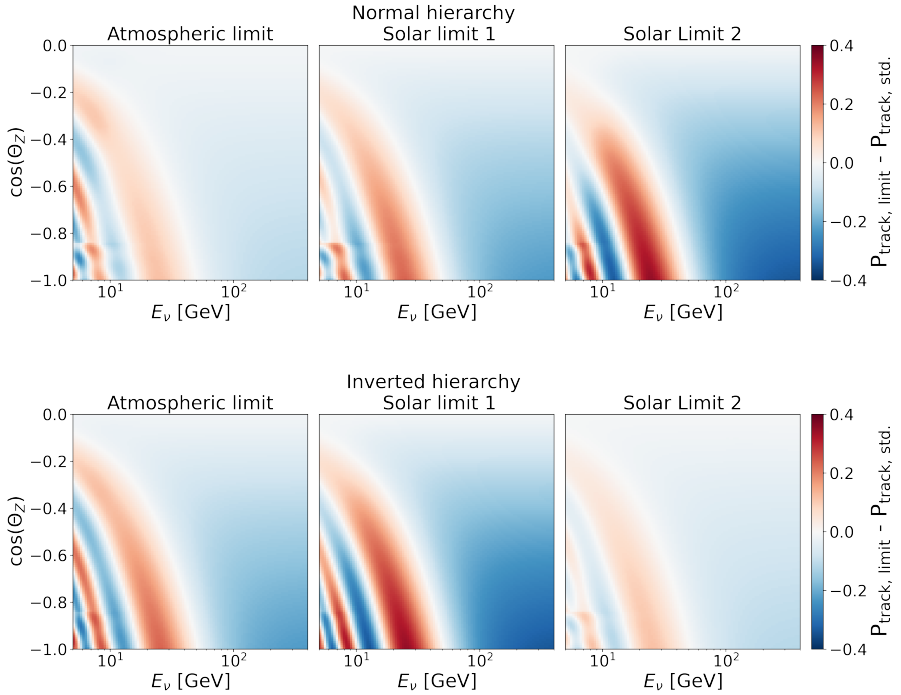

Figure 4.6: Difference between standard oscillations and the three limits in the approximated distribution of track-like events for $n = 0$.

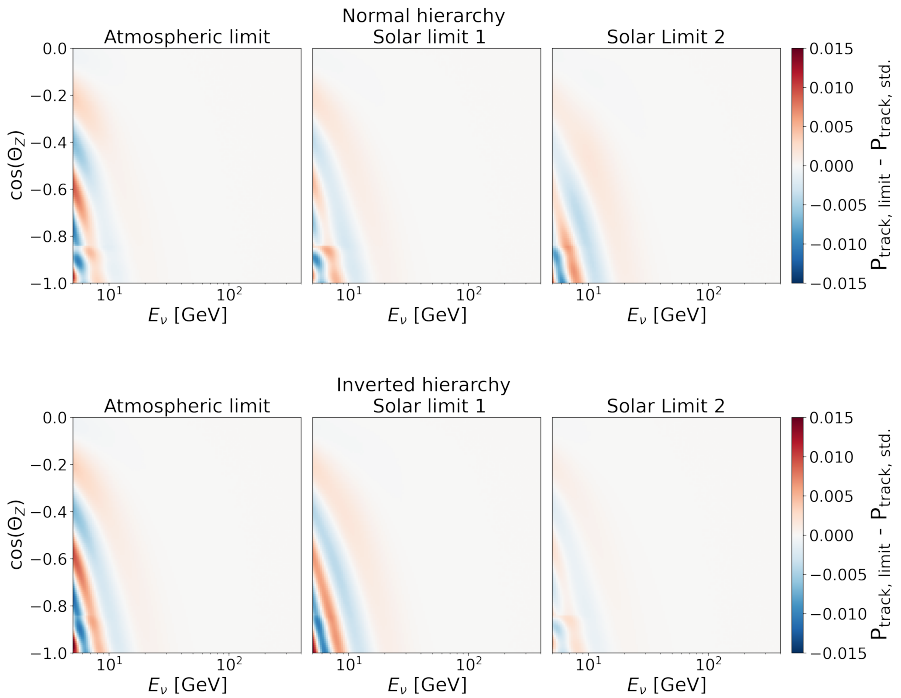

Figure 4.7: Difference between standard oscillations and the three limits in the approximated distribution of track-like events for $n = -2$.

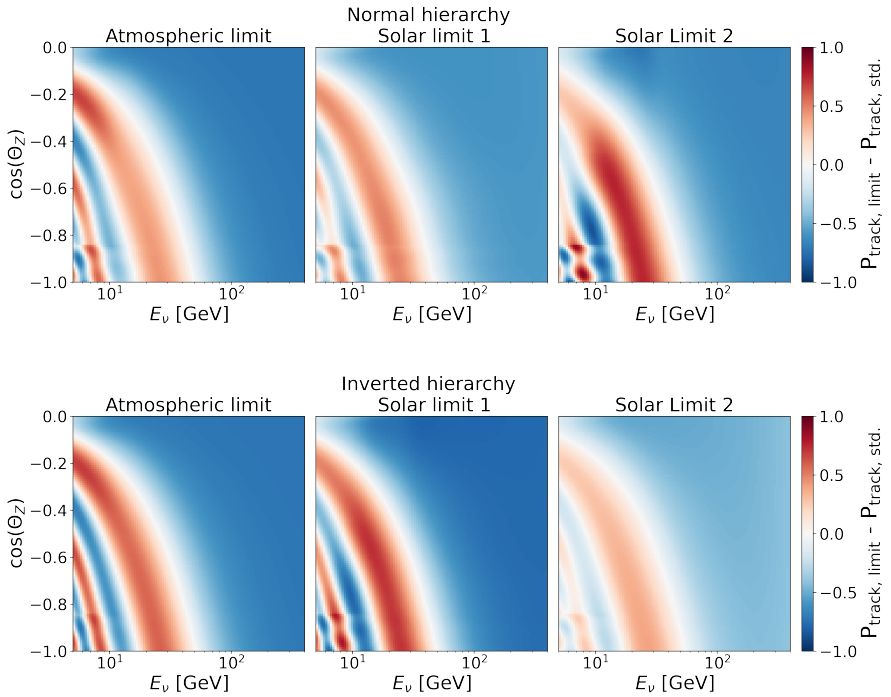

Figure 4.8: Difference between standard oscillations and the three limits in the approximated distribution of track-like events for $n = 2$.

5 Detector Sensitivities

In this work, the detector configurations of ORCA and ARCA with 115 detection strings are considered. This corresponds to the full ORCA detector and to one building block for ARCA, which will consist of two building blocks in total. Additionally, the sensitivity of ORCA with 6 strings is investigated, since for this configuration data is already available at the time. The data taking time is set to 3 years for ORCA115, 1 year for ARCA115 and 600 days for ORCA6, respectively. The intention here is to compare the sensitivity of ORCA115 to the results reported with three years of DeepCore data, and to compare ARCA115 with the result obtained with one year of IceCube data. The values for DeepCore and IceCube were taken from [15]. For ORCA6, the data taking time corresponds to a rough estimate of the full dataset since no official number is available at the time.

For all sensitivities reported in this work, the bounds on the decoherence parameter are determined at the 95% CL in order to be consistent with previous studies and publications.

In a first simple approach, no systematic uncertainties are included in the analysis. The sensitivity is then directly given by

$$S = \sqrt{|\Delta\chi^2_{\text{stat}}|} \tag{5.1}$$

with $\Delta\chi^2_{\text{stat}}$ is taken to be as defined in Equation 3.6.

Figure 5.1 shows the bounds γ_{lim} on the decoherence parameter obtained with this approach for all energy dependencies for the Atmospheric limit. The behaviour of the detector sensitivities for the Solar limits is analogous (see Appendix A).
It becomes apparent that the sensitivity of ORCA has the same dependence of n as the bounds obtained with DeepCore, and both detectors have the best sensitivity for $\gamma \propto E^{-1}$ and $\gamma \propto E^{-2}$. This is not surprising as ORCA and DeepCore, are designed to target low energy neutrinos of a few GeV, which contribute most to the divergence from the standard oscillation case for $\gamma \propto E^{-1}$ and $\gamma \propto E^{-2}$ (see Figure 4.7).
ORCA115 and even ORCA6 might be able to lower the bounds on the decoherence parameter for these two power dependencies. To further specify the potential of the detectors, systematic parameters are included in the analysis, as will be discussed in section 5.2.
The sensitivity of ARCA is comparable to the bounds obtained with IceCube. ARCA has the best performance in the cases $\gamma \propto E^1$ and $\gamma \propto E^2$, since it targets neutrinos of high energies. Consequently, these two power dependencies are studied in more detail for ARCA in the next section.

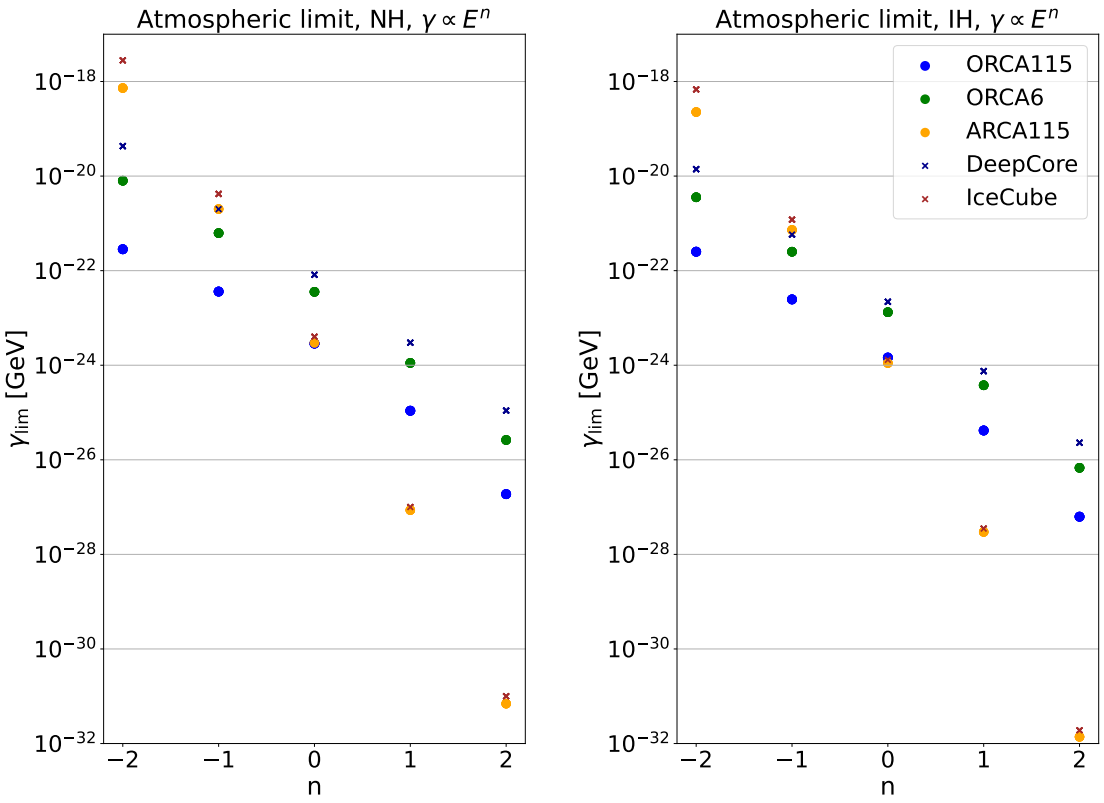

Figure 5.1: Sensitivities to decoherence at the 95 % CL for ORCA115, ORCA6 and ARCA115 in dependence of the power-law index n for normal (left) and inverted hierarchy (right) obtained with a simple approach with no systematic parameters. The limits from IceCube and DeepCore reported in [15] are shown for comparison.

5.1 ARCA

The specifications for the analysis for ARCA115 are summarized in Table 5.1, where the PID classes refer to the classes with best cut values. The determination of the best cut values is explained in the next section. Afterwards, the sensitivities obtained with the best cuts are presented. The sensitivities reported for ARCA are given by Equation 5.1, as no systematics were included in the analysis.

	ARCA115
Data taking time	1 year
PID classes	Showers: $p_{\text{track}} \leq 0.3$ Middles: $0.3 < p_{\text{track}} \leq 0.95$ Tracks: $p_{\text{track}} > 0.95$
Additional cuts	$p_{\text{bkg},\mu}$ <0.05
MC sample	ARCA_v6_2020
Energy reconstruction algorithm	Showers/Middles: Aashower Tracks: JGandalf

Table 5.1: Specifications for the analysis for ARCA115.

5.1.1 Optimization of PID cuts

Recall that the particle identification (PID) classes are defined by cuts on the scores $p_{\text{bkg,noise}}$, $p_{\text{bkg},\mu}$ and p_{track}. For ARCA, the impact of the cut on p_{track} on the sensitivity is investigated for $\gamma \propto E^1$ and $\gamma \propto E^2$. The results for normal and inverted hierarchy can be seen in Figure 5.2 and Figure 5.3, respectively, where the bounds on the decoherence parameter are shown in dependence of the cut value for all three limits[4].
In a first approach, a standard two-class strategy is pursued: For $p_{\text{track}} \leq p_{\text{cut}}$, events are classified as showers. For $p_{\text{track}} > p_{\text{cut}}$, events are classified as tracks. The bounds obtained with this strategy are indicated by the dots in Figure 5.2 and Figure 5.3.
The sensitivity can be further improved by introducing a *middles* class. In this case, showers are defined by $p_{\text{track}} \leq 0.3$, the middles class contains events with $0.3 < p_{\text{track}} \leq p_{\text{cut}}$, and the tracks class consist of events with $p_{\text{track}} > p_{\text{cut}}$. The bounds obtained with the additional *middles* class are indicated by the crosses.
As can be seen in both figures, the best cut value is $p_{\text{cut}} = 0.95$ for most cases. The only exceptions here are Solar limit 2, $\gamma \propto E^2$ for normal hierarchy and Solar limit 1, $\gamma \propto E^2$ for inverted hierarchy. In these two cases, an even stricter cut of $p_{\text{cut}} = 0.99$ resulted in a slightly better sensitivity.
The improvement in sensitivity when applying strict cuts can be attributed to a higher purity of the tracks class. However, it is expected that even more stringent cuts should lower the sensitivity, due to the reduction in statistics for the tracks class.
Figure 5.4 shows the statistical Chi-square in dependence of the decoherence parameter for the best cut value $p_{\text{cut}} = 0.95$. The solid lines correspond to the interpolation between the calculated $\sqrt{\Delta\chi^2_{\text{stat}}}$ values. The contributions from each individual PID class is shown as dotted/dashed line in the respective color for each limit. Here it becomes apparent that the tracks class contributes most to the sensitivity, while the contribution from showers and middles class is about ten orders of magnitude smaller. This is because shower-like events are not detected very efficiently with ARCA due to the large separation between the detection strings.

[4]The assumed data taking time is 3 years here. This does not affect the dependence of the bound on the PID cuts.

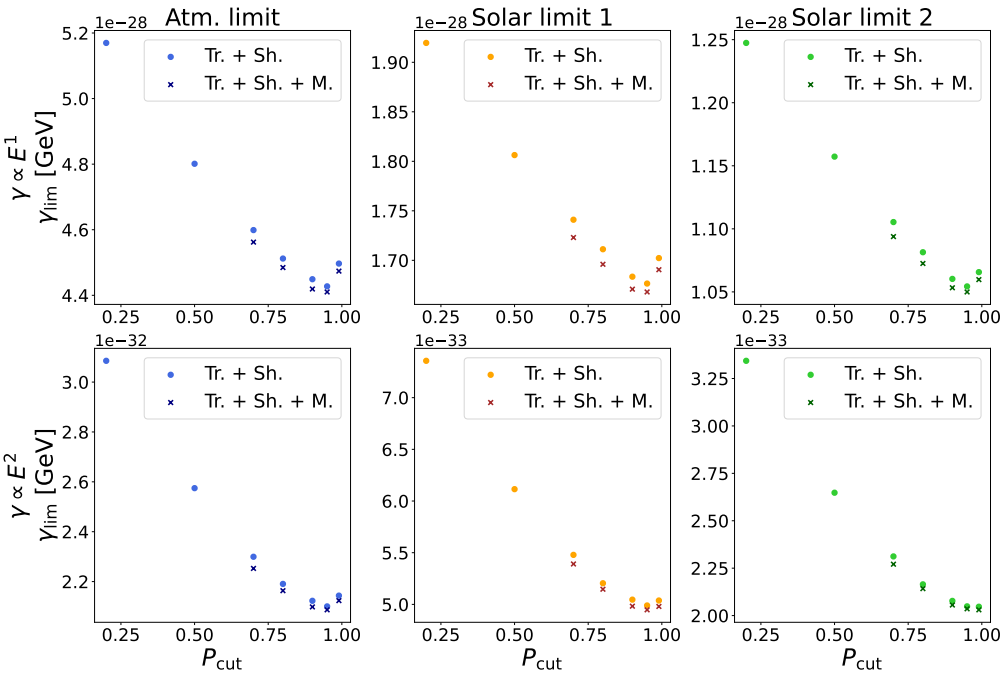

Figure 5.2: Sensitivities for different cuts on the tracks class for ARCA115 assuming normal hierarchy. The abbreviations in the legend refer to Tracks, Showers and Middles.

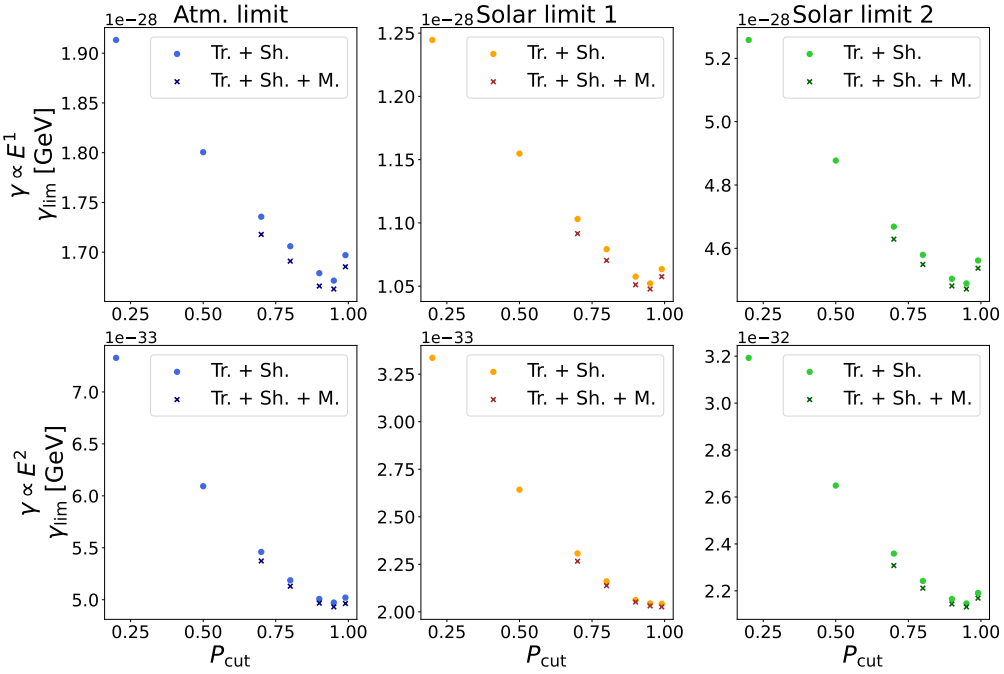

Figure 5.3: Sensitivities for different cuts on the tracks class for ARCA115 assuming inverted hierarchy.

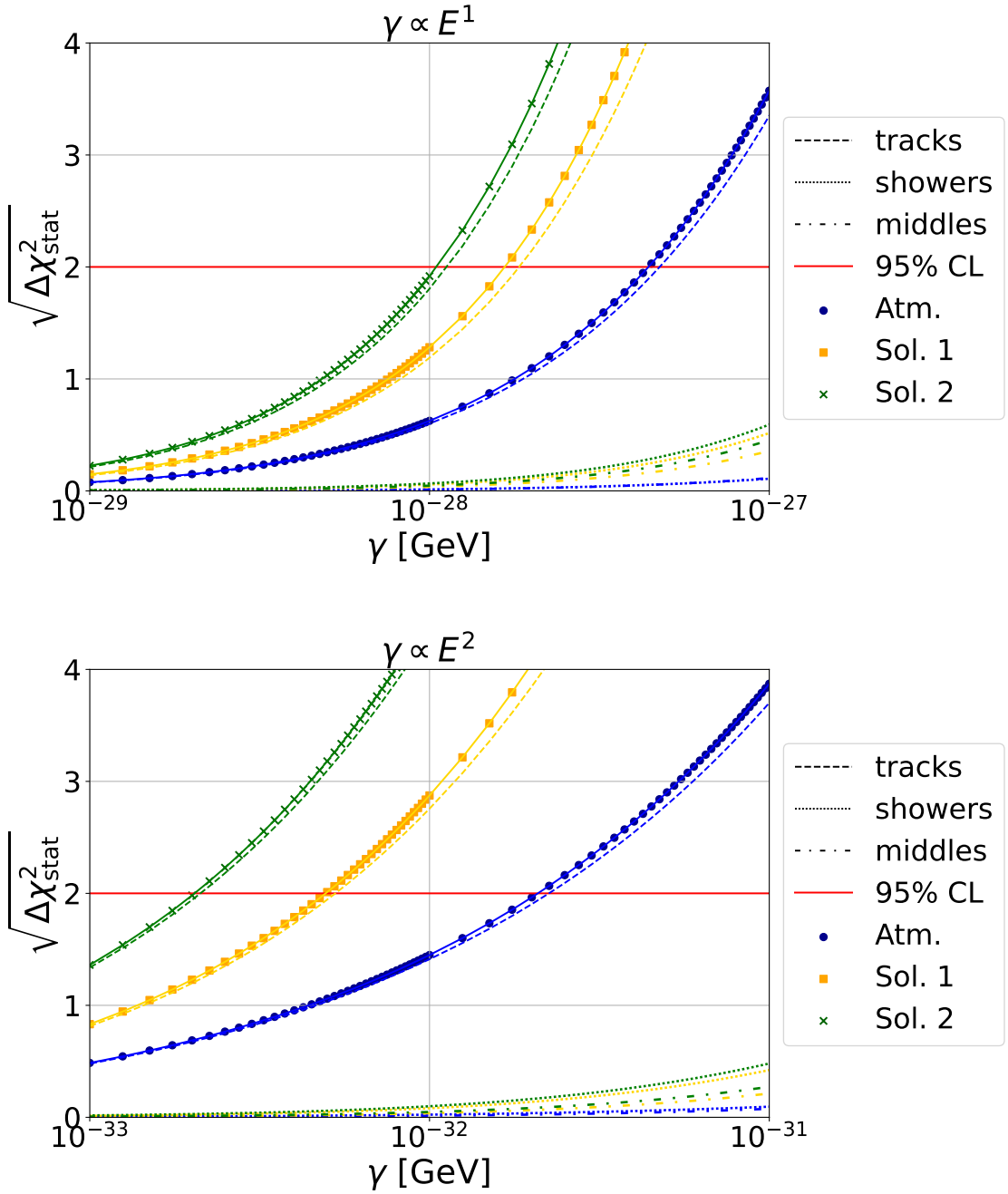

Figure 5.4: Statistical Chi-square as a function of the decoherence parameter for the Atmospheric limit (blue), Solar Limit 1 (orange) and Solar Limit 2 (green) for normal hierarchy. The contributions from the individual PID classes are shown as dotted and dashed lines in the respective colors.

5.1.2 Sensitivity with ARCA115

Figure 5.5 compares the sensitivity obtained with the best cuts for ARCA115 to the results obtained for one year of data from IceCube. The values are listed in Table 5.2. Note that for IceCube a set of systematic parameters was fitted, which was not done in the analysis for ARCA. This might explain why ARCA115 has a better performance than IceCube in this comparison, even though the instrumented volume of ARCA115 is only about half as big.

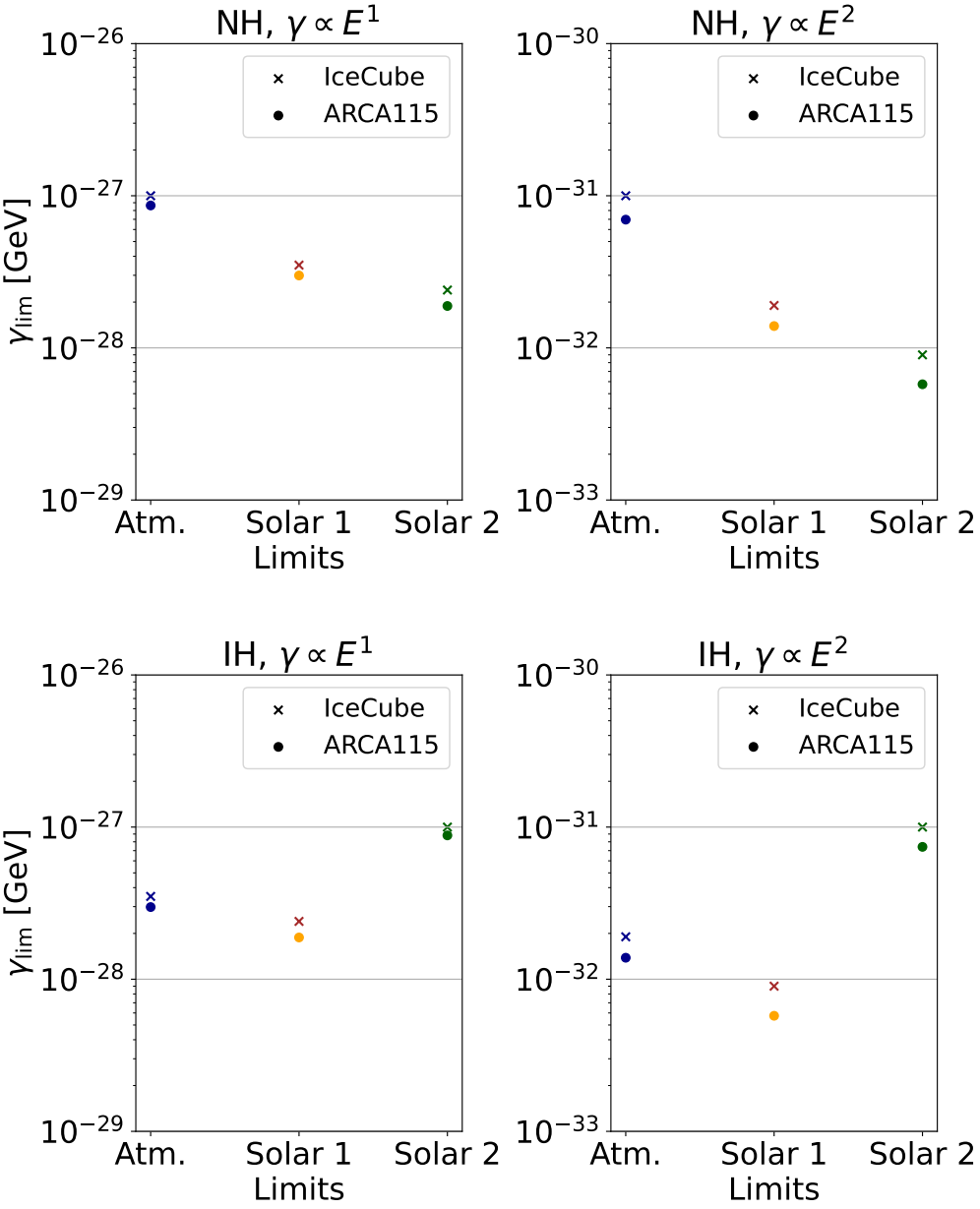

Figure 5.5: Sensitivity to decoherence for one year of data taking time with ARCA115 in comparison with the bounds obtained with IceCube.

The behaviour of the sensitivities for the different limits is as expected:
First of all, the equivalences stated in Equation 4.1 for the oscillation probabilities can be seen in the sensitivities in Figure 5.5 (compare e.g. the Atmospheric limit NH to the Solar limit 2 IH). Furthermore, the sensitivity is best for the Solar limit 2 (Solar Limit 1) for normal (inverted) hierarchy. These are the limits for which the divergence from standard oscillations is largest, as we saw in Figure 4.8.

		$n = 1$	$n = 2$
NH	Atmospheric limit	$8.6 \cdot 10^{-28}$	$7.0 \cdot 10^{-32}$
	Solar limit 1	$3.0 \cdot 10^{-28}$	$1.4 \cdot 10^{-32}$
	Solar limit 2	$1.9 \cdot 10^{-28}$	$5.8 \cdot 10^{-33}$
IH	Atmospheric limit	$3.0 \cdot 10^{-28}$	$1.4 \cdot 10^{-32}$
	Solar limit 1	$1.8 \cdot 10^{-28}$	$5.7 \cdot 10^{-33}$
	Solar limit 2	$8.8 \cdot 10^{-28}$	$7.4 \cdot 10^{-32}$

Table 5.2: Bounds on the decoherence parameter γ_{ij} in GeV for one year of data taking time with ARCA115.

5.2 ORCA

The details for the analysis for ORCA115 and ORCA6 are listed in Table 5.3. The PID classes listed here again refer to the classes with best cuts, which are determined in the same way as for ARCA.

	ORCA115	ORCA6
Data taking time	3 years	600 days
PID classes	Showers: $p_{\text{track}} \leq 0.3$ Middles: $0.3 < p_{\text{track}} \leq 0.9$ Tracks: $p_{\text{track}} > 0.9$	Showers: $p_{\text{track}} \leq 0.3$ Middles: $0.3 < p_{\text{track}} \leq 0.8$ Tracks: $p_{\text{track}} > 0.8$
Additional cuts	$p_{\text{bkg},\mu} < 0.05$ $p_{\text{bkg,noise}} < 0.1$ gandalf_loose_is_selected is_good_recoJGandalf	$p_{\text{bkg},\mu} < 0.05$
MC sample	ORCA115_20x9_MX_PID_20190222	ORCA6_v6_2021
Energy reconstruction algorithm	Showers/Middles: Dusj Tracks: JGandalf	Showers/Middles: JShower Tracks: JGandalf

Table 5.3: Specifications for the analysis for ORCA115 and ORCA6.

5.2.1 Optimization of PID cuts

Figure 5.6 to Figure 5.9 show the sensitivities for different values of p_{cut} for ORCA115 and ORCA6 for normal and inverted hierarchy. The optimal cuts for ORCA115 are in an area between $p_{\text{cut}} = 0.8$ and $p_{\text{cut}} = 0.95$ for all limits and powers. For ORCA6, the best cut value is $p_{\text{cut}} = 0.8$, except for the Atmospheric limit assuming inverted hierarchy, where $p_{\text{cut}} = 0.7$ resulted in a better sensitivity.
It can be seen that, just as for ARCA, introducing a middles class improves the sensitivity compared to the two-classes approach. When introducing a middles class, the contribution from the shower class is reduced a little bit due to the loss of statistics. However, the impact is very small because it is compensated by a higher purity of the shower class. The additional contribution from the middles class is about as big as for the shower class, as can be seen in Figure 5.10 and Figure 5.11, where the contribution of the individual PID classes to the sensitivity is shown. This additional contribution from the middles class leads to a higher sensitivity compared to the two-class approach. Compared to ARCA, the relative contribution of the showers and middles class is bigger. Due to the smaller spacing between the detection strings, ORCA can detect shower-like events with higher efficiency. Nevertheless, also for ORCA tracks are the most important PID class in the sensitivity to decoherence. The PID classes in Table 5.3 are chosen for the further analysis for ORCA.

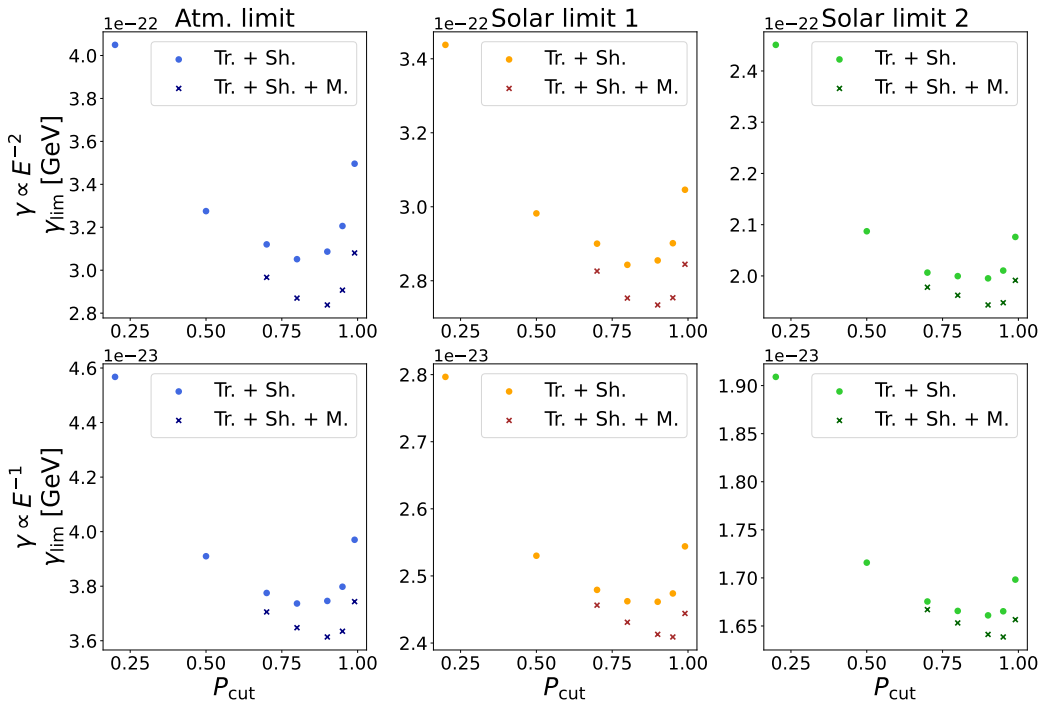

Figure 5.6: Sensitivities for different cuts on the tracks class for ORCA115 assuming normal hierarchy.

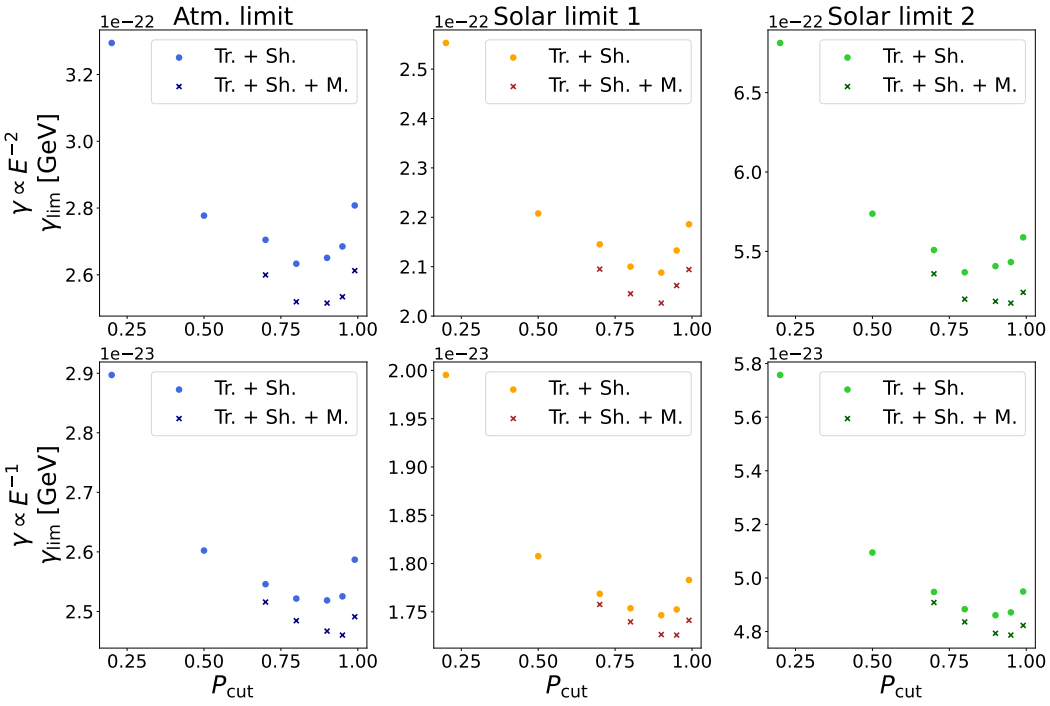

Figure 5.7: Sensitivities for different cuts on the tracks class for ORCA115 assuming inverted hierarchy.

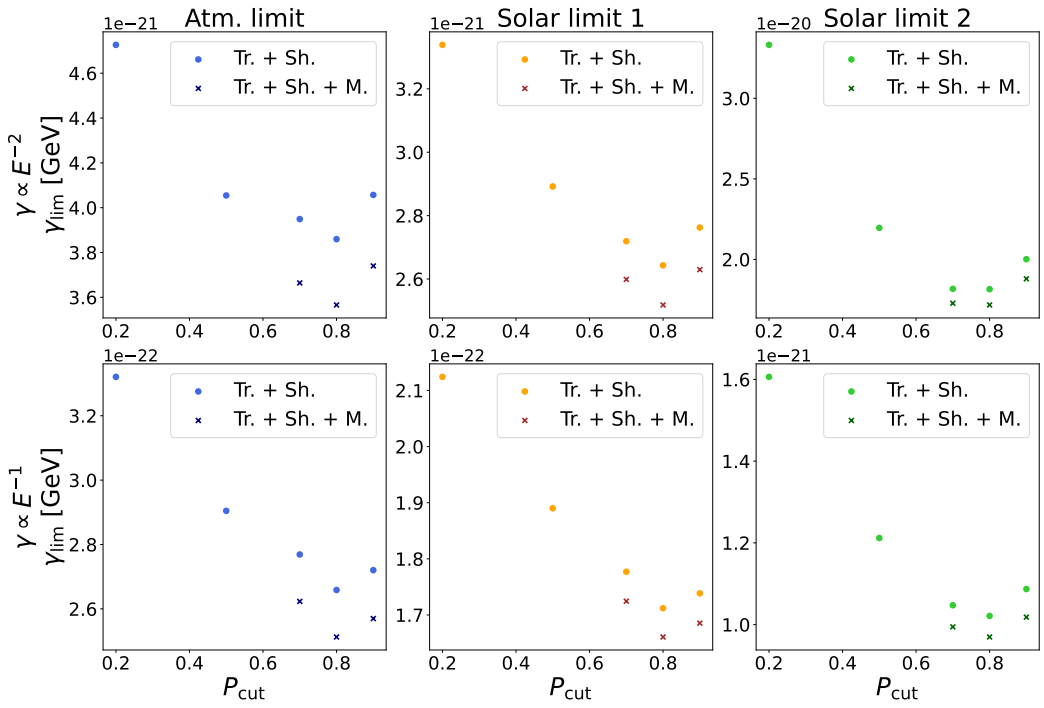

Figure 5.8: Sensitivities for different cuts on the tracks class for ORCA6 assuming normal hierarchy.

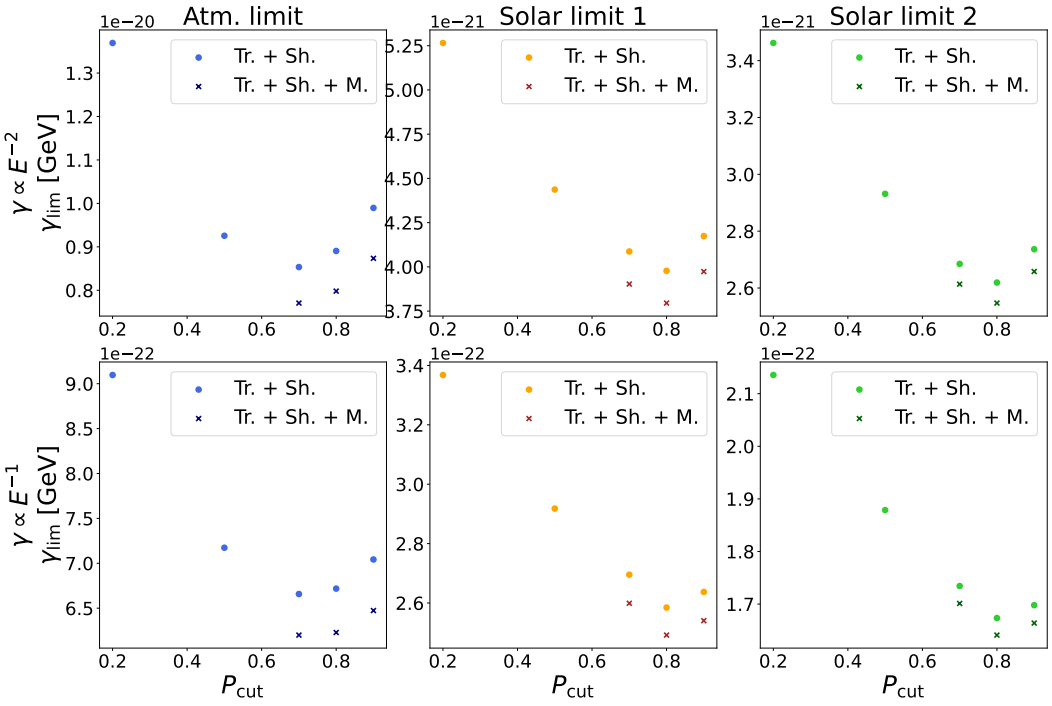

Figure 5.9: Sensitivities for different cuts on the tracks class for ORCA6 assuming inverted hierarchy.

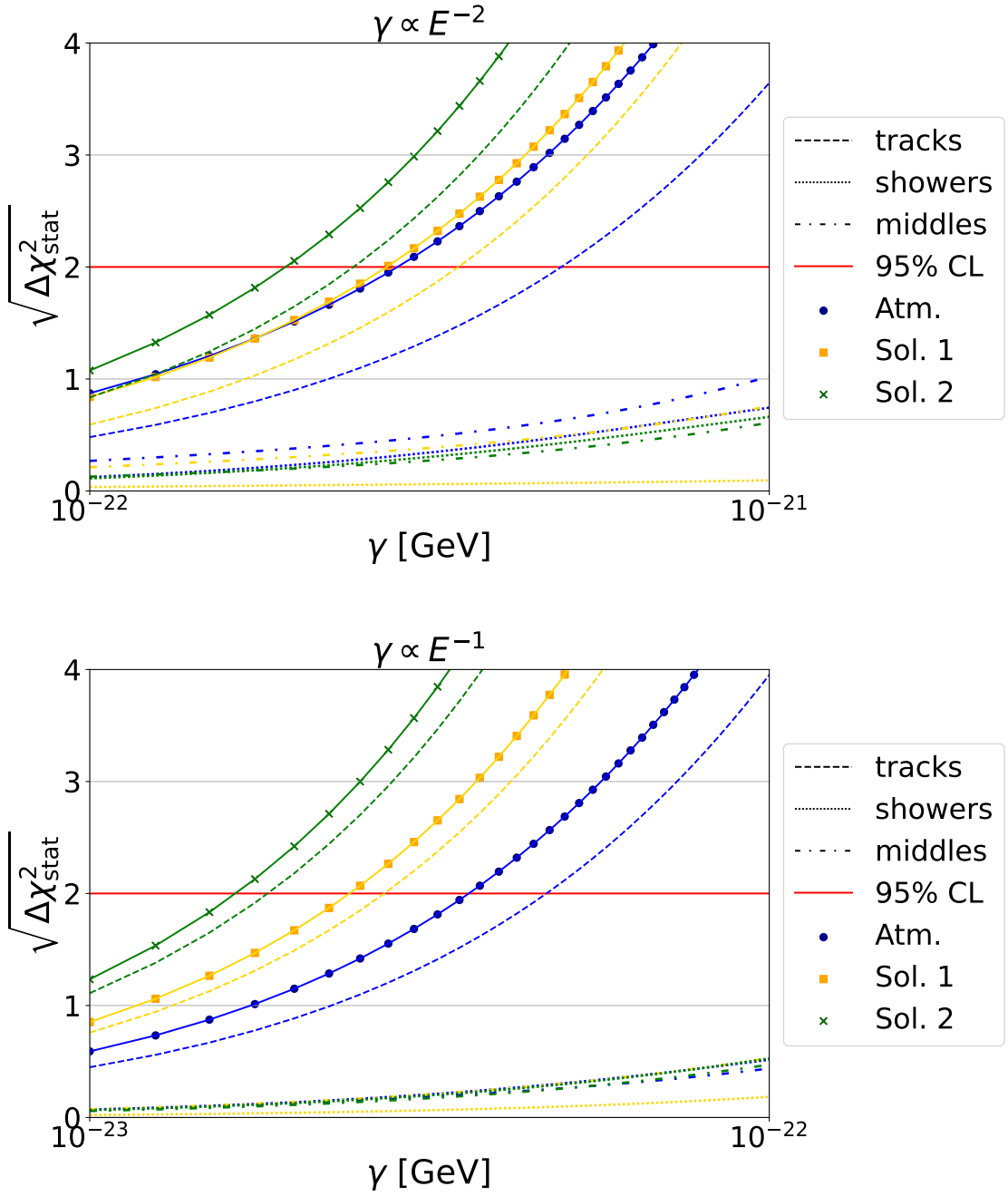

Figure 5.10: Statistical Chi-square for ORCA115 as a function of the decoherence parameter for the Atmospheric limit (blue), Solar Limit 1 (orange) and Solar Limit 2 (green) for normal hierarchy.

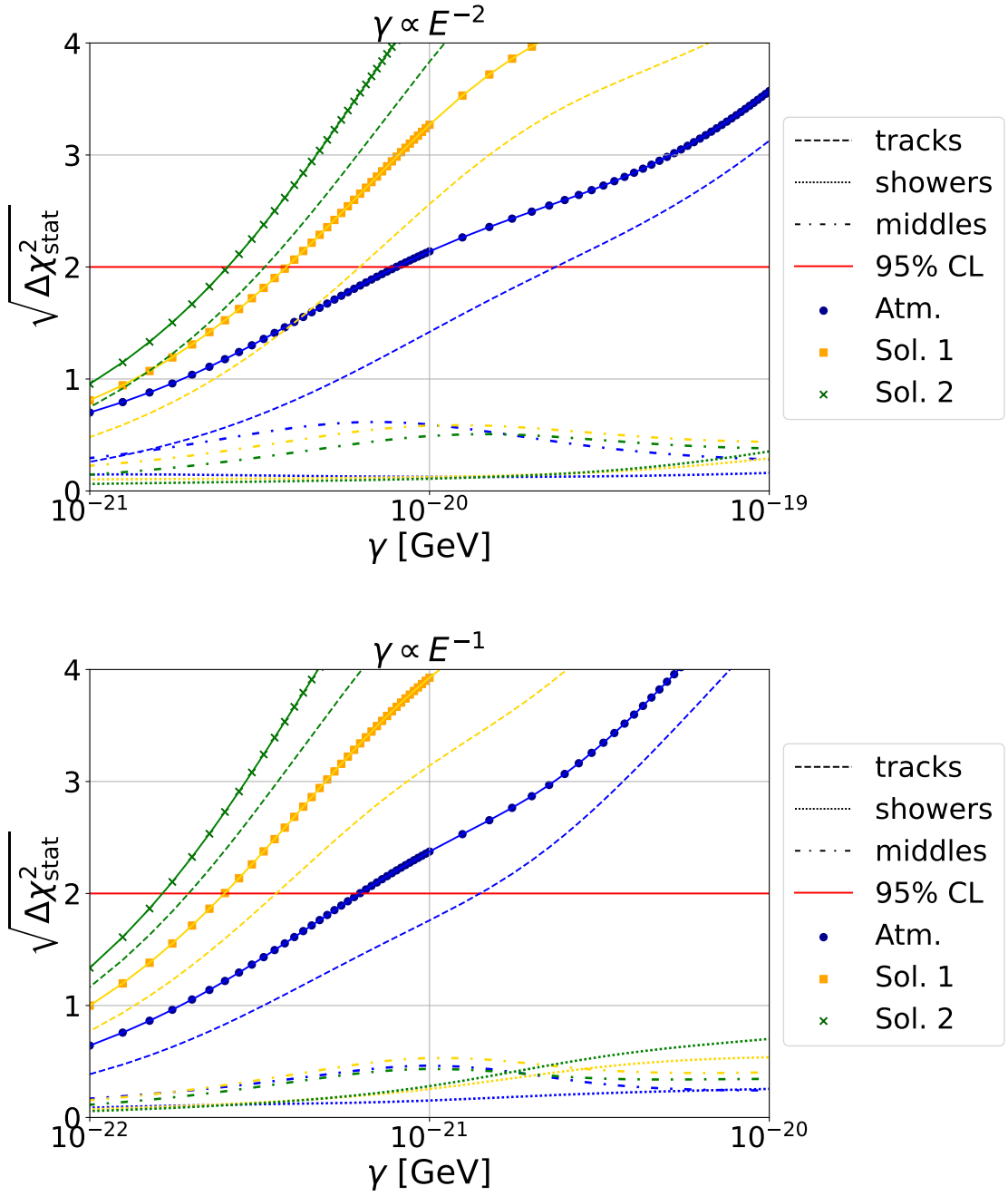

Figure 5.11: Statistical Chi-square for ORCA6 as a function of the decoherence parameter for the Atmospheric limit (blue), Solar Limit 1 (orange) and Solar Limit 2 (green) for normal hierarchy.

5.2.2 Sensitivities with ORCA115 and ORCA6

To make the sensitivity calculations more realistic, the oscillation parameters and a set of systematic parameters are fitted in the determination of the Chi-square. Table 5.4 and Table 5.5 show the fitted parameters along with their corresponding (starting) values as well as their treatment in the minimization. Each parameter is either fixed to a certain value, left completely free in the fit, or constrained by a prior.
As explained in Sec. 3.2, the parameters constrained by a prior are assumed to follow a Gaussian distribution. The mean m of the distribution is given by theoretical calculations and/or global best fit values. The value given by the prior corresponds to the the standard deviation σ of the Gaussian distribution. It is determined based on the uncertainty of each parameter. For each parameter with a prior, a penalty term of the form $^{(x-m)^2}/_{\sigma^2}$ is added to the statistical Chi-square, where x is the value determined by the fit. The penalty term is bigger, the bigger the discrepancy between the fit value x and the mean m is, and the smaller the standard deviation σ is.
Some of the parameters, as those describing the flavor composition, depend on the neutrino energy. In this case, the deviation from the expected value is returned by SWIM.
The parentheses in Table 5.4 indicate the cases where a different value was taken for inverted hierarchy. The parameters as well as their individual impact on the sensitivity is discussed in detail in the next chapters.

Until now, the oscillation parameters were fixed to the values from [9], where no decoherence is assumed. This means that potential decoherence effects in other experiments could have affected these values. This is relevant for ORCA, since the detector is sensitive to some of the oscillation parameters. By having a prior on Θ_{13} we assume that the experiments that determine this parameter are not sensitive to decoherence in the same way as ORCA. Note that for ARCA the oscillation parameters should have no impact on the sensitivity.

Parameter	Central value (IH)	Prior
$\Delta m^2_{\text{atm}}\,[\text{eV}^2]$	$2.515 \cdot 10^{-3}$ $(-2.498 \cdot 10^{-3})$	free
$\Delta m^2_{\text{sol}}\,[\text{eV}^2]$	$7.42 \cdot 10^{-5}$	fixed
$\Theta_{12}\,[°]$	33.44	fixed
$\Theta_{13}\,[°]$	8.57	0.13
$\Theta_{23}\,[°]$	49.2	free
$\delta_{\text{CP}}\,[°]$	149 (287)	free

Table 5.4: Oscillation parameters.

Figure 5.12 and Figure 5.13 show the total Chi-square with all parameters fitted for both detectors and both mass hierarchies, as well as the 95 % CL. The solid lines again correspond to a linear interpolation between the points. Note that for ORCA115, NH, $\gamma \propto E^{-1}$ the fit failed for two values of γ. The additional dashed lines in this plot indicate the case where only oscillation parameters were fitted. The two points where the fit failed lie even above these limits, which indicates that the fit was not able to find the minimum. Therefore, these two points were excluded in the determination of the sensitivity.

The sensitivities can be seen in Figure 5.14, where the current bounds from DeepCore are shown for comparison. The values obtained with all parameters fixed are also shown, in order to see the impact of fitting systematics. The results are additionally summarized in Table 5.6 and Table 5.7.
Even with all systematics fitted, ORCA6 has a better sensitivity than DeepCore for all cases. This means that the bounds on the decoherence parameter could potentially be lowered with the dataset that will soon be available for ORCA6.
The sensitivity of ORCA115 is more than one order of magnitude better than the bounds from DeepCore. With ORCA115 it will be possible to lower the bounds on the decoherence parameter considerably for certain power dependencies.

Parameter	Prior
Energy slope	0.3
Energy scale	0.06
Zenith angle slope	0.02
$\nu_e/\bar{\nu}_e$	0.07
$\nu_\mu/\bar{\nu}_\mu$	0.05
$(\nu_\mu+\bar{\nu}_\mu)/(\nu_e+\bar{\nu}_e)$	0.02
n_{showers}	free
n_{middles}	free
n_{tracks}	free

Table 5.5: Systematic parameters.

	ORCA115	$n=-2$	$n=-1$
NH	Atmospheric limit	$3.2 \cdot 10^{-22}$	$4.5 \cdot 10^{-23}$
	Solar limit 1	$3.5 \cdot 10^{-22}$	$3.5 \cdot 10^{-23}$
	Solar limit 2	$2.3 \cdot 10^{-22}$	$2.3 \cdot 10^{-23}$
IH	Atmospheric limit	$2.9 \cdot 10^{-22}$	$3.5 \cdot 10^{-23}$
	Solar limit 1	$2.6 \cdot 10^{-22}$	$2.6 \cdot 10^{-23}$
	Solar limit 2	$6.8 \cdot 10^{-22}$	$7.5 \cdot 10^{-23}$

Table 5.6: Bounds on the decoherence parameter γ_{ij} in GeV with three years of data taking time with ORCA115.

	ORCA6	$n=-2$	$n=-1$
NH	Atmospheric limit	$1.6 \cdot 10^{-20}$	$9.0 \cdot 10^{-22}$
	Solar limit 1	$5.2 \cdot 10^{-21}$	$3.1 \cdot 10^{-22}$
	Solar limit 2	$3.2 \cdot 10^{-21}$	$1.9 \cdot 10^{-22}$
IH	Atmospheric limit	$5.1 \cdot 10^{-21}$	$3.2 \cdot 10^{-22}$
	Solar limit 1	$3.4 \cdot 10^{-21}$	$2.0 \cdot 10^{-22}$
	Solar limit 2	$2.9 \cdot 10^{-20}$	$1.4 \cdot 10^{-21}$

Table 5.7: Bounds on the decoherence parameter γ_{ij} in GeV with 600 days of data taking time with ORCA6.

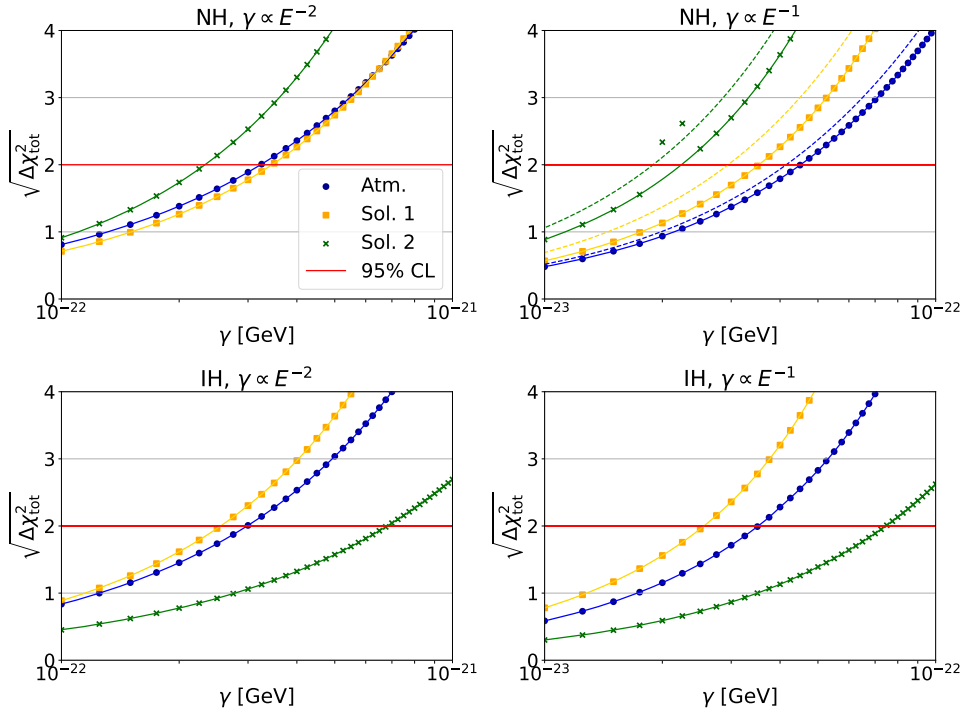

Figure 5.12: Chi-square for ORCA115 with all parameters fitted.

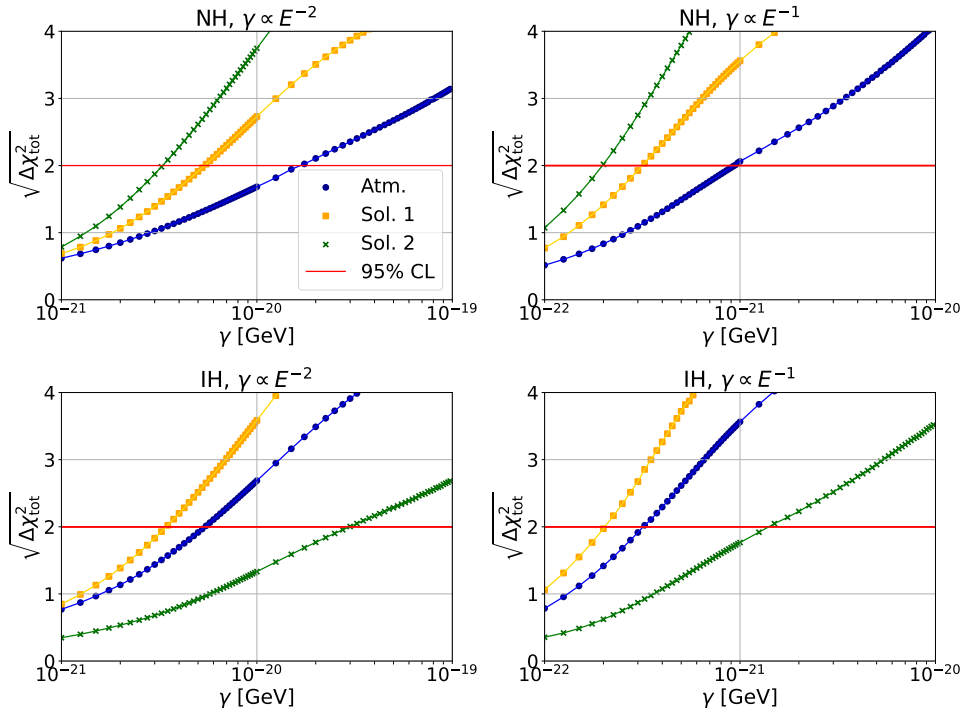

Figure 5.13: Chi-square for ORCA6 with all parameters fitted.

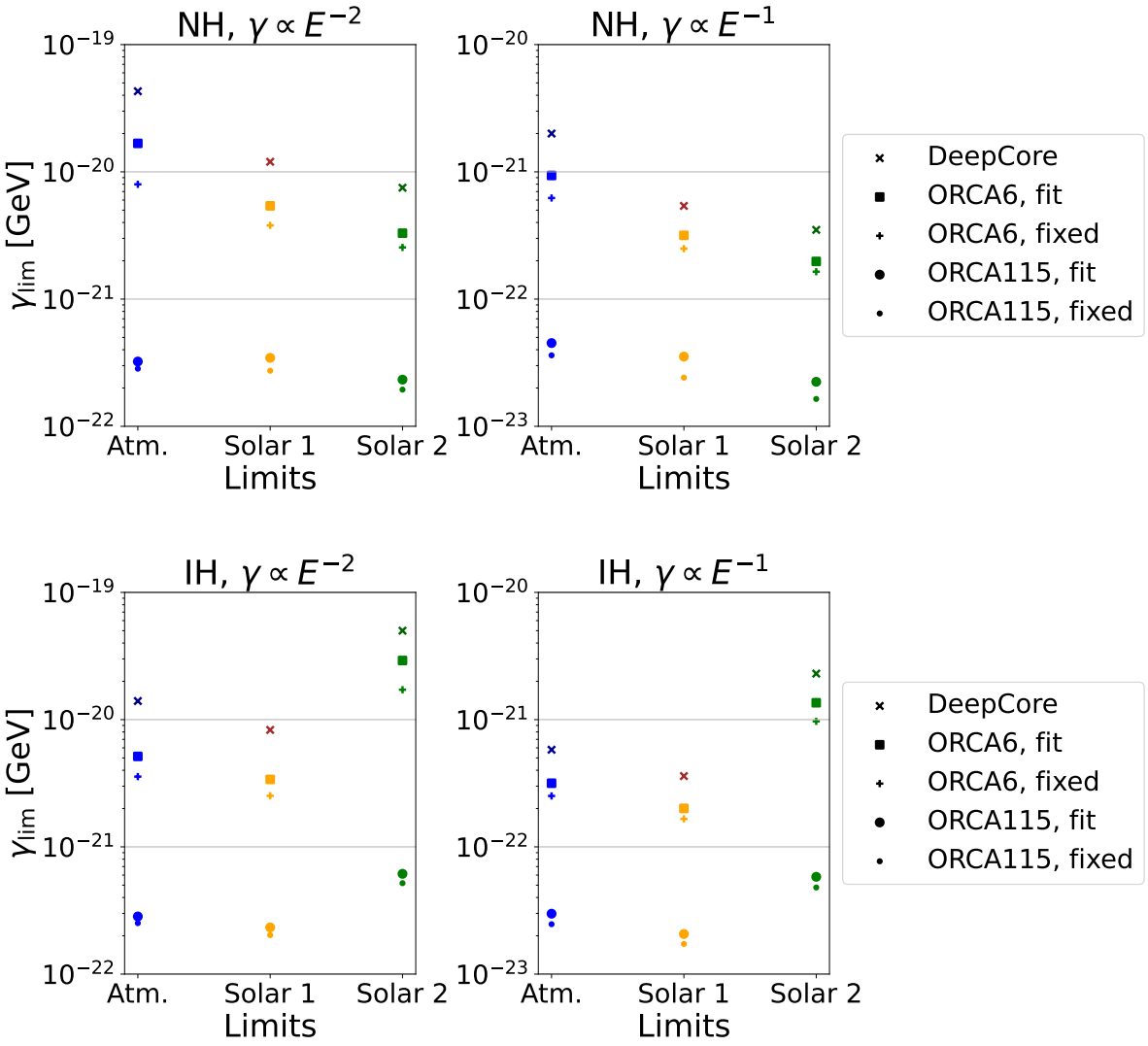

Figure 5.14: Sensitivity to decoherence for three years of data taking time with ORCA115 and 600 days of data taking time with ORCA6, compared to the bounds from DeepCore. Additionally, the results when all parameters were fixed are shown.

5.2.3 Impact of oscillation parameters

This section discusses how the individual oscillation parameters affect ORCA's sensitivity to decoherence. Figure 5.15 and Figure 5.16 show the normalized difference in sensitivity when only the parameter inscribed on the x-axis is fitted and the sensitivity when all parameters are fixed. The inscription *all* refers to the case when all parameters were fitted simultaneously. In general, the impact of fitting the parameters is bigger for ORCA6 than for ORCA115. However, the relative impact of the individual parameters is comparable for both detectors. It can be seen that of all parameters Θ_{23} has the biggest influence on the sensitivity for both, ORCA115 and ORCA6.

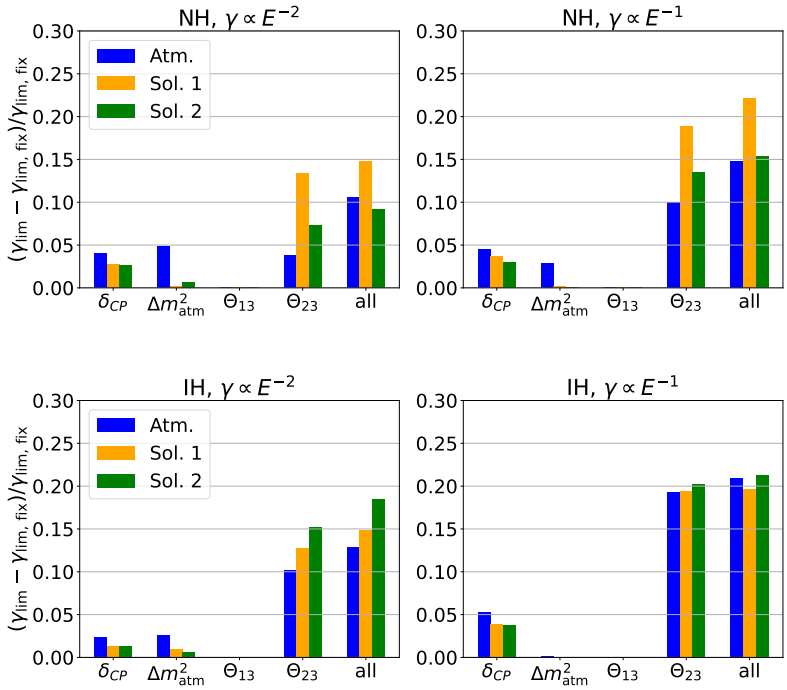

Figure 5.15: Normalized difference of the sensitivity for ORCA115 with the oscillation parameters fitted and all parameters fixed.

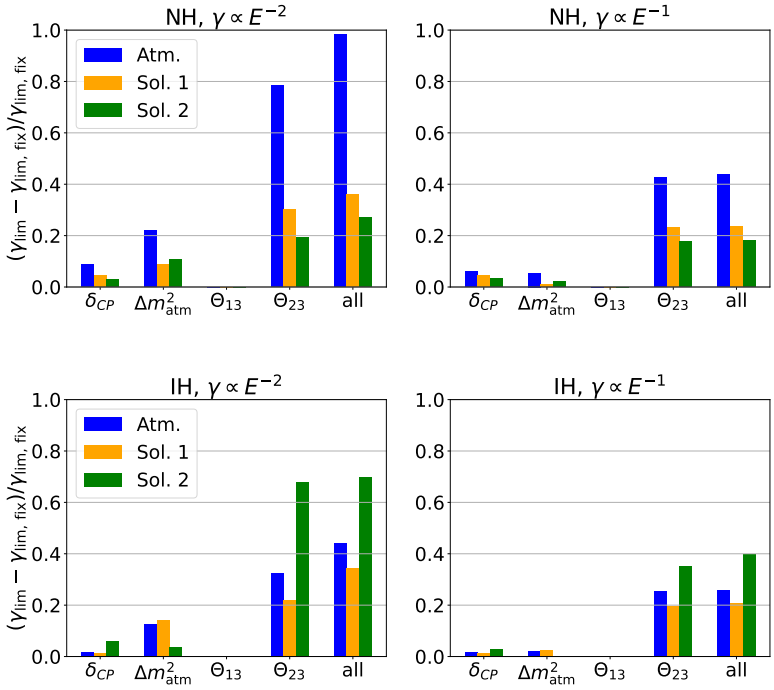

Figure 5.16: Normalized difference of the sensitivity for ORCA6 with the oscillation parameters fitted and all parameters fixed.

The behaviour of Θ_{23} in dependence of the decoherence parameters is shown in Figure 5.17 for normal hierarchy. The behaviour for inverted hierarchy is analogous (see Appendix A). For all limits the parameter tends to drive towards maximal mixing. The reason for this is that $\Theta_{23} \to 45\,^\circ$ enhances neutrino oscillations and counteracts the damping of decoherence effects. This leads to a reduced contrast in the histograms for the sensitivity calculation. For very strong decoherence effects Θ_{23} can reach unphysical values. Therefore, the current bounds from DeepCore are shown as vertical lines in Figure 5.17. It can be seen that the values of Θ_{23} are reasonable at least up to these bounds.

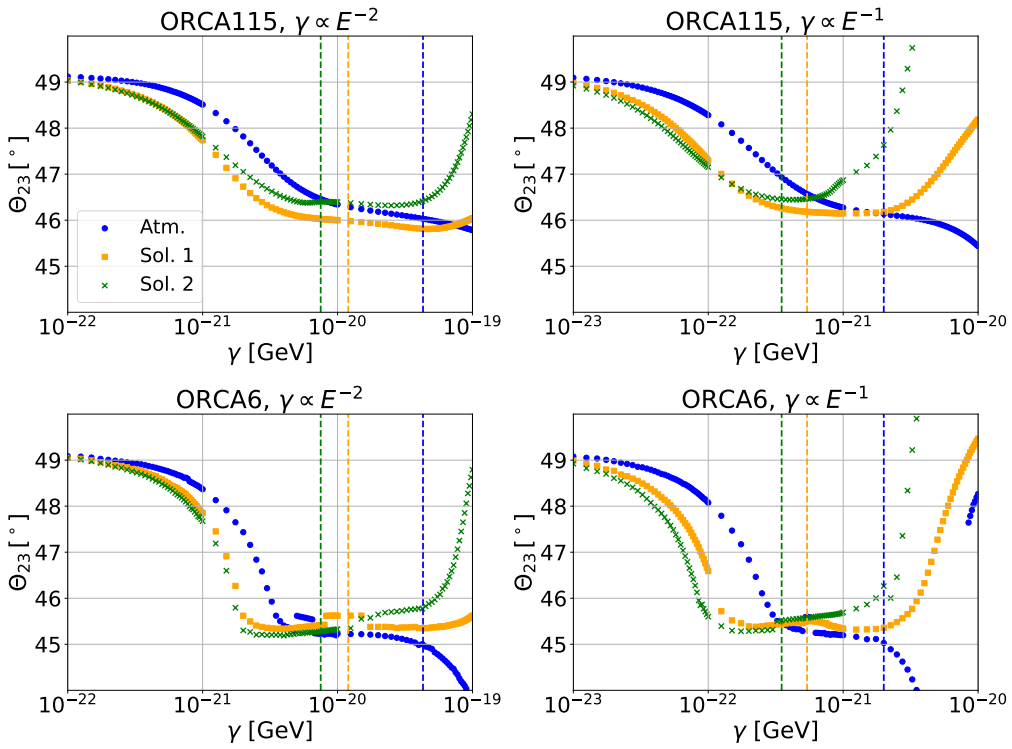

Figure 5.17: Behaviour of Θ_{23} in the minimization in dependence of the decoherence parameter for normal hierarchy. As the strength of decoherence effects increases, $\Theta_{23} \to 45\,^\circ$ counteracts the damping of neutrino oscillations.

Since Θ_{23} has a high impact on decoherence studies, the dependence of the sensitivity on the true value of this parameter was investigated. This can be seen in Figure 5.18. As expected, the minimum is around $\Theta_{23} = 45\,^\circ$, since for this true value oscillations are maximal and therefore a damping in the oscillations can be seen most clearly. The same behaviour is found for the Solar limits (see Appendix A). The reason that the minimum in the fit is not exactly at $\Theta_{23} = 45\,^\circ$ is due to the contribution of Θ_{13} to the oscillation amplitude.

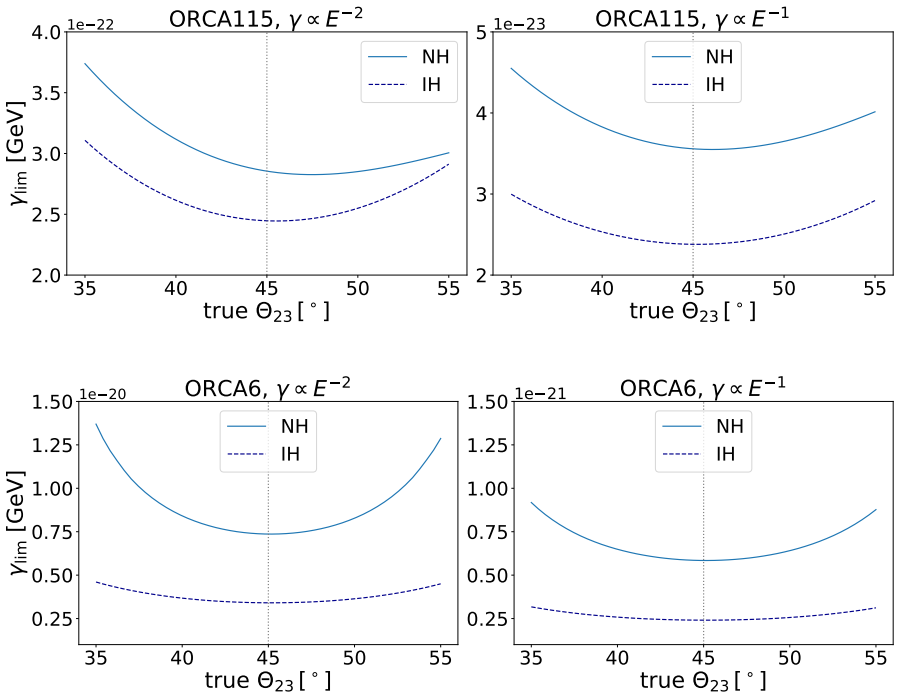

Figure 5.18: Dependence of the sensitivity on the true value of Θ_{23} for the Atmospheric limit. The sensitivity is best around maximal mixing.

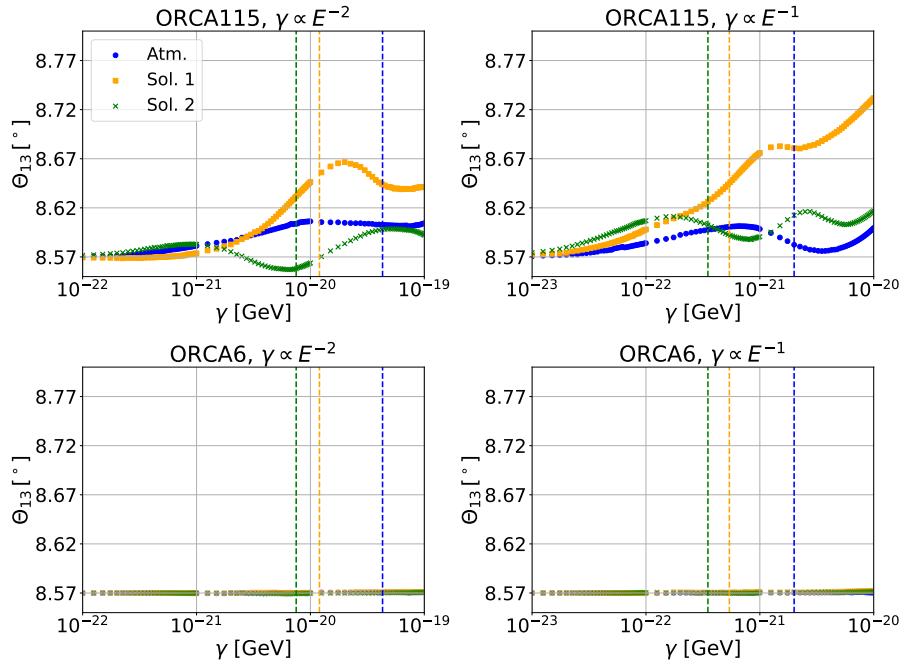

Figure 5.19: Behaviour of Θ_{13} in the minimization in dependence of the decoherence parameter for normal hierarchy. Θ_{13} was fitted with a prior of 0.13.

The behaviour of Θ_{13} in the fit is shown in Figure 5.19. The parameter stays within the bounds provided by the prior but shows a tendency towards higher values for ORCA115. For ORCA6 Θ_{13} is almost constant which indicates that ORCA6 is not sensitive to this parameter.

The influence of δ_{CP} on the sensitivity is relatively small. Nevertheless, the fit values for this parameter are shown in Figure 5.22 for normal hierarchy and in Figure 5.23 for inverted hierarchy. Since the CP-violating phase is not very well constrained at the time, the sensitivity was calculated for three extreme cases: $\delta_{\mathrm{CP}} = 0$ and $\delta_{\mathrm{CP}} = 180\,°$, which corresponds to no CP-violation and $\delta_{\mathrm{CP}} = 90\,°$, which corresponds to maximal CP-violation. All other parameters were kept fixed. The ratio of the sensitivity for each of these cases and the case where δ_{CP} was set to the NuFit value is shown in Figure 5.21 and **??** for normal and inverted hierarchy. This plot confirms that δ_{CP} can have an impact on the sensitivity of a few percent. The impact is larger for inverted hierarchy for all limits, which might also explain the larger fluctuation of δ_{CP} in the fit for inverted hierarchy. For most cases the sensitivity is better for the cases with no CP-violation.

Finally, the fit values for $\Delta m^2_{\mathrm{atm}}$ can be seen in Figure 5.24. Since varying $\Delta m^2_{\mathrm{atm}}$ only changes the oscillation frequency, the impact of fitting this parameter is relatively small. For both detector configurations a similar behaviour of $\Delta m^2_{\mathrm{atm}}$ can be observed. Note that for inverted hierarchy, the behaviour is very much alike for each of the limits if the equivalences stated in Equation 4.1 are taken into account (see Appendix A).
The dependence of the sensitivities on the true value of $\Delta m^2_{\mathrm{atm}}$ is shown in Figure 5.25. For smaller values the sensitivity increases slightly. This indicated a larger deviation from the standard oscillations for higher frequencies, which possibly stems from a higher number of oscillation amplitudes that contribute to the deviation per energy range.

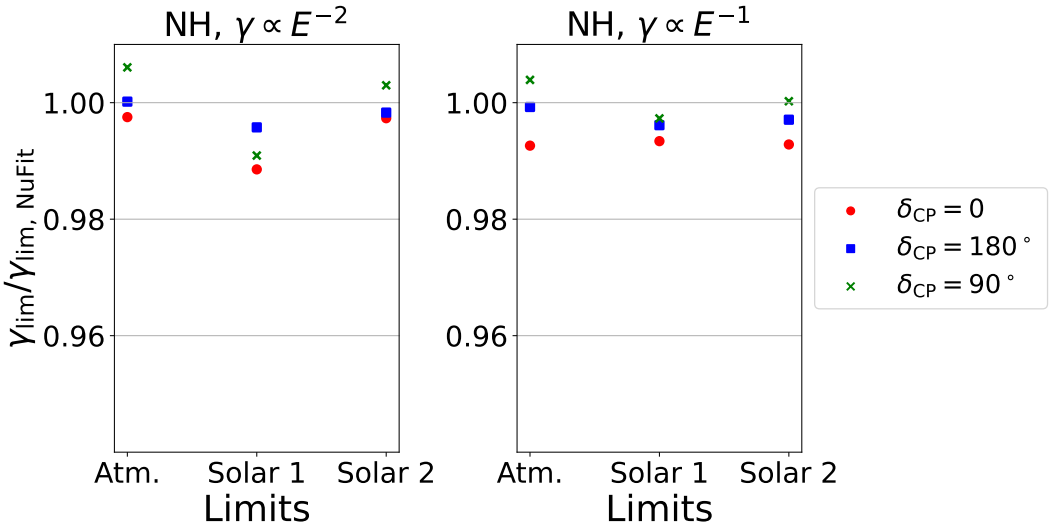

Figure 5.20: Ratio of the sensitivity with different values of δ_{CP} and the case where the NuFit value (see Table 5.4) was taken for normal hierarchy.

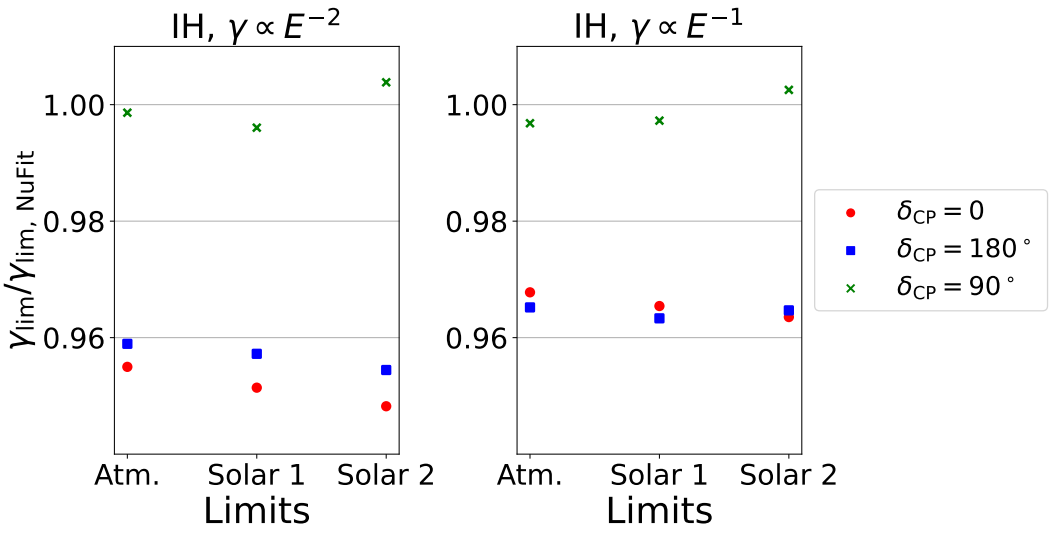

Figure 5.21: Ratio of the sensitivity with different values of δ_{CP} and the case where the NuFit value (see Table 5.4) was taken for inverted hierarchy.

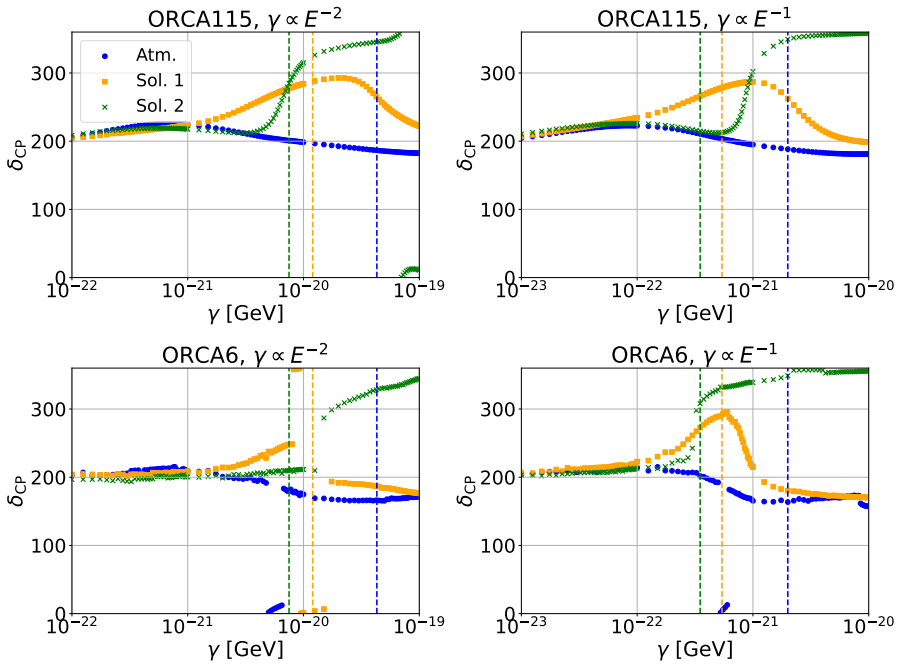

Figure 5.22: Behaviour of δ_{CP} in the minimization in dependence of the decoherence parameter for normal hierarchy.

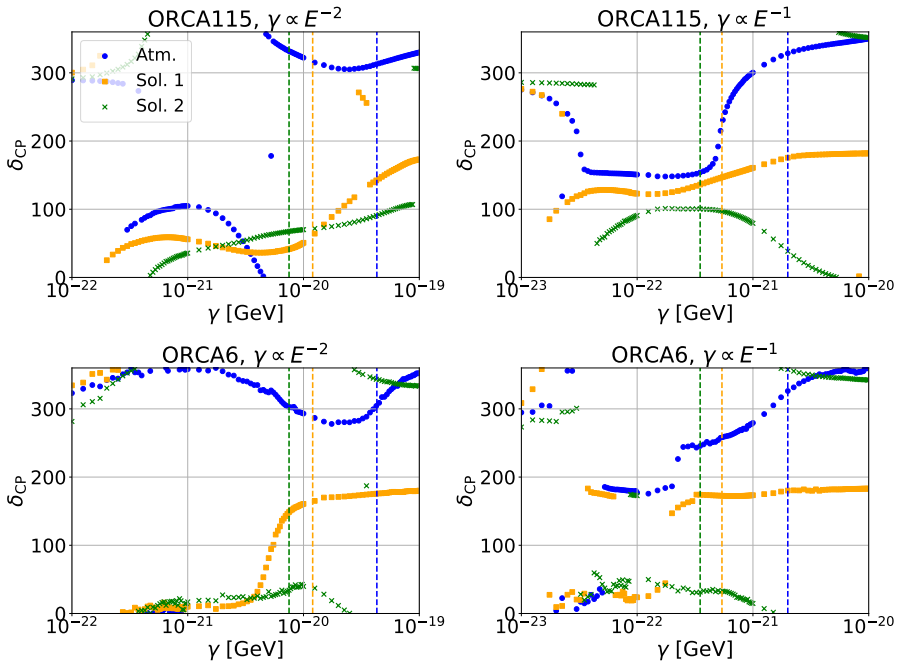

Figure 5.23: Behaviour of δ_{CP} in the minimization in dependence of the decoherence parameter for inverted hierarchy.

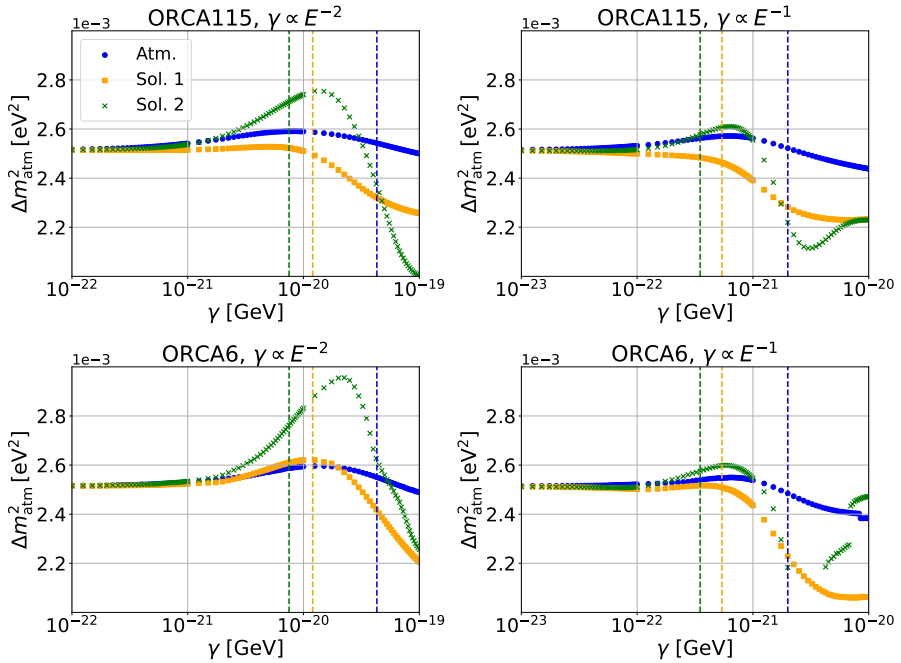

Figure 5.24: Behaviour of Δm^2_{atm} in the minimization in dependence of the decoherence parameter for normal hierarchy.

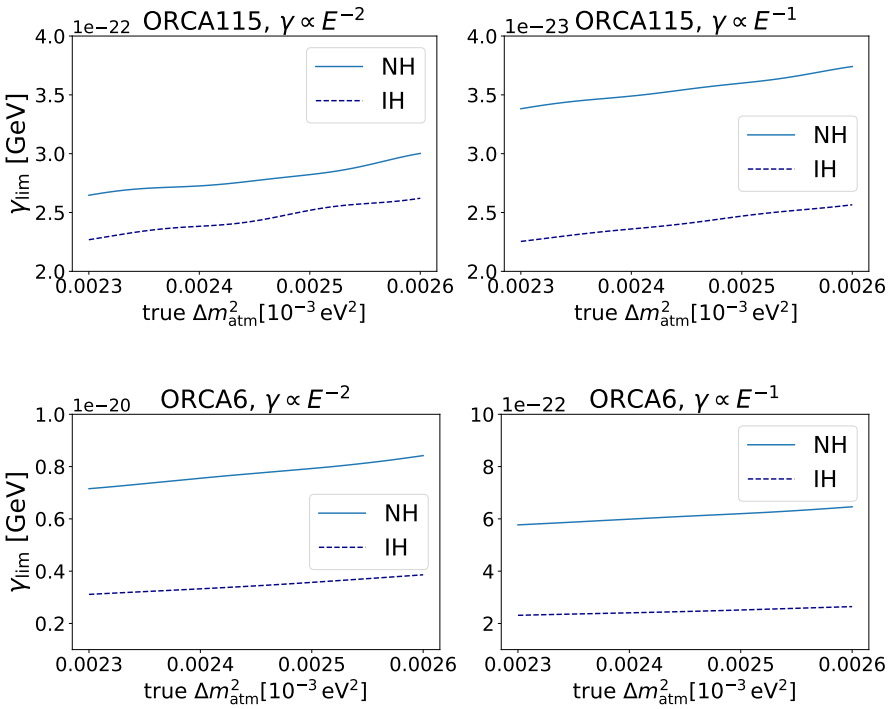

Figure 5.25: Dependence of the sensitivity on the true value of Δm^2_{atm} for the Atmospheric limit.

5.2.4 Discussion of systematics

Here, the impact of systematics stemming from uncertainties in the flux and the energy reconstruction is presented. The following systematics are taken into account in the fit:

- Energy slope: uncertainty in the spectral index α of the atmospheric neutrino flux.
- Zenith angle slope: uncertainty of the zenith angle distribution.
- $\nu_e/\bar{\nu}_e$, $\nu_\mu/\bar{\nu}_\mu$, $(\nu_\mu+\bar{\nu}_\mu)/(\nu_e+\bar{\nu}_e)$: uncertainties in the flavor composition.
- n_{showers}, n_{middles}, n_{tracks}: uncertainty in the flux normalization for each PID class.
- Energy scale: shift in the reconstructed energy.

The impact of each of these parameters on the sensitivity is shown in Figure 5.26 to Figure 5.29. The oscillation parameters were always fitted, which is why the plots show the the normalized difference to the case with just oscillation parameters fitted. Note that the energy slope and the zenith angle slope do not have any impact on the sensitivity.
The overall impact of fitting the systematics in addition to the oscillation parameters is smaller for ORCA6 than for ORCA115. However, this could be due to the fact that fitting the oscillation parameters already has a very high influence on the sensitivity for ORCA6 so that adding the systematic parameters does not lower the sensitivity too much further.

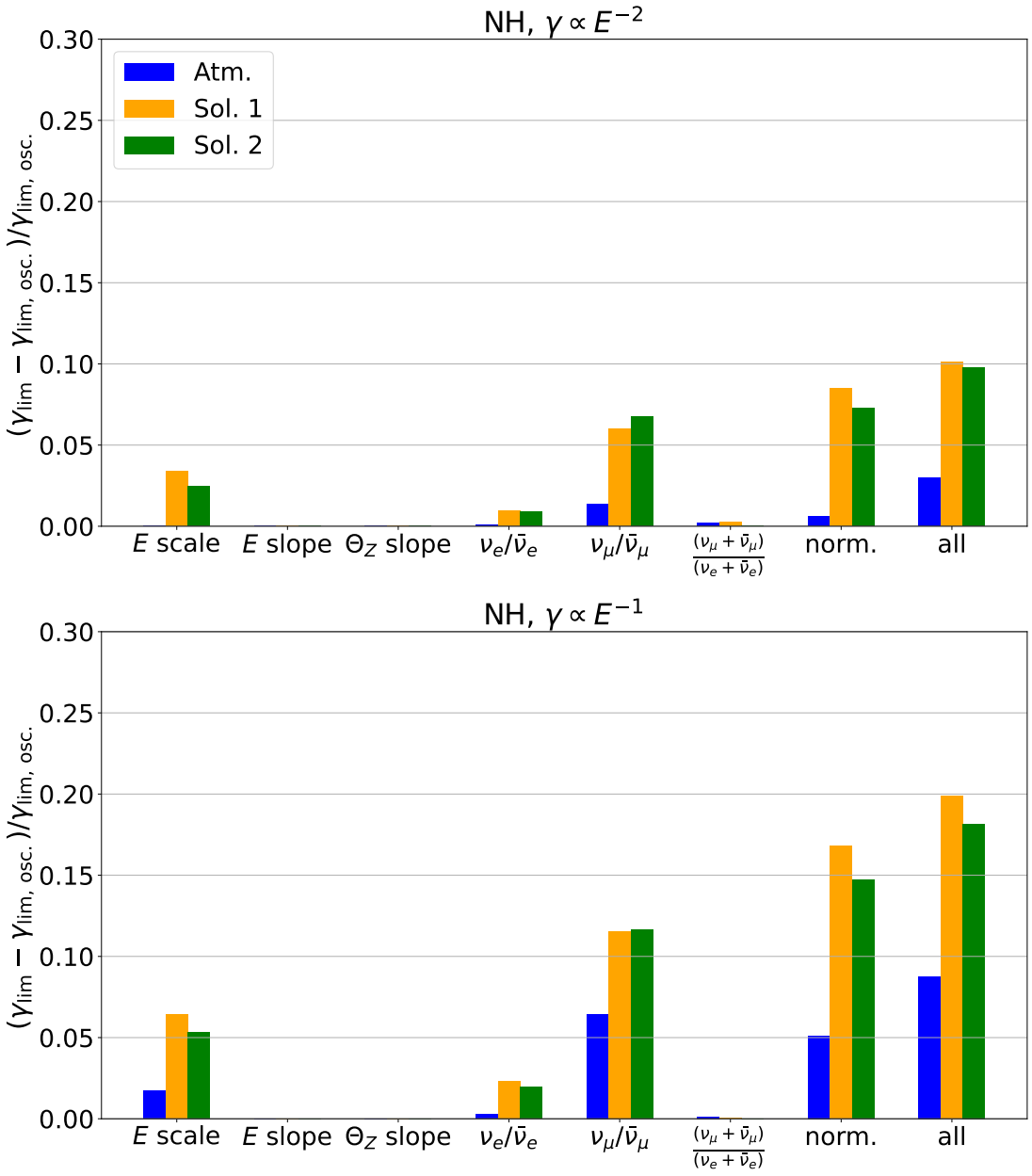

Figure 5.26: Impact of individual systematic parameters and all systematic parameters together on the sensitivity of ORCA115 for normal hierarchy. Note that the energy slope and the zenith slope angle do not have any impact.

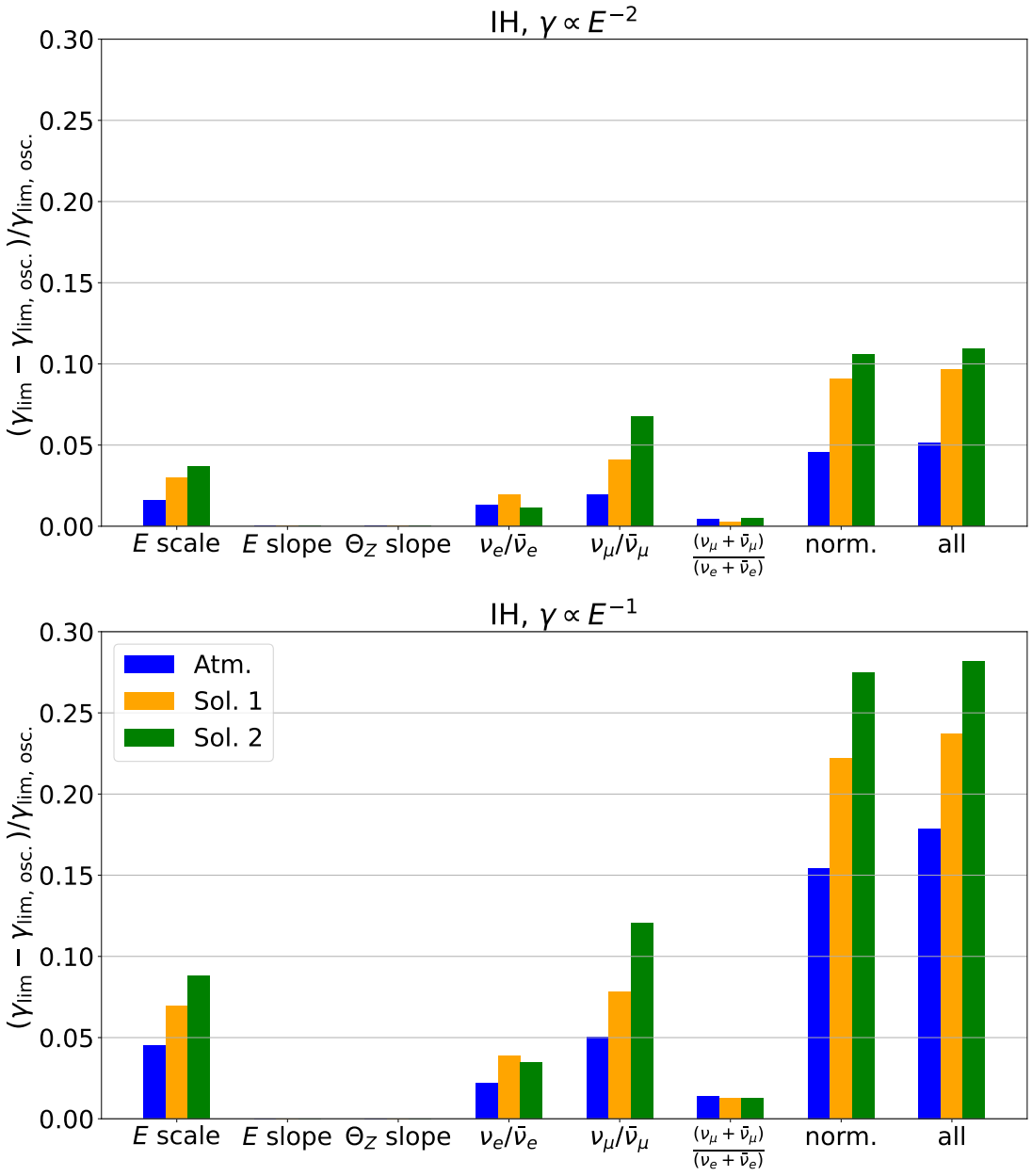

Figure 5.27: Impact of individual systematic parameters and all systematic parameters together on the sensitivity of ORCA115 for inverted hierarchy.

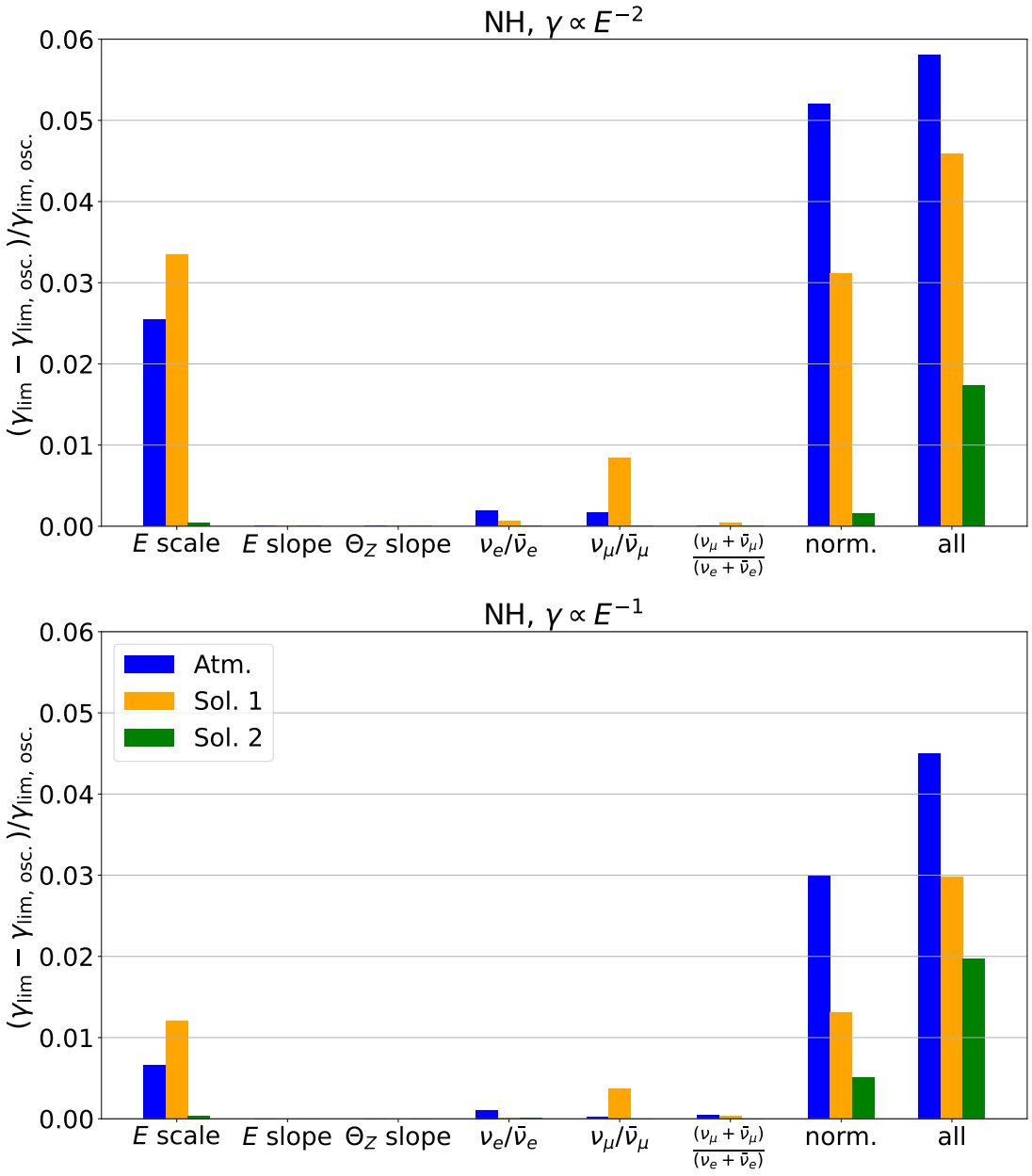

Figure 5.28: Impact of individual systematic parameters and all systematic parameters together on the sensitivity of ORCA6 for normal hierarchy. Also for ORCA6 the energy slope and the zenith slope angle do not have any impact on the sensitivity.

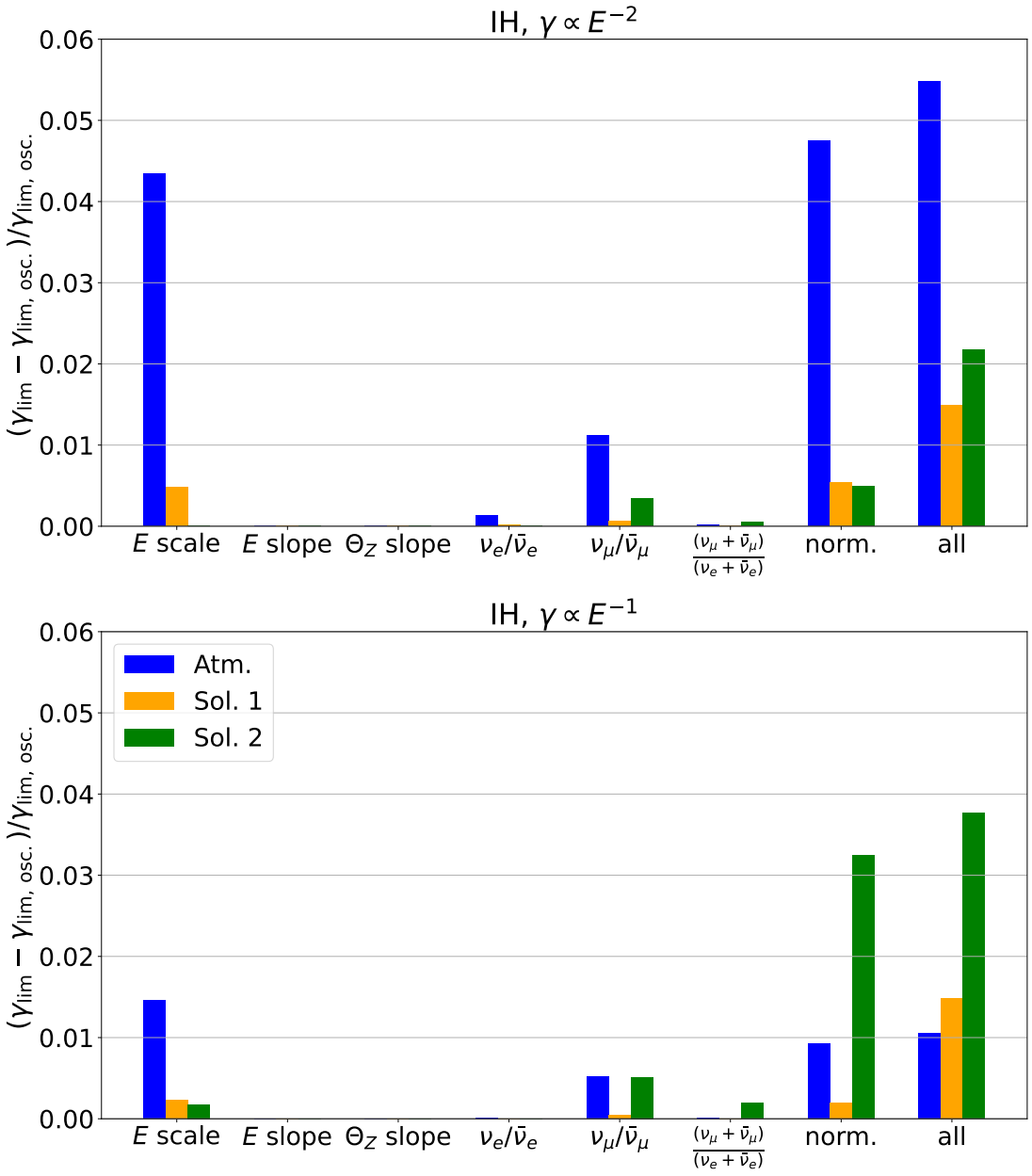

Figure 5.29: Impact of individual systematic parameters and all systematic parameters together on the sensitivity of ORCA6 for inverted hierarchy.

The energy scale shifts the reconstructed energy in the event histograms and emulates the possibility that the energy estimate from the amount of Cherenkov light is either too low or to high. The high influence of this parameter in some of the cases is not intuitive. Nevertheless, the behaviour of this parameter in dependence of γ is shown in Figure 5.30. The parameter stays within the value given by the prior.

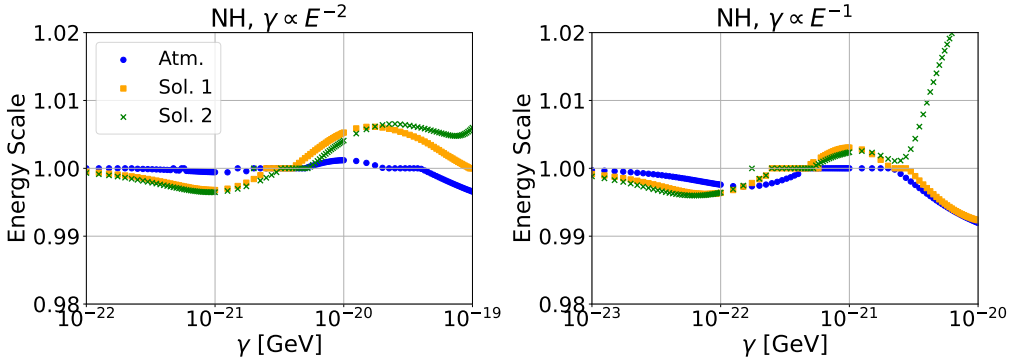

Figure 5.30: Deviation of the energy scale from the central value as a function of the decoherence parameter for ORCA115, assuming normal hierarchy. The energy scale was fitted with a prior of 0.06.

The energy slope and the zenith angle slope do not have any impact on the sensitivity to decoherence. The parameters themselves fluctuate very little around their central value.

The ratios of neutrinos to anti-neutrinos have a relatively high impact since neutrinos generate more events in the detector than anti-neutrinos. Changing the ratios therefore is another possibility to change the contrast in the oscillograms. The deviation of each of the ratios from their theoretical value is shown in Figure 5.31 to Figure 5.33, where the vertical lines once more correspond to the current bounds from DeepCore. At least up to this bound $\nu_e/\bar{\nu}_e$ and $(\nu_\mu+\bar{\nu}_\mu/(\nu_e+\bar{\nu}_e)$ stay within the value given by the prior whereas $\nu_\mu/\bar{\nu}_\mu$ is outside of this range in some of he cases.

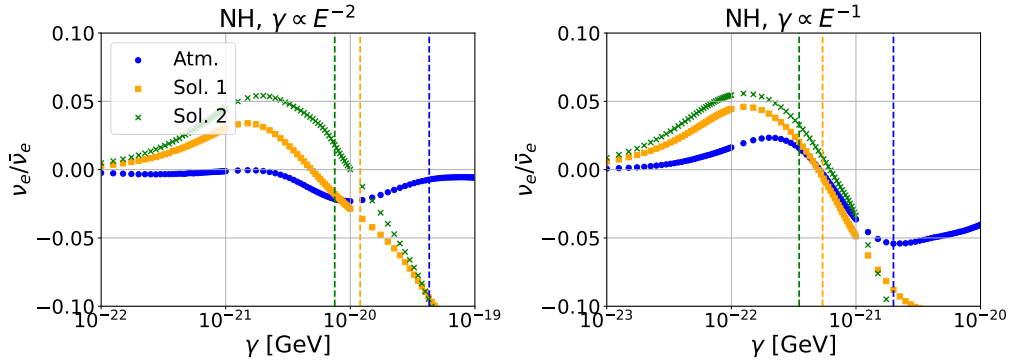

Figure 5.31: Fluctuation in the ratio of electron neutrinos and anti-neutrinos for ORCA115. The ratio was fitted with a prior of 0.07.

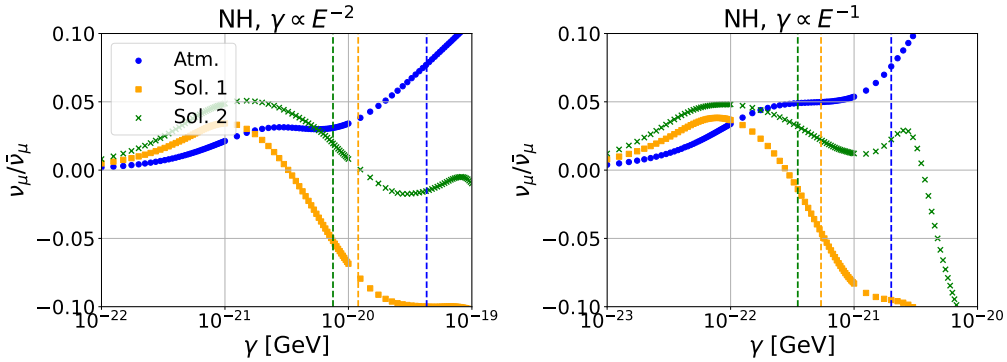

Figure 5.32: Fluctuation in the ratio of muon neutrinos and anti-neutrinos for ORCA115 fitted with a prior of 0.05.

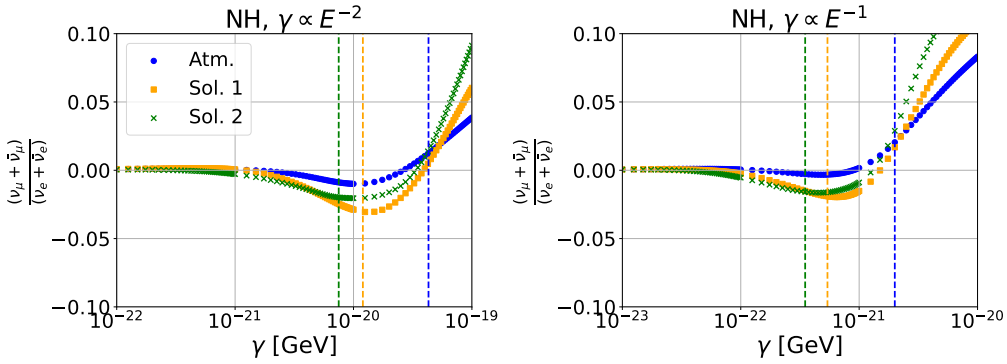

Figure 5.33: Fluctuation in the ratio of muon neutrinos and electron neutrinos for ORCA115 fitted with a prior of 0.02.

Finally, it is not surprising that the overall normalization norm. $= n_{\text{showers}} + n_{\text{middles}} + n_{\text{tracks}}$ has the largest impact on the sensitivity for most cases. This parameter can counteract the damping of decoherence effects by changing the number of events for each PID class. Figure 5.34 to Figure 5.36 show the fluctuation in the normalization for each individual PID class when fitting $n_{\text{showers}} + n_{\text{middles}} + n_{\text{tracks}}$ simultaneously. As the tracks class is the PID class that contributes most to the sensitivity, it makes sense that n_{tracks} has the biggest variation.

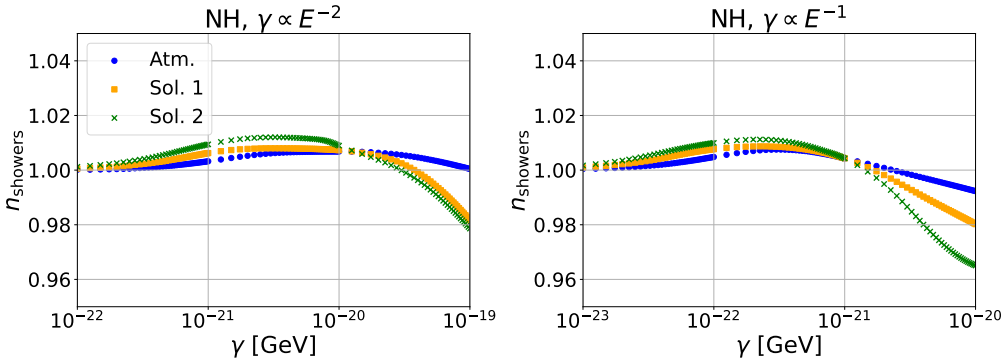

Figure 5.34: Behaviour of n_{showers} when fitting the overall normalization for ORCA115 assuming normal hierarchy.

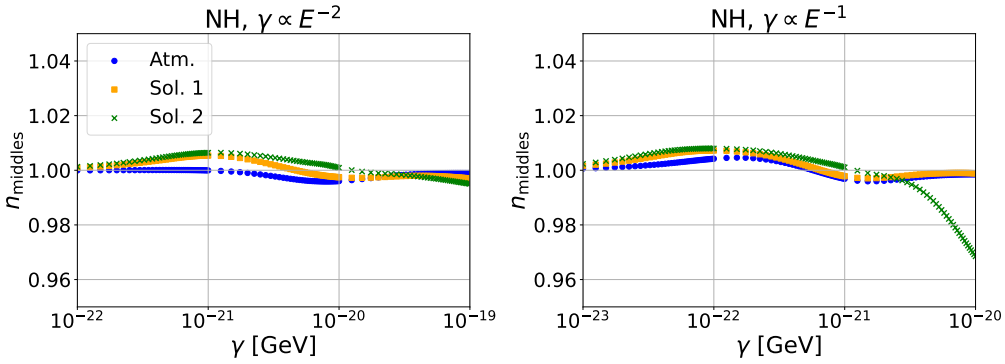

Figure 5.35: Behaviour of n_{middles} when fitting the overall normalization for ORCA115 assuming normal hierarchy.

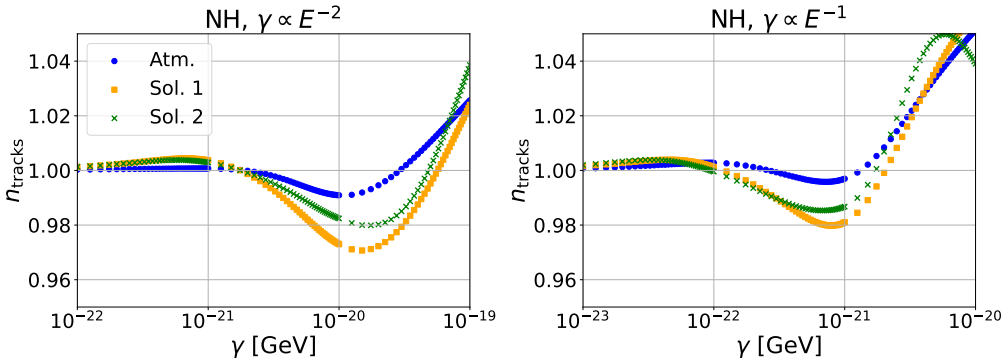

Figure 5.36: Behaviour of n_{tracks} when fitting the overall normalization for ORCA115 assuming normal hierarchy.

6 Conclusion and outlook

The analysis in this work was performed in a full three-family framework including matter effects. For KM3NeT/ORCA a fit of the oscillation parameters as well as a set of systematic parameters was performed.

It was shown that ORCA has a better sensitivity to decoherence than DeepCore for both mass hierarchies and all investigated energy dependencies of decoherence effects. The full ORCA detector can improve the bounds on the decoherence parameter by more than one order of magnitude for $\gamma \propto E^{-2}$ (all limits), and $\gamma \propto E^{-1}$ (Atmospheric limit). Furthermore, even ORCA with only six detection units can already provide new bounds for these cases. Note that the Solar Limits are better constrained by KamLAND [27] for $\gamma \propto E^{-1}$.
Some aspects that could be investigated further are the correlations between different systematic parameters as well as the problem of not finding a minimum when no prior is set on the energy slope. It could also be interesting to find out how the sensitivity improves with the data taking time for ORCA115 to see whether this is limited only by statistics.

KM3NeT/ARCA with 115 detection strings has a sensitivity comparable to IceCube. Since ARCA targets neutrinos of higher energies, it has the best sensitivity for $\gamma \propto E^{1}$ and $\gamma \propto E^{2}$. However, for ARCA no systematic parameters were included in the analysis. Due to the different energy range the systematic uncertainties from the neutrino flux are not the same as for ORCA. For example, the spectral index of the prompt neutrino flux is not very well constrained. Also the uncertainty of the ratio of muon to electron neutrinos is different at high energies. Therefore, for ARCA it is necessary to include new systematics and different priors to gain more realistic results. The oscillation parameters could not be fitted in the analysis for ARCA, since in the energy range considered there are no oscillations. However, in [15] it was stated that the oscillation parameters were fitted in the analysis for IceCube. It is not really clear how this was done. This is is a point that requires further investigation for a better comparison of the performance of ARCA and IceCube.

All in all, especially the sensitivities to decoherence for KM3NeT/ORCA are very promising. Since for ORCA6 data is already available, new bounds on decoherence effects can be set in the near future. Also, as the ORCA detector will be taking data during construction, the bounds will improve with the detector size over the years. This allows to constrain the decoherence parameter further even before the construction has finished.

A Additional Figures

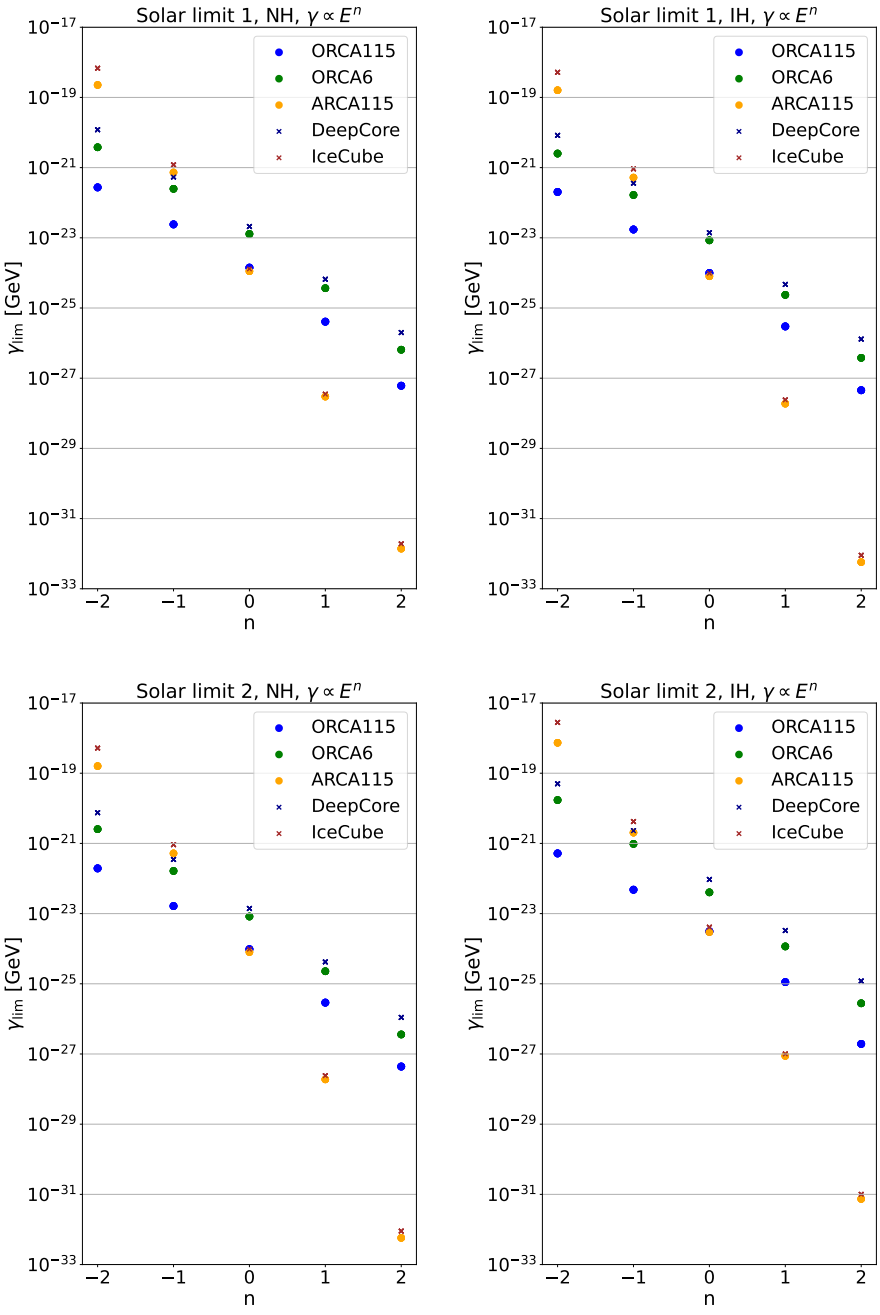

Figure A.1: Bounds on the decoherence parameter at the 95 % CL for ORCA115, ORCA6 and ARCA115 in dependence of the power-law index n in comparison with current bound from IceCube and DeepCore.

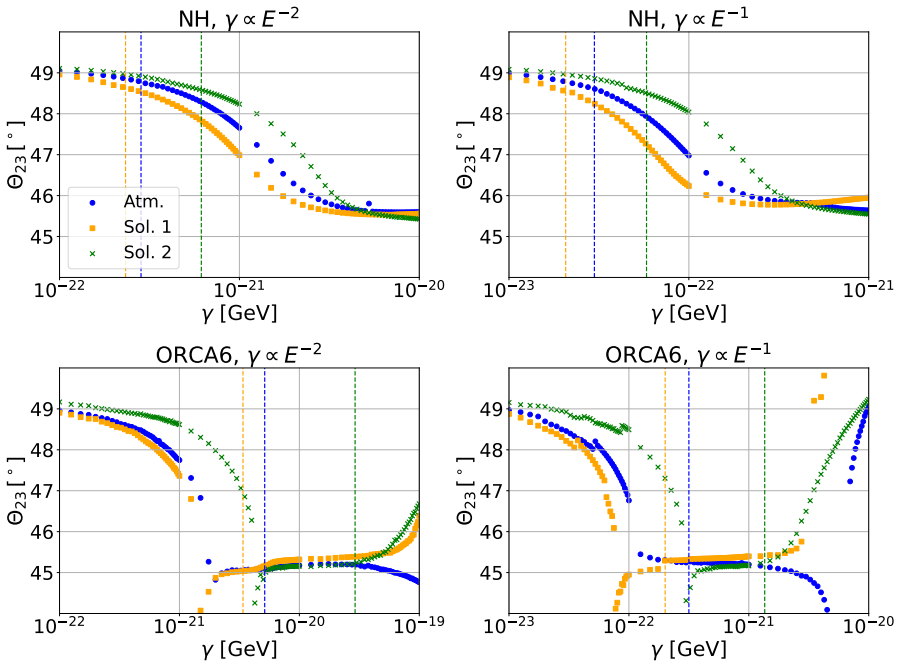

Figure A.2: Behaviour of Θ_{23} in the minimization in dependence of the decoherence parameter for inverted hierarchy.

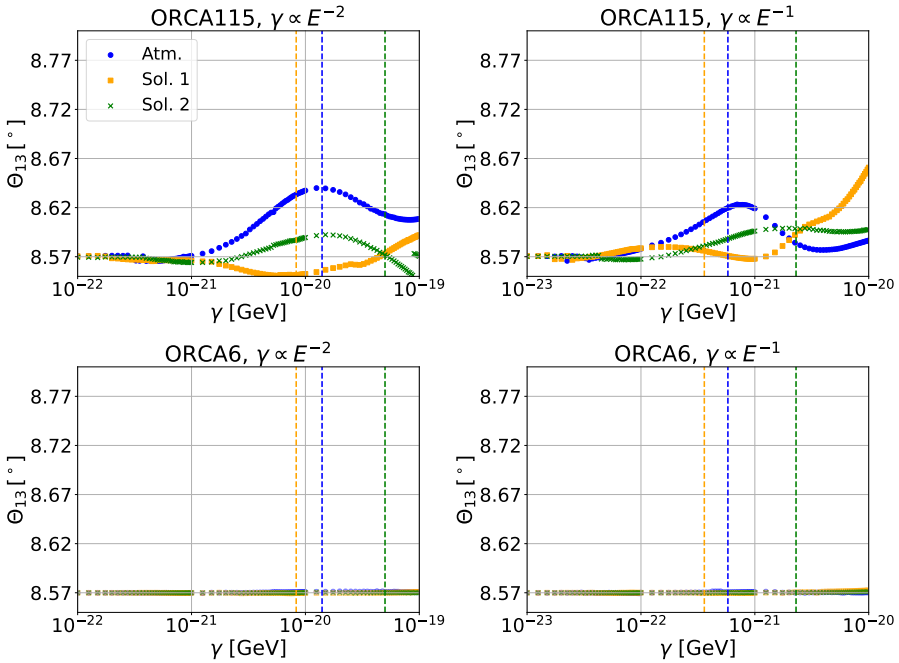

Figure A.3: Behaviour of Θ_{13} in the minimization in dependence of the decoherence parameter for inverted hierarchy.

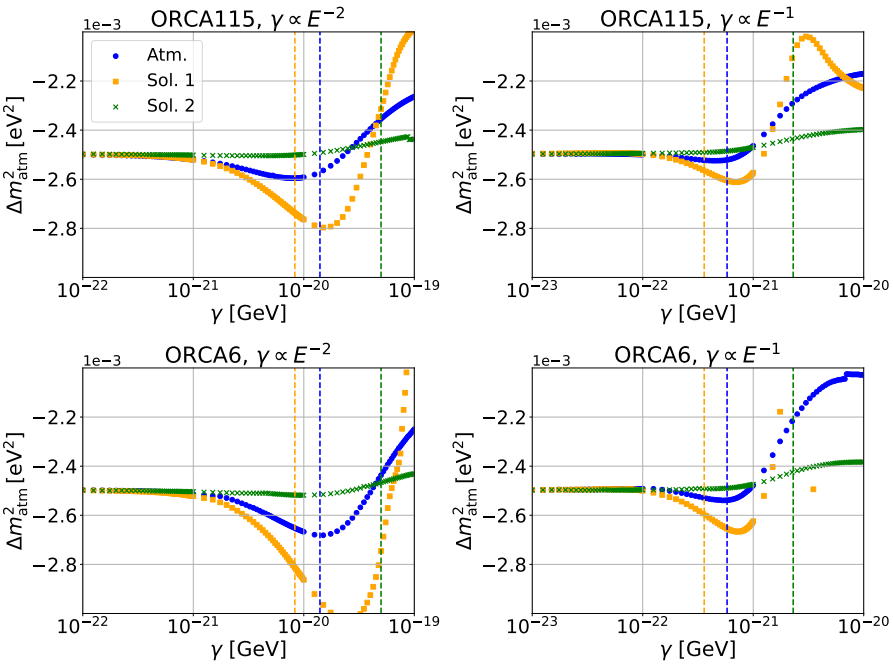

Figure A.4: Behaviour of $\Delta m^2_{\mathrm{atm}}$ in the minimization in dependence of the decoherence parameter for inverted hierarchy.

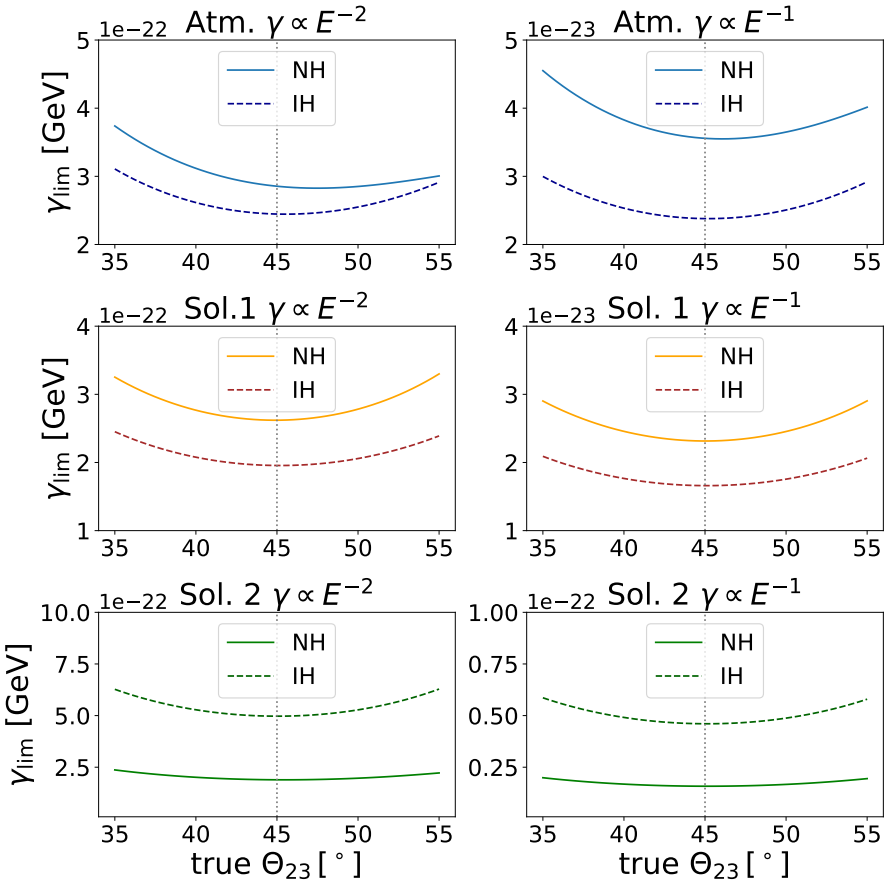

Figure A.5: Dependence of the sensitivity of ORCA115 on the true value of Θ_{23} for all limits.

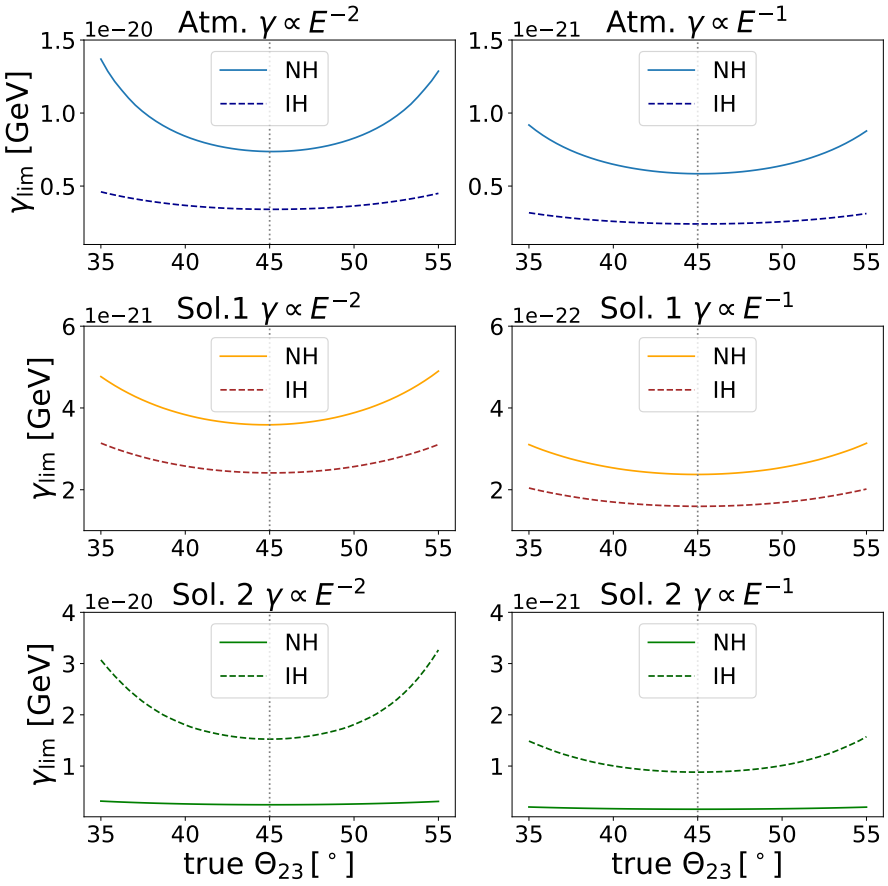

Figure A.6: Dependence of the sensitivity of ORCA6 on the true value of Θ_{23} for all limits.

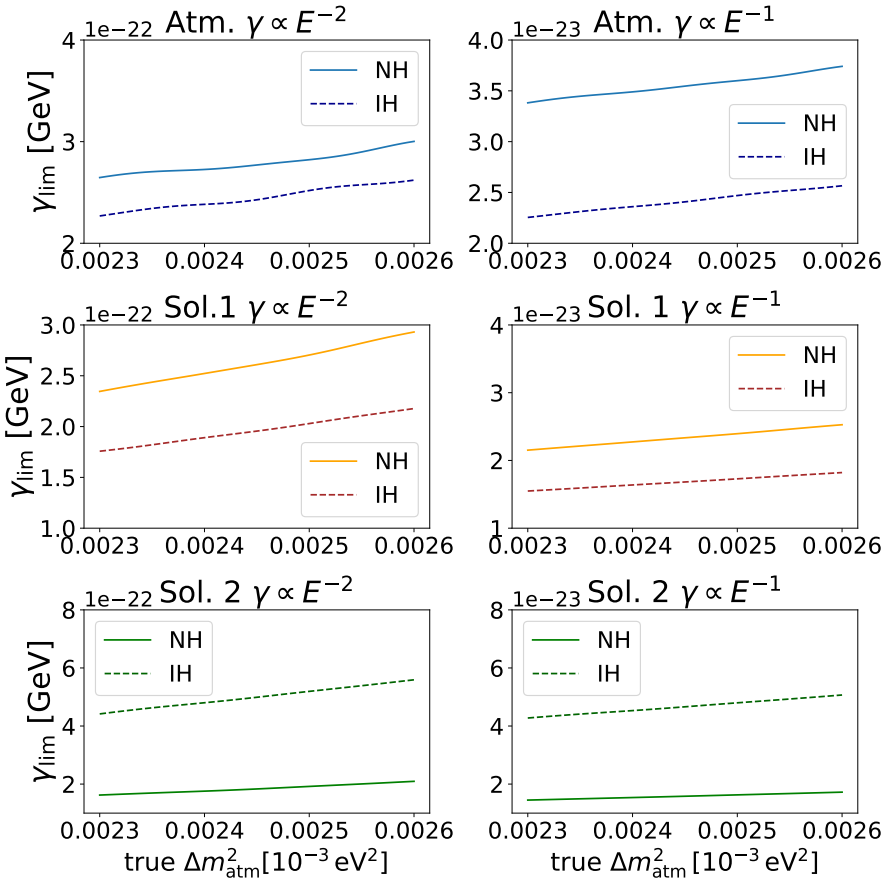

Figure A.7: Dependence of the sensitivity of ORCA115 on the true value of $\Delta m^2_{\mathrm{atm}}$ for all limits.

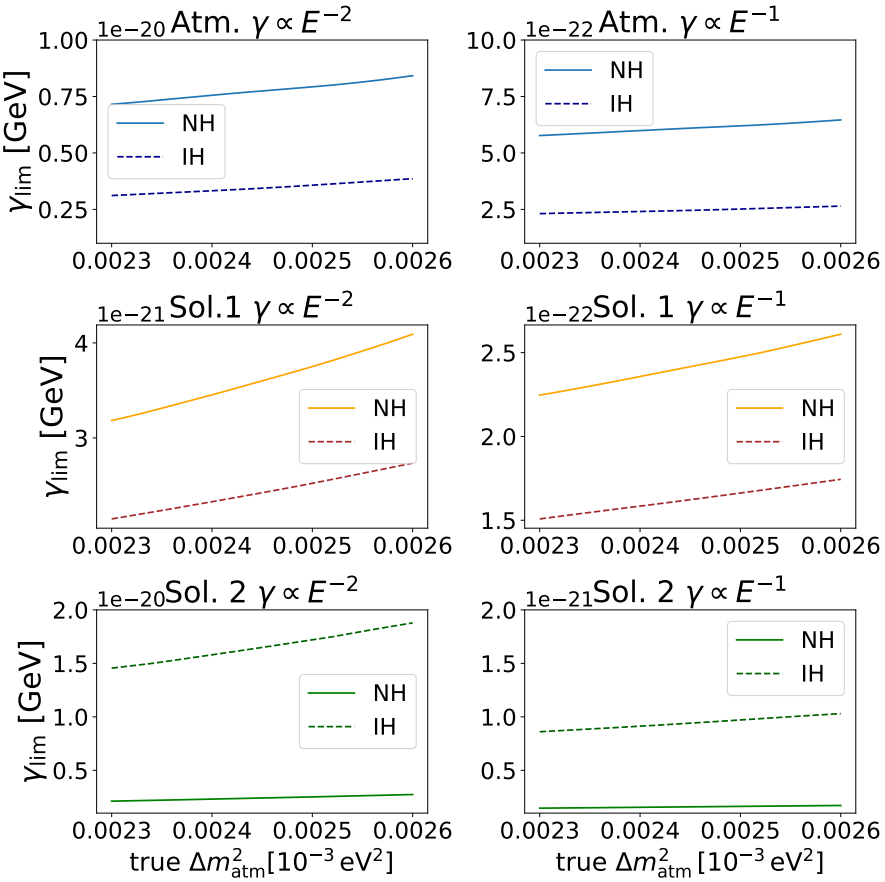

Figure A.8: Dependence of the sensitivity of ORCA6 on the true value of Δm^2_{atm} for all limits.

B Decoherence in SWIM

The programs used in this work can be found in the branch `https://git.km3net.de/sbourret/Swim/-/tree/dev-decoherence`.

B.1 Calculated oscillation probabilities

The oscillation probabilities can be calculated and plotted with the programs available at `https://git.km3net.de/sbourret/Swim/-/tree/dev-decoherence/Applications/Decoherence/DecoProbabilities`. The three different programs have the following functionalities:

- `DecoProb.C`: calculate oscillation probabilities in dependence of the neutrino energy for a fixed zenith angle.
- `DecoProb2D.C`: calculate oscillation probabilities in dependence of the neutrino energy and the zenith angle (only up-going events).
- `DecoTracks2D.C`: calculate an estimate of the distribution of track-like events in dependence of the neutrino energy and the zenith angle (only up-going events).

There are three parameters that can be varied in all of the programs: the power-law index ($n = \pm 2, \pm 1, 0$), the strength of decoherence effects γ_{ij}^0, and the mass hierarchy.
In `DecoProb.C`, `DecoTracks2D.C` also the initial and final neutrino flavor can be specified. Furthermore, it can be distinguished between neutrinos and anti-neutrinos. `DecoProb.C` additionally takes the zenith angle as input.
Each of these programs returns a table that contains calculated oscillation probabilities, which can be plotted using the notebook `PlotOscillationProbabilities.ipynb`.

B.2 Sensitivity studies

There are two programs to calculate the $\Delta\chi^2$ to obtain the sensitivity to decoherence in SWIM:

- `SimpleDeco.cc`: calculate χ^2_{stat} without fitting any parameters for a simple estimate of the sensitivity.
- `DecoFit.cc`: calculate χ^2_{tot} fitting any number of oscillation parameters and systematics that are implemented in SWIM.

Some of the parameters that can be passed when running the programs are the MC sample, the mass hierarchy, the limit/model (Atmospheric limit, Solar limit 1 or Solar limit 2), the power-law index ($n = \pm 2, \pm 1, 0$), and whether ARCA or ORCA are considered.
The parameters that should be fitted as well as their priors need to be set directly in `DecoFit.cc`.

The determination of the 95 %CL as well as the visualization of the results was done with:

- `SimpleDecoBestCuts.ipynb`: using the output of `SimpleDeco.cc`.
- `FitOscillationParams.ipynb`: using the output of `DecoFit.cc` with oscillation only parameters fitted.
- `FitOscillationParams.ipynb`: using the output of `DecoFit.cc` with all oscillation parameters and additional systematics fitted.

Further dependencies were investigated with:

- `PID_comparison.ipynb`: use the output of `SimpleDeco.cc` with different PID classes and compare the detector sensitivities for the different cases. The PID classes need to be set directly in `SimpleDeco.cc` before creating the response matrix.
- `DecoTheta23.ipynb`: use the output of `ContourTheta23.cc` to calculate the sensitivity as a function of the true value of Θ_{23}. Note that `ContourTheta23.cc` is equal to `SimpleDeco.cc` except for an additional loop on Θ_{23}.
- `DecoDeltaM.ipynb`: use the output of `ContourDeltaM.cc` to calculate the sensitivity as a function of the true value of Δm^2_{atm}. Again, this program is equal `SimpleDeco.cc` except for an additional loop on Δm^2_{atm}.
- `CP_phase.ipynb`: use the output of `SimpleDeco.cc` with different with different values of δ_{CP}.

Bibliography

[1] IceCube Collaboration. The IceCube Neutrino Observatory Part V: Neutrino Oscillations and Supernova Searches, 2013. https://arxiv.org/abs/1309.7008.

[2] Y. et al. Fukuda. Evidence for oscillation of atmospheric neutrinos. *Phys. Rev. Lett.*, 81:1562–1567, Aug 1998.

[3] Q. R. et al. Ahmad. Direct evidence for neutrino flavor transformation from neutral-current interactions in the Sudbury Neutrino Observatory. *Phys. Rev. Lett.*, 89:011301, Jun 2002.

[4] Fabio Benatti and Roberto Floreanini. Open quantum dynamics: Complete positivity and entanglement. *International Journal of Modern Physics B*, 19(19):3063â3139, Jul 2005.

[5] S Adrián-Martínez, M Ageron, F Aharonian, S Aiello, A Albert, F Ameli, E Anassontzis, M Andre, G Androulakis, M Anghinolfi, and et al. Letter of intent for KM3NeT 2.0. *Journal of Physics G: Nuclear and Particle Physics*, 43(8):084001, Jun 2016.

[6] S. Abe, T. Ebihara, S. Enomoto, K. Furuno, Y. Gando, K. Ichimura, H. Ikeda, K. Inoue, Y. Kibe, Y. Kishimoto, and et al. Precision measurement of neutrino oscillation parameters with KamLAND. *Physical Review Letters*, 100(22), Jun 2008.

[7] Mark Thomson. *Modern Particle Physics*. Cambridge University Press, 2013.

[8] F.P. An, A.B. Balantekin, H.R. Band, M. Bishai, S. Blyth, I. Butorov, G.F. Cao, J. Cao, W.R. Cen, Y.L. Chan, and et al. New measurement of antineutrino oscillation with the full detector configuration at Daya Bay. *Physical Review Letters*, 115(11), Sep 2015.

[9] Ivan Esteban, M.C. Gonzalez-Garcia, Michele Maltoni, Thomas Schwetz, and Albert Zhou. The fate of hints: updated global analysis of three-flavor neutrino oscillations. *Journal of High Energy Physics*, 2020(9), Sep 2020.

[10] C. Giunti and C. W. Kim. Coherence of neutrino oscillations in the wave packet approach. *Physical Review D*, 58(1), Jun 1998.

[11] F. P. An et al. Study of the wave packet treatment of neutrino oscillation at Daya Bay, 2016. https://arxiv.org/abs/hep-ph/0208166.

[12] Bin Xu. Neutrino Decoherence in Simple Open Quantum Systems, 2021.

[13] Fabio Benatti and Roberto Floreanini. Open system approach to neutrino oscillations. *Journal of High Energy Physics*, 2000(02):032â032, Feb 2000.

[14] A.M. Gago, E.M. Santos, W.J.C. Teves, and R. Zukanovich Funchal. A study on quantum decoherence phenomena with three generations of neutrinos. Aug 2002.

[15] P. Coloma, J. Lopez-Pavon, I. Martinez-Soler, and H. Nunokawa. Decoherence in neutrino propagation through matter, and bounds from IceCube/DeepCore. *The European Physical Journal C*, 78(8), Aug 2018.

[16] João A. B. Coelho. *Investigacao de Mecanismos Alternativos a Oscilacao de Neutrinos no Experimentos MINOS.* PhD thesis, Campinas State U., 2012. `https://lss.fnal.gov/archive/thesis/2000/fermilab-thesis-2012-23.pdf`.

[17] Simon Bourret. *Neutrino oscillations and earth tomography with KM3NeT-ORCA*. PhD thesis, Université Sorbonne Paris Cité, 2018.

[18] J. P. Yáñez and A. Kouchner. Measurement of atmospheric neutrino oscillations with very large volume neutrino telescopes. *Advances in High Energy Physics*, 2015:1â24, 2015.

[19] U.F. Katz and Ch. Spiering. High-energy neutrino astrophysics: Status and perspectives. *Progress in Particle and Nuclear Physics*, 67(3):651â704, Jul 2012.

[20] T. Eberl. Neutrino physics lecture, Friedrich-Alexander-Universität Erlangen- Nürnberg, 2020.

[21] ROOT data analysis framework. `https://root.cern/`.

[22] M. Honda, M. Sajjad Athar, T. Kajita, K. Kasahara, and S. Midorikawa. Atmospheric neutrino flux calculation using the nrlmsise-00 atmospheric model. *Physical Review D*, 92(2), Jul 2015.

[23] João A. B. Coelho. Neutrino oscillation calculator OscProb. `https://github.com/joaoabcoelho/OscProb`.

[24] Adam M. Dziewonski and Don L. Anderson. Preliminary Reference Earth Model. *Physics of the Earth and Planetary Interiors*, 25(4):297–356, 1981.

[25] Matthias Winkler Fred James. Minuit 2.

[26] Matthias Winkler Fred James. Mnmigrad.

[27] G. Balieiro Gomes, M. M. Guzzo, P. C. de Holanda, and R. L. N. Oliveira. Parameter limits for neutrino oscillation with decoherence in KamLAND. *Phys. Rev. D*, 95:113005, Jun 2017.

Declaration

I declare that I completed this work on my own and that information which has been directly or indirectly taken from other sources has been noted as such.

Erlangen, 03.03.2022

Student